ESTABLISHING THE METHOD OF DUAL-TENSOR FOR TRACT BASED ANALYSIS (DTTA) AND INVESTIGATING HUMAN BRAIN DEVELOPMENTAL CONNECTOME WITH DIFFUSION MRI

by

VIRENDRA RADHESHYAM MISHRA

Presented to the Faculty of the Graduate School of

The University of Texas at Arlington in Partial Fulfillment

of the Requirements

for the Degree of

DOCTOR OF PHILOSOPHY

THE UNIVERSITY OF TEXAS AT ARLINGTON

May 2014

Acknowledgements

I would like to thank Dr. Hao Huang for opening the door for me in his laboratory and being my mentor. His continuous support and belief in my abilities has culminated in completion of this thesis successfully. I cannot thank him enough for all the words of suggestion, guidance and patience that he has persisted with me throughout these four years of my stay under him as my mentor.

I would also like to thank Dr. Hanzhang Lu, Dr. Hanli Liu (committee chair), Dr. Georgios Alexandrakis and Dr. Juan Pascual for taking time out of their busy schedule and serving on my thesis committee. The inputs extended to me from all the committee members have been very helpful in completing my research. I would also like to thank my lab members; Tina Jeon, Tien Nyugen, Tejasvi Gundapuneedi, Minhui Ouyang, Austin Ouyang and Qiaowen Yu for sharing with me their respective expertise whenever needed. I would also to thank my friends Mukesh Jain, Mihir Mehta, Rohit Rawat, Amit Jain, Shachi Agarwal, Deepali Shewale, Sameer Dhamne, Srikanth Vasudevan, Swarupnarayan Dash, Sandeep Ganji, Binu Thomas, Sina Aslan, Abhishek Banerjee, Sairam Geethanath and Praveen Gulaka who have made my transition to UTA and graduate school an easy and enriching one.

And finally, I thank my parents Shri. Radheshyam and Smt. Indravati Mishra, my wife Anchal Mishra, my brothers, Mr. Dhirendra and Satyendra Mishra, my sisters, Sarita Shukla and Sunita Mishra and my son, Rudravardaan for extending their love, blessings, support and encouragement without which I cannot become what I am today.

Janaury 31, 2014

Abstract

ESTABLISHING THE METHOD OF DUAL-TENSOR FOR TRACT BASED ANALYSIS (DTTA) AND INVESTIGATING HUMAN BRAIN DEVELOPMENTAL CONNECTOME WITH DIFFUSION MRI

Virendra Mishra, PhD

The University of Texas at Arlington, 2014

Supervising Professor: Hao Huang

Diffusion MRI (dMRI) has the unique ability of studying white matter fiber structure in the human brain in-vivo. The trajectory of the white matter fibers inside the brain can be mapped using the tractography techniques and their structural integrity can be assessed with the help of various metrics such as fractional anisotropy (FA) derived from diffusion tensor imaging (DTI). But with typical dMRI in clinical applications, almost half of human brain white matter (WM) voxels has crossing-fiber regions (CFR) where WM microstructural integrity is significantly underestimated with single tensor FA. A technique adapted to WM tract analysis and correcting the anisotropy bias at the CFR for dMRI acquired within 5 minutes in clinical research needs to be developed and was the goal of Aim 1. Other than FA, various other DTI derived metrics such as radial (RD), axial (AxD) and mean diffusivity (MD) have been used to noninvasively assess the microstructural development of human brain WM. At birth, most of the major WM tracts are apparent but in a relatively disorganized pattern. Brain maturation is a process of establishing organized pattern of these major WM tracts. However, the change in the spatial-temporal linkage pattern of major WM tracts during development remains unclear and evaluating the linkage pattern of major WM tracts during development was the goal of Aim 2. Moreover, the linkage pattern observed at birth is a result of complicated

molecular and biochemical processes which take place during perinatal brain development and reshape the later brain structural network for sophisticated functional and cognitive requirements. However, structural topological configuration of human brain during this specific development period is not well understood and was the goal of Aim 3.

To evaluate Aim 1, novel dual tensor tract analysis (DTTA) was developed that includes dual tensor fitting with Gaussian mixture model and tract analysis. Digital phantom was designed and dMRI with multiple b values was acquired to evaluate the accuracy of estimated tract-specific anisotropy at CFR after DTTA correction. The results from phantom study showed high accuracy of the corrected anisotropy with DTTA. The results from normal human dMRI used in clinical research indicated effective identification of CFR and correction of tract-specific anisotropy. Corrected anisotropy with DTTA is highly consistent to the single fiber FA within the same tract. The results suggest great potential of DTTA in estimating accurate tract-specific anisotropy at CFR and conducting tract analysis in clinical research.

To evaluate Aim 2, diffusion magnetic resonance image (dMRI) data of 26 neonates and 28 children around puberty was acquired. 10 major WM tracts, representing four major tract groups involved in distinctive brain functions, were traced with DTI tractography for all 54 subjects. With the 10 by 10 correlation matrices constructed with Spearman's pairwise inter-tract correlations and based on tract-level measurements of FA, RD, AxD and MD of both age groups, we assessed if the inter-tract correlations become stronger from birth to puberty. In addition, hierarchical clustering was performed based on the pairwise correlations of WM tracts to reveal the clustering pattern for each age group and evaluate the pattern shift from birth to puberty. Stronger and enhanced microstructural inter-tract correlations were found during development from birth to puberty. The linkage patterns of two age groups differ due to brain

development. These changes of microstructural correlations from birth to puberty suggest inhomogeneous but organized myelination processes which cause the reshuffled inter-tract correlation pattern and make homologous tracts tightly clustered. It opens a new window to study WM tract development and can be potentially used to investigate atypical brain development due to neurological or psychiatric disorders.

To evaluate Aim 3, dMRI of 15 in-vivo human brains in the age range of 31 gestational weeks (wg) to 41wg were acquired to characterize structural brain network during perinatal brain development. dMRI tractography was used to construct structural brain networks and the underlying topological properties were quantified by graph-theory approaches. Small-world attributes were found to be evident throughout the perinatal brain development. Our results reveal a perinatal brain “connectome” that shows monotonically increasing network derived metrics and stronger networks with development, which is likely to be the outcome of both strengthening of major white-matter tracts and pruning of small fibers.

Table of Contents

List of Illustrations

List of Tables

Chapter 1

Introduction

1.1. Normal White Matter of the Brain

The human brain is a highly complex structure consisting of gray and white matter tissue weighing about 1400 grams in the adult (Blinkov and Glezer, 1968; Filley, 2011). Gray matter, also known as the cerebral cortex, is roughly 3-mm thick external surface of the brain consisting of billions of neuronal cell bodies and several subcortical structures (Blinkov and Glezer, 1968). It is speculated that out of the 100 billion neurons in the brain, vast majority of the neurons are classified as interneurons and serve to link gray matter regions with each other (Filley, 2011; Nolte, 1999). Cerebral cortex has been considered of significant importance because of its relationship to memory (Filley, 2011; Filley et al., 1988), intelligence (Garde et al., 2005; van Dijk et al., 2008), executive functions (Reed et al., 2004; Swanberg et al., 2004; Tullberg et al., 2004; Wen et al., 2004), language (Filley, 2011) and self (Cummings, 2004; Rafii and Aisen, 2009).

White matter tissue occupies roughly 50% of the entire brain parenchyma and is composed mainly of lipids and hence freshly cut white matter tissue appears to be white. It consists of densely packed fiber collections classified into projection, commissural, limbic and association fiber tracts (Catani, 2011; Filley, 2011; Nolte, 1999). Commissural, association and limbic fibers are predominantly associated with conveying information from one region of the brain to other while projection fibers conveys afferent sensory input to the brain or efferent motor output to the limbs (Catani, 2011; Filley, 2011). Most of the white matter fiber tracts remain confined as inter or intra-hemispheric connecting tracts.

The microstructure of the white matter contains myelinated axons, glial cells and nourishing blood vessels (Filley, 2011; Nolte, 1999). The fiber tracts are composed of

these myelinated axons of neurons that serve as the connecting highway of the brain that either conveys the information from one region of the brain to other or conveys the information to a part of the body to perform an ordered function (Fields, 2008; Filley, 2011; Filley and Kleinschmidt-DeMasters, 2001). Myelin is produced from oligodendrocytes and encircles axons with a concentric insulin sheath made up of 70% lipid and 30% proteins (Baumann and Pham-Dinh, 2001; Evans and Finean, 1965). Myelinated axons can conduct action potential 100 times faster than those without myelin due to saltatory conduction between myelinated axonal segments (Filley, 2011; Filley and Kleinschmidt-DeMasters, 2001; Huxley and Stampfli, 1949).

1.2. Importance of Studying Brain White Matter

Since 50% of the whole brain volume is occupied by white matter and they are responsible for transferring the information from one brain region to another or/and transferring the information from the brain regions to periphery to perform a certain function; studying the brain white matter needs no justification from a neuroscientific perspective. White matter is peculiarly important as its neuroanatomy is highly variable across the lifespan of an individual (Fields, 2008; Filley, 2001; Marner et al., 2003; Wozniak and Lim, 2006). Similar to gray matter, white matter also has developmental process right from the birth till the end of life (Huppi, 2011). Neuronal formation to convey information across the brain gray matter regions occurs early but myelination, a key aspect of how fast the signal gets transmitted, is developed later and continues well into postnatal life (Benes et al., 1994). White matter volume continues to increase until mid-age and undergoes a slow process of volume reduction in old age (Salat et al., 1999; Tang et al., 1997). Hence it can be observed that these developmental changes in white matter directly affect the human behavior and may even influence certain emotional and

cognitive functions of an individual at various stages of life (Huang et al., 2011; Huang et al., 2012b).

It also becomes important to study brain white matter because of its implications in certain brain disorders such as traumatic brain injury (Alexander, 1995; Filley, 2001), neoplasms (eg: focal white matter tumors, diffusely infiltrative gliomas etc.), vascular diseases (eg: Leukoaraiosis, Migraine), metabolic disorders (eg: hypoxia, high altitude cerebral edema), demyelinative diseases (eg: Multiple Sclerosis, Schilder's disease) and a multitude of other disorders that are still under active research (Filley, 2001; Filley, 2011).

1.3. Role of Magnetic Resonance Imaging (MRI) in Studying White Matter

Given the significance of studying brain white matter in normal brain function, various techniques have been used to analyze the structure of the white matter. A few of the notable techniques include confocal laser scanning microscopy, myelin staining, tract tracing and polarized light imaging (Axer, 2011). Although all of these techniques have significant advantages in terms of resolution and studying interested area of white matter in a lot of details, it is very time consuming and needs a highly skilled and trained laboratory members to complete the task (Axer, 2011).

Magnetic Resonance Imaging (MRI) developed in past few decades has been robust, fast, reproducible and can be tailored according to the objective of the study. The most important advantage of using MRI to study white matter is its application to living human beings. MRI has been used to study white matter development and its role in brain functions throughout the lifespan of an individual (Dosenbach et al., 2010; Filley, 2001; Huppi, 2011; Lebel et al., 2008; Li et al., 2012). It has also been used to study the efficacy of a drug treatment to a diseased neuropathological case (Bakshi et al., 2005).

T_1 weighted and T_2 weighted MRI has been used extensively to study white matter brain pathologies (Filley, 2001; Tofts, 2003) and to study human brain development (Huppi, 2011; Wozniak and Lim, 2006). MRI offers excellent soft tissue contrast along with no radiation damage to the living being unlike CT or X-rays. It is because of this excellent ability of MRI to image a human being without irradiating, *in-vivo* extends its importance to image a baby *in-utero* (Studholme, 2011).

1.4. Basics of Diffusion MRI (dMRI)

Diffusion MRI (dMRI) exploits the inherent diffusion of water inside the brain as a contrast to generate the MR signal. Diffusion is a process which is governed by thermally driven random *Brownian motion* of any molecule (Callaghan, 2011). It is by virtue of this process that certain matter inside the brain is transferred from one region to another. Every molecule by itself has an intrinsic and characteristic diffusion coefficient, also known as a diffusion constant, abbreviated as *D* (Le Bihan, 2011; Mori, 2007). This diffusion constant depends upon the molecular weight, viscosity and temperature of the surroundings in which the molecule resides (Beaulieu, 2002).

This diffusion coefficient was first investigated by Fick in 1855 (Fick, 1855) where he found analogies of heat transfer phenomenon to diffusion in fluids. He proposed, which is known as, Fick's first law of diffusion stated as: If *F* is the transfer rate of a specific diffusing substance through a unit area of each section in a measured sample, *C* is the concentration of the diffusing substance and *x* is the coordinate in space normal to the section, then

$$J = -D\frac{\partial C}{\partial X} \qquad [1.1]$$

The proportionality term, *D*, is the diffusion coefficient. The negative sign implies that the diffusive flow is in the direction opposite to that of the increasing concentration. The SI units of *D* is m^2/s, but it is also common to associate *D* with units of cm^2/s or mm^2/s (Bernstein et al., 2004; Tofts, 2003; Stampfli, 2007). Equation [1.1] gives the relationship between the flux of the particles and the particle concentration gradient. Einstein's equation gives the relationship of finding a self-diffusing particle in 3D in a certain position at a certain time which is:

$$< R^2 >= 6Dt \qquad [1.2]$$

where $< R^2 >$ represents mean squared displacement in time *t* (Callaghan, 2011). In this case *D* represents the so called self-diffusion coefficient (Le Bihan, 2011; Mori, 2007). Equation [1.2] is obtained under the assumption of isotropic diffusion implying that the diffusing molecules have equal probability of diffusing in any direction without a preference and the diffusing particles perform a random walk of equal length in a constant time (Callaghan, 2011; Mori, 2007; Tofts, 2003).

In biological tissue, however, boundaries and obstacles represent barriers for diffusing molecules and hence affect the diffusion process (Filley, 2011; Nolte, 1999). In general, diffusion process is preferred along the boundary and restricted perpendicular to them (Le Bihan, 2011; Mori, 2007). Hence self-diffusing water molecule now has a preferred orientation in the presence of an obstacle resulting in an anisotropic diffusion. Hence in the case of anisotropic diffusion, the diffusion coefficient *D* is no longer a scalar and has a direction associated with it. In a 3D space, *D* can be represented as a 3x3 second order, symmetric tensor called as a diffusion tensor (Le Bihan, 2011; Mori, 2007).

Almost any MR imaging sequence can be designed to be sensitive to these self-diffusing water molecules by application of magnetic field gradients. The signal which is then obtained with the help of these sensitizing additional magnetic field gradients are

called as “diffusion weighted” MRI (dMRI) (Le Bihan, 2011; Mori, 2007). dMRI images are created with the help of pulsed magnetic field gradient introduced by Stejskal and Tanner (Stejskal and Tanner, 1956). The purpose of these gradient pulses is to magnetically label the spins carried by the self-diffusing water molecule. These labeled spins can now be considered as endogenous tracers that can be monitored in similar fashion as classical diffusion tracing techniques. However the measured signal is only sensitive, parallel to the direction of applied gradient and hence only represents the component of entire diffusion phenomenon.

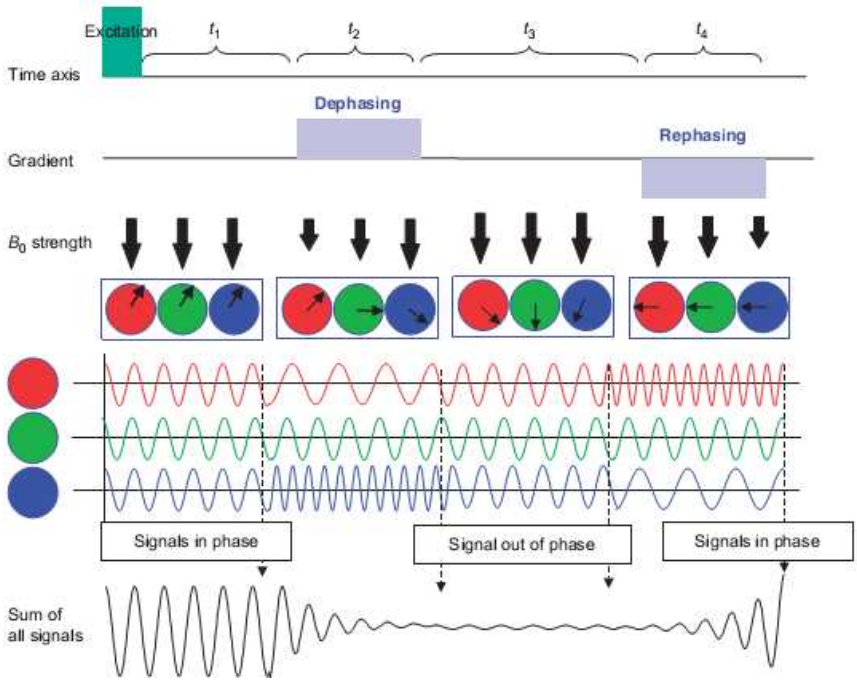

Figure 1.1: Thick arrow indicates the strength of the magnetic field (B0). Small arrows indicate the phase of the individual protons. Individual protons are represented by different circles in red, green and blue colors. Phase accumulated due to the application of gradient pulses is indicated by different arrows relative to each other from the starting point (Mori, 2007).

Figure 1.1 represents a diagrammatic approach to the measured diffusion weighted MR signal. In Figure 1.1, 3 different spins are represented by 3 different colors

as red, green and blue. In the absence of “dephasing” gradients (during time interval t_1), all the 3 spins are in phase with each other and aligned to the main magnetic field strength, B_0 and the signal read by MR receiver is maximum. With the application of dephasing gradients (during time interval t_2), different spins experience different magnetic field and hence have different phases relative to each other. During this time interval, the signal received at the MR receiver is less; as the out-of-phase spins now add destructively to produce MR signal. When the dephasing gradient is off (during the time interval t_3), all the 3 spins experience the same magnetic field B_0 but due to losing the phase because of the previously applied dephasing gradient; the signal received at the MR receiver is still less than that obtained during the time interval t_1. When the “rephasing” gradients are applied with same strength but opposite polarity as the dephasing gradients (during the time interval t_4), all the 3 spins experience different magnetic field with equal but opposite intensity as during t_2, and go back in-phase to give a signal that has similar intensity as during time interval t_1 at MR receiver. But if during the time interval of t_2 and t_4 the spins have diffused, the signal received at the MR receiver is less as compared to that at time interval t_1 as the number of spins from t_1 to t_4 are less as they have moved away from their initial locations giving rise to a “diffusion weighted” MR signal.

The amount of signal (S) received at the receiver because of application of gradient pulses relative to the signal in the absence of gradient pulses (S_0) can be given as $f(G,\Delta,\delta,\gamma,D)$ where G represents the magnitude of the applied gradient pulses, Δ and δ represents the separation and duration of the gradient pulses, γ represents the gyromagnetic ratio of water which is 42.58 MHz/Tesla and D represents the self-diffusion coefficient of water molecule (Callaghan, 2011; Le Bihan, 2011; Mori, 2007). The

probability of finding a spin at a location x_2 during the time interval Δ from its original location x_1 at time t_0 in one dimension, is Gaussian distributed and is given by:

$$P(x, \Delta) = \frac{1}{\sqrt{4\pi D\Delta}} e^{-\frac{x^2}{4D\Delta}} \quad [1.3]$$

where, $x = x_2 - x_1$ (Callaghan, 2011; Mori, 2007). The total signal measured by the MR receiver is the product of signal phase along x and the net population of spins in the measured voxel, given by

$S = \sum_x P(x,t)\Theta(x,t)$ where $\Theta(x,t)$ represents the phase accumulated by the spins inside the voxel during time interval, t. [1.4]

Equation [1.4] can be solved for measured signal, S, as:

$$S = \int_x P(x,t)\Theta(x,t)dx = \frac{1}{\sqrt{4\pi Dt}} \int_x e^{-\frac{x^2}{4Dt}} e^{i\gamma G(t)tx} dx \quad [1.5]$$

The total measured signal S, due to the application of the gradient pulse of duration δ, strength G and separation Δ can be solved from equation 1.5 giving:

$$S = S_0 \; e^{-\Upsilon^2 G^2 \delta^2 D(\Delta - \frac{\delta}{3})} \quad [1.6]$$

Substituting $\Upsilon^2 G^2 \delta^2 D(\Delta - \frac{\delta}{3})$ as "b", equation [1.6] can be rewritten as:

$$S = S_0 \; e^{-bD} \quad [1.7]$$

Hence from equation [1.7], one can non-invasively obtain the self-diffusion coefficient of water molecules inside the voxel with the application of "b" (Le Bihan, 2011; Mori, 2007). This *b-value* is governed by the gyromagnetic ratio of the water molecule, strength of the applied gradient, G, duration of the applied gradient, δ, and separation between the dephasing and the rephasing gradients, Δ. In theory, any MR imaging sequence can be designed to give a diffusion weighted image but practically, single shot

spin echo echo-planar imaging (SS-SE EPI) sequences are employed due to its insensitivity to motion, fast and relatively higher signal to noise ratio (Bernstein et al., 2004). A typical diffusion weighted MR sequence is shown in Figure 1.2. Unlike Figure 1.1, there is an 180^{o} radiofrequency (RF) pulse applied between the application of dephasing and rephasing gradients. Due to the presence of this 180^{o} RF pulse, the dephasing and the rephasing gradients now have the same polarity unlike Figure 1.1. However SS-SE EPI sequences suffer from low spatial resolution and susceptibility artifacts due to increased sensitivity at the vicinity of the air-filled structures to magnetic field inhomogeneities (Bernstein et al., 2004).

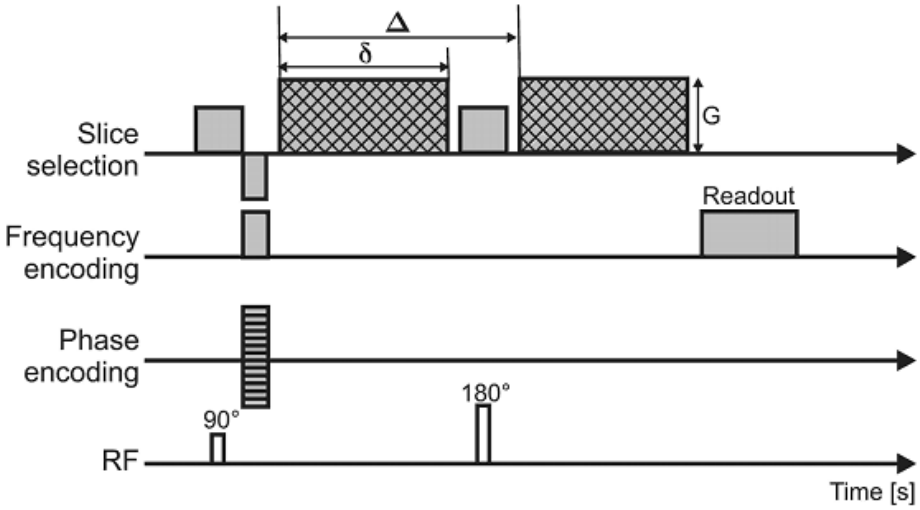

Figure 1.2: A typical spin echo diffusion sequence. Gradient pulses are represented by the hatched rectangles. The amount of diffusion weighting is governed by the gradient strength (G), the time (Δ) between the two gradient pulses and gradient duration (δ) (Stampfli, 2007).

The diffusion coefficient, *D*, measured from equation [1.7] is called as *apparent diffusion coefficient* (ADC) (Le Bihan, 2011; Mori, 2007). The measured diffusion coefficient is apparent since it is not the true intrinsic diffusion of the water molecule but rather depends on the interactions of the diffusing water molecules with the cellular

structures over a given diffusion time. As can be observed from equation [1.7], choice of *b-value* is a significant factor to accurately measure the ADC value. In a noise-free measurement, choice of *b-value* is has no influence in the estimation of ADC value but in practice, the measured dMRI signals are influenced by noise and choice of *b-value* becomes important. If the *b-value* is chosen to be very low, the precision of ADC estimation is low and if the chosen *b-value* is chosen to be very high, the acquired signal drops below the noise level resulting in underestimation of ADC value. The signal attenuation is a product of the applied *b-value* and the expected ADC and hence theoretically, there exists an optimum *b-value* for the expected ADC value. It has been shown that the optimal choice of *b-value* is in the range of ADCxb≈0.85 (Jones et al., 1999a). As the brain white matter ADC has a wide range of 0.35 to $1.3x10^{-3}$ mm^2/s, there is no one single *b-value* for all white matter tissue types. A tradeoff value of b=1000 s/mm^2 is widely used in clinical practice used in DTI studies of the human brain (Bernstein et al., 2004; Jones et al., 1999a).

1.5. From dMRI to Diffusion Tensor Imaging (DTI)

As mentioned previously, water molecules diffusing inside the brain have restricted diffusion due to the cellular microstructure of the tissue. Apart from the cellular microstructure of the tissue, there are various other compartments such as the extracellular space, intracellular space, presence of glial cells, neuronal cells and many other particles. All of these sources of hindrance affect the mobility of water diffusion and hence changes the diffusion properties. Earlier hypothesis suggested that the presence of myelin structures encasing the axons build a natural hindrance for the water molecules due to their limited permeability to water and hence diffusivity is restricted perpendicular to axons (Beaulieu, 2002). There is no such obstacle present along the length of the

axons. However it was shown that water diffusion was significantly anisotropic even in the normal, intact and non-myelinated olfactory nerve of the garfish (Beaulieu and Allen, 1994). dMRI studies in early brain development shows that anisotropy increases with increasing myelination of the axons (Dubois et al., 2008; Gao et al., 2009a; Huppi and Dubois, 2006; Lebel et al., 2008). Recently, it has been shown that anisotropy values are also influenced by axon diameters (Alexander et al., 2010; Assaf and Basser, 2005; Assaf et al., 2004), degree of myelination (Song et al., 2002) and fiber packing density (Schwartz et al., 2005). Hence the current literature suggests that the anisotropy obtained from dMRI within a neuronal tissue is mainly caused by high fiber density and axonal membranes which represent strong barriers for the water molecule to diffuse perpendicular to the main axis of the axons and the presence of myelin sheats around the axons.

This phenomenon of anisotropic diffusion is captured in the 3x3 second order, symmetric tensor known as diffusion tensor (Le Bihan, 2011; Mori, 2007). This tensor is represented as:

$$\mathbf{D} = \begin{pmatrix} D_{xx} & D_{xy} & D_{xz} \\ D_{yx} & D_{yy} & D_{yz} \\ D_{zx} & D_{zy} & D_{zz} \end{pmatrix} \quad [1.8]$$

The tensor in equation [1.8] can be represented as a diffusion ellipsoid where D_{xx}, D_{yy} and D_{zz} represents diffusion along X, Y and Z directions whereas the off-diagonal elements represents diffusion along i, j direction with i, j = X, Y and Z directions. Since the tensor is symmetric, there are 6 independent elements which have to be determined in order to estimate the tensor. Equation [1.6] can be rewritten as:

$S = S_0\ e^{-b\vec{g}^T D\vec{g}}$ where $\vec{g}$ is a normalized vector in the direction of the diffusion sensitizing gradient and $|g|$ is its corresponding strength (Le Bihan, 2011; Mori, 2007). [1.9]

Using the symmetric property of the diffusion tensor, equation [1.9] can be rewritten as:

$$-\ln(\frac{S}{S_0}) = b_{xx}D_{xx} + b_{yy}D_{yy} + b_{zz}D_{zz} + 2b_{xy}D_{xy} + 2b_{xz}D_{xz} + 2b_{yz}D_{yz} \quad [1.10]$$

Hence by acquiring at least 6 diffusion weighted images with non-collinear diffusion directions and one unweighted reference image (b_0 image), the 6 tensor elements can be calculated by solving the linear equation:

$$\boldsymbol{S = bD} \quad [1.11]$$

Where $\boldsymbol{S}$ is the signal attenuation vector, $\boldsymbol{S} = \begin{bmatrix} -\ln(S_1/G_1) \\ -\ln(S_2/G_2) \\ -\ln(S_3/G_3) \\ -\ln(S_4/G_4) \\ -\ln(S_5/G_5) \\ -\ln(S_6/G_6) \end{bmatrix}$ [1.12]

with $S_i=S_i/S_0$, G_i is the strength of the different gradients; **b** is the b-matrix, [1.13]

$$\boldsymbol{b} = \begin{bmatrix} (b_{xx}/G_1),(b_{yy}/G_1),(b_{xx}/G_1),(b_{zz}/G_1),(2b_{xy}/G_1),(2b_{xz}/G_1),(2b_{yz}/G_1) \\ (b_{xx}/G_2),(b_{yy}/G_2),(b_{xx}/G_2),(b_{zz}/G_2),(2b_{xy}/G_2),(2b_{xz}/G_2),(2b_{yz}/G_2) \\ (b_{xx}/G_3),(b_{yy}/G_3),(b_{xx}/G_3),(b_{zz}/G_3),(2b_{xy}/G_3),(2b_{xz}/G_3),(2b_{yz}/G_3) \\ (b_{xx}/G_4),(b_{yy}/G_4),(b_{xx}/G_4),(b_{zz}/G_4),(2b_{xy}/G_4),(2b_{xz}/G_4),(2b_{yz}/G_4) \\ (b_{xx}/G_5),(b_{yy}/G_5),(b_{xx}/G5),(b_{zz}/G_5),(2b_{xy}/G_5),(2b_{xz}/G_5),(2b_{yz}/G_5) \\ (b_{xx}/G_6),(b_{yy}/G_6),(b_{xx}/G_6),(b_{zz}/G_6),(2b_{xy}/G_6),(2b_{xz}/G_6),(2b_{yz}/G_6) \end{bmatrix}$$

and $\boldsymbol{D}$ is the vector containing the diffusion elements:

$$\boldsymbol{D^T} = \begin{bmatrix} D_{xx}, D_{yy}, D_{zz}, D_{xy}, D_{xz}, D_{yz} \end{bmatrix} \quad [1.14]$$

As shown in Figure1.3 (A), the diffusion tensor can be depicted as a diffusion ellipsoid (bottom panel). The eigenvalues and the eigenvectors of the tensor can be determined by singular value decomposition (SVD) algorithm. The eigenvector

corresponding to the largest eigenvalue points in the direction of the most pronounced diffusion direction. As mentioned previously, diffusion in the brain white matter is predominantly in the direction parallel to the underlying axonal fiber tracts and hence, DTI can be used to study course of directions of axons and the architecture of the brain white matter (Jones et al., 1999b).

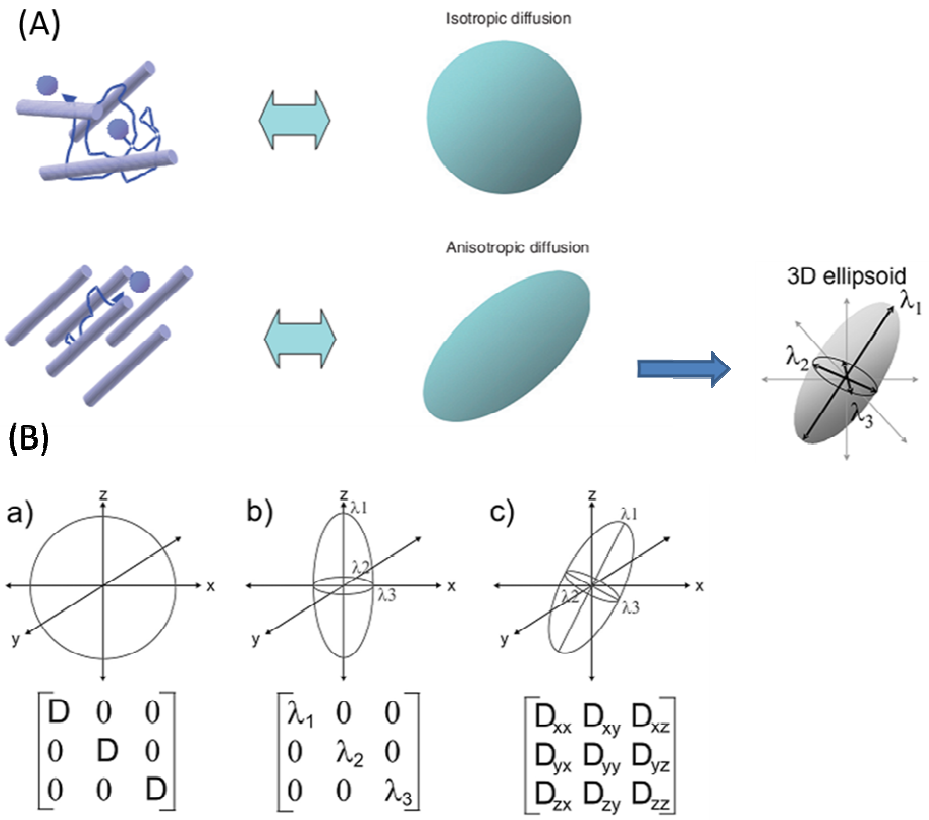

Figure 1.3: (A) In the absence of ordered barriers to free motion of water molecule, diffusion tensor can be represented as a sphere (top panel). The barriers to motion are represented by cylinders and water protons are represented by small circles. In the presence of ordered barriers, diffusion tensor can be represented by a 3D ellipsoid (bottom panel) (Mori, 2007). (B). (a) represents the isotropic tensor with equal elements along the diagonals of the tensor matrix; (b) represents the anisotropic tensor that does not have any cross-terms in the diagonal (perfectly aligned to the coordinate space); (c) represents the anisotropic tensor that has some angulation to the coordinate space.

1.6. Image Contrasts Derived from DTI

As can be seen that diffusion tensor, ***D***, has a lot of dimensions and it becomes a challenge to extract and visualize different information embedded inside the tensor data. Different grey scale images can be extracted from the diffusion tensor data as shown in Figure 1.4. These images are extracted from DTI images of a healthy individual. Of specific interests are the parameters which are objective and insensitive to the choice of orientation of the tissue structure within the laboratory frame and of the image scan plane, i.e., which are invariant to rotation and translation.

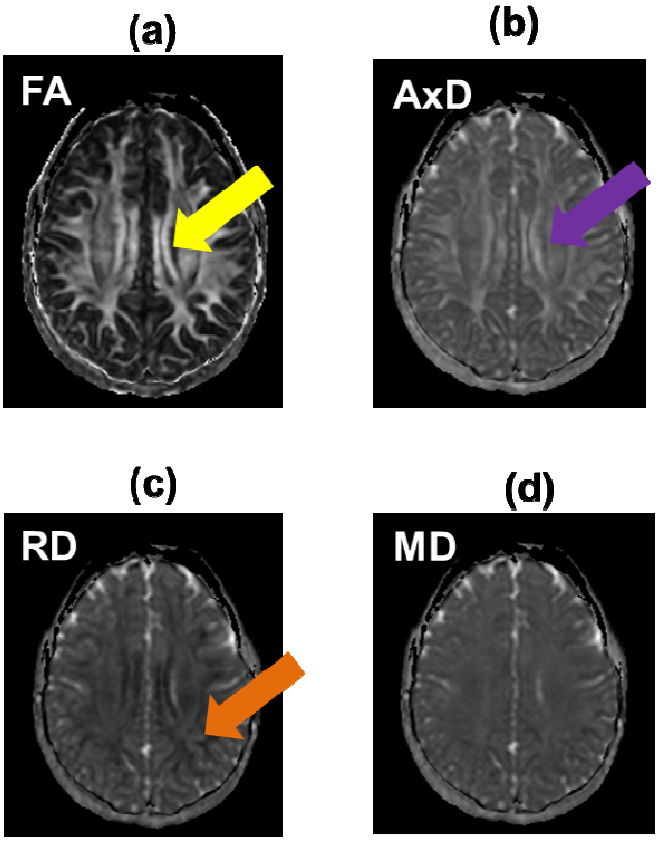

Figure 1.4: FA (a), AxD (b), RD (c) and MD (d) maps shown for a healthy adult. Yellow arrow in (a) represents the region of high FA; Violet arrow in (b) represents the region of high AxD; Orange arrow in (c) represents the region of high RD

One of the first derived quantities is called as mean diffusivity (MD), also denoted as <*D*>.

$$<D> = \frac{D_{xx} + D_{yy} + D_{zz}}{3} = \frac{Trace(D)}{3} \quad [1.15]$$

MD represents a "scale factor" indicating the elongation of the diffusion ellipsoid in 3D space. Within the cerebro-spinal fluid, diffusivity of the water molecules is isotropic and hence <*D*> is around $3x10^{-3}$ mm^2/s (Pasternak et al., 2009) whereas in the white matter, <*D*> is around $0.7x10^{-3}$ mm^2/s (Jones et al., 1999a).

Apart from MD, several other anisotropy indices which are dimensionless, rotationally invariant, independent of the orientation of the tensor and describe how much anisotropy is present in the voxel of measurement have been proposed (Basser et al., 1994a, b). One of the most widely used anisotropy indices is the fractional anisotropy (FA) index. It is defined as

$$FA = \sqrt{(\lambda_1 - \lambda_2)^2 + (\lambda_1 - \lambda_3)^2 + (\lambda_2 - \lambda_3)^2} \,/\, \sqrt{2(\lambda_1^{\,2} + \lambda_2^{\,2} + \lambda_3^{\,2})} \quad [1.16]$$

For a completely isotropic diffusion; FA will take the value of 0 and for a completely anisotropic diffusion; FA will take the value of 1. Other commonly used DTI derived contrasts are axial diffusivity (AxD) and the radial diffusivity (RD). AxD is the primary eigenvalue of the tensor, λ_1 and it is thought to describe the axonal integrity of the white matter structure. RD is the mean of the other 2 eigenvalues of the tensor, $\frac{\lambda_2 + \lambda_3}{2}$ and is shown to be sensitive to the myelination of the white matter tissue bundle.

As can be seen from Figure 1.4(a), FA map helps to extract the strength of the underlying anisotropy of the white matter bundles. The brighter the voxel or higher the FA is, the higher is the anisotropic whereas dark regions or voxels with lower FA represents

region of isotropic diffusion. One such region with high FA value is pointed by the yellow arrow. Thus as can be seen in Figure 1.4(a), ventricles are represented as dark regions, gray matter is either dark or light gray in color whereas white matter is bright in color. Although region of low FA can be seen as the region of low anisotropy, there are several other processes that might cause a drop in FA. As can be seen in Figure 1.5(a) pointed by the red arrow FA, in the region of the corona radiata where the fibers from cortico-spinal tract intersect the commissural fibers of the corpus callosum, is low. The FA of individual fibers is averaged and true individual anisotropy of these fibers is missing. This drawback of DTI will be discussed in further chapters and potential solution will be proposed. Also, as can be seen from Figure 1.4(b), AxD is higher where axons are arranged in the organized fashion (pointed by the purple arrow) while RD, as shown in Figure 1.4(c) is higher in the region where the diffusivity in the direction perpendicular to the axons is high (pointed by the orange arrow). Such regions can also be thought of as those white matter tracts that have weak myelination.

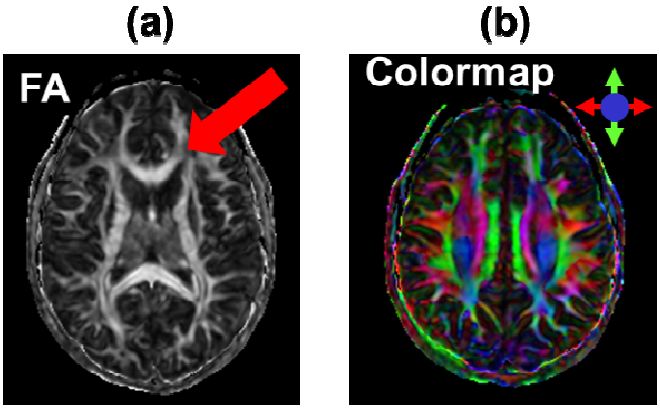

Figure 1.5: (a) Region of fictitious low FA pointed out by the red arrow due to the crossing of the corona radiate with the corpus callosum. (b) Colormap obtained by scaling the primary eigenvector by FA at the individual voxels. Red represents the fibers running in left-right direction, green represents the fibers running in anterior-posterior direction and blue represents the fibers running in foot-head direction

Figure 1.5(b) represents the color map obtained from a DTI image of a healthy individual. As mentioned previously, diffusion is sensitive to the application of the gradient directions and hence the orientation of the axons within the voxel can be visualized *in-vivo*. The brightness of the color map is obtained by scaling the primary eigenvector or the direction of the fastest diffusion, by the FA maps. Each color represents a direction. Red represents the fibers that run right-left direction; green represents the fibers that run in anterior-posterior direction and blue represents the fibers that run from top-bottom. The combination of RGB colors represents the intermediate directions.

1.7. *In-vivo* Dissection of White Matter Fiber Bundles from 3D Fiber Tractography

One of the main strengths of DTI is to visualize the orientation of the white matter fiber bundles *in-vivo* and it has been one of the active research areas of DTI. Fiber tracking opens the window to map axonal white matter fiber bundles within the brain white matter. This mapping is obtained by using the information encoded in the primary eigenvector representing the direction of fastest diffusion and strength of the anisotropy obtained from FA map. Figure 1.6(a) shows the graphical representation of the most commonly used fiber tracking algorithm known as Fiber Assignment by Continuous Tracking (FACT), also referred to as deterministic tracking (Mori, 2007; Mori et al., 1999). As shown in Figure 1.6, in order to trace a fiber; a continuous trajectory is traced step by step in the direction of the primary eigenvector within each voxel. A step size smaller than the size of the voxel is normally used and the propagation direction is interpolated based on the information of the primary eigenvectors of the adjacent voxels. In Figure 1.6(a), tracking was initiated within the light gray voxel resulting in the black pathway representing a reconstructed fiber. For instance, cingulum bundle traced using FACT is shown overlaid on a color map for a representative healthy subject in Figure 1.6(b).

Hence, we can potentially explore the connectivity network of the human brain using DTI techniques.

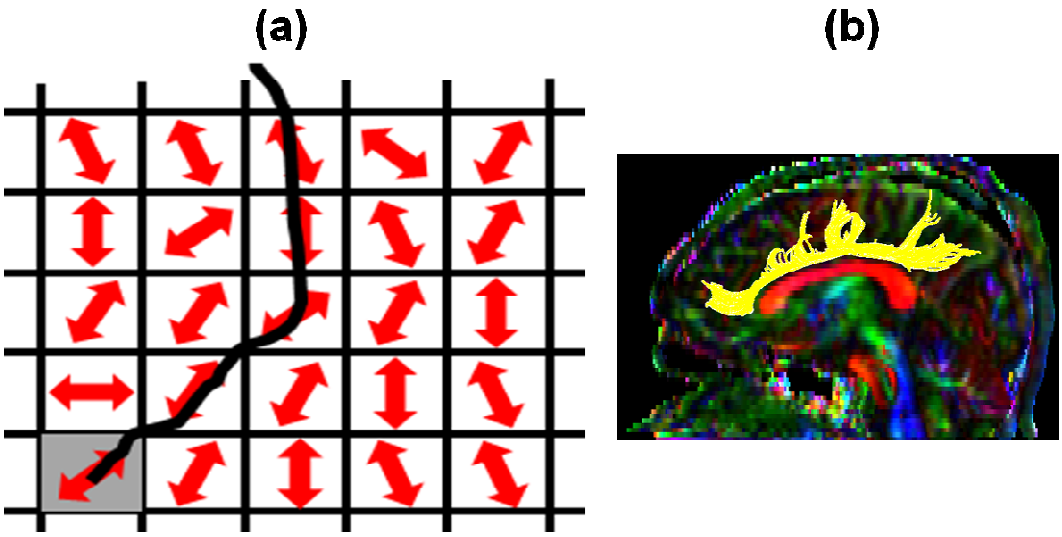

Figure 1.6: (a) Illustration of FACT or deterministic tracking technique. The tracking seed point was selected in the center of the gray voxel and the using the direction of the fastest diffusion or primary eigenvector, shown as arrows, the fiber shown in black color was delineated. (b) Cingulum bundle shown in yellow color overlaid on the color map of a healthy subject using the principle of FACT.

Although FACT is widely used in the clinical research to visualize the white matter fibers *in-vivo*, it can only resolve fibers with no crossing. The primary eigenvector information in regions where the fiber kiss, cross or diverge is biased and hence the fiber tracking obtained from FACT is biased. To resolve this issue, several techniques have been proposed; such as probabilistic tracking, fast marching techniques, tracking based on spherical harmonic decomposition of diffusion data (Tournier, 2011) and it continues to be an active research area.

1.8. Clinical Applications of DTI

Ever since the introduction of dMRI in clinical research it has been used extensively to investigate and treat several neurological disorders. DTI and dMRI images have become a routine for clinical assessment of acute stroke. Fast diagnosis is essential for stroke detection since necrosis of brain tissue can be stopped if perfusion to the damaged region can be restored quickly. As compared to normal T_1 and T_2 weighted MR images, contrasts such as MD provide improved contrast information (Baird et al., 1997; Baird and Warach, 1998; Schwamm et al., 1998; Wu et al., 2001).

Due to DTI's sensitivity to myelin, DTI has also been used to study multiple sclerosis (MS) extensively. FA and ADC maps have been shown to be different in MS patients as compared to normal controls (Filippi et al., 2001; Rovaris et al., 2002; Tievsky et al., 1999). DTI has been used extensively to study normal human brain development (Gao et al., 2009a; Huppi, 2011; Lebel et al., 2008), schizophrenia (Filley, 2011), Alzheimer disease (Choi et al., 2005; Jeon et al., 2012) and various other neuropathological diseases (Filley, 2001; Filley, 2011). Due to its inherent ability to build structural connectivity network of the human brain, DTI has recently been used to build human brain connectome to study brain disorders such as autism (Dennis et al., 2011) and normal human brain development (Hagmann et al., 2010) using graph theoretical approaches. Recently, fiber tracking information obtained from DTI has been used to provide information of the influence of the tumor on the adjacent white matter during surgical planning (Goebell et al., 2006; Helton et al., 2006; Witwer et al., 2002).

1.9. Objectives of this Research Work

1.9.1. Establish the Method of Dual-Tensor for Tract based Analysis (DTTA).

As mentioned in the above paragraphs, a most widely used DTI-derived metric quantifying white matter microstructure is FA, ranging from 0 to 1. FA with the current clinical scanning parameters severely underestimates the true microstructural properties at the regions of crossing-fibers (Ciccarelli et al., 2008; Horsfield and Jones, 2002; Tournier, 2011). While crossing-fiber voxels are estimated to take around 90% of entire brain white matter voxels (Jeurissen et al., 2012; Tournier, 2011), most models beyond single tensor (Alexander et al., 2010; Anderson, 2005; Assaf and Basser, 2005; Assaf et al., 2004; Dell'acqua et al., 2013; Douaud et al., 2011; Ennis and Kindlmann, 2006; Hosey et al., 2005; Jbabdi et al., 2010; Ozarslan et al., 2005; Peled et al., 2006; Sotiropoulos et al., 2008; Tournier et al., 2004; Tuch, 2004; Wedeen et al., 2005) were proposed to delineate tractography of the crossed fibers. Relatively fewer efforts have been made to restore the multi-FA values at the voxels of crossing-fibers. Voxelwise analysis of FA has been used extensively to investigate brain development or study brain pathologies (Ciccarelli et al., 2008; Eluvathingal et al., 2007; Horsfield and Jones, 2002; Huang et al., 2006). However, the white matter tracts connecting different brain regions have functional and clinical significance. In order to perform a tract-based analysis in clinical research, the tract of interest will be segmented through tractography and the FA values at the tract level and along the tract will be calculated to evaluate pathology or brain development. The aim is to establish a method capable of restoring FA at the regions of crossing-fibers for each tract with routinely used clinical diffusion imaging parameters.

1.9.2. Quantitatively Characterize the Microstructural Relationships of Human Brain White Matter Tracts during Development.

Various metrics such as FA, AxD, RD and MD derived from DTI are thought to reflect the microstructural integrity of white matter fibers across adults. They have also been used to study brain development and shown to correlate with aging, cognitive and behavioral performance (Beaulieu et al., 2005; Bonekamp et al., 2007; Goodlett et al., 2009; Hermoye et al., 2006; Klingberg et al., 2000; Lebel et al., 2008; Niogi et al., 2008; Salat et al., 2005; Snook et al., 2005). With DTI-derived metrics, it has been shown that asymmetry of the homologous tracts exist in the developing brain. However, these studies have primarily focused on assessing the group mean differences rather than correlation of the tracts itself (Gao et al., 2009a; Giorgio et al., 2010; Gong et al., 2005; Li et al., 2009; Powell et al., 2006; Rodrigo et al., 2007; Westlye et al., 2010; Wilde et al., 2009). Whether the white matter tract development is homogeneous for the homologous tracts or non-homogeneous is also unclear. The aim is to investigate the microstructural relationships of white matter tracts during early years of brain development. The hypothesis is that the microstructural relationships of human brain white matter tracts exists at early stages of brain development and the pattern of correlation as well as the strength of the correlation change significantly to support later functional activities of human brain.

1.9.3. Exploring the Perinatal Brain Network with Diffusion MRI and Graph Theory

Studies have shown in DTI images of perinatal brains that different white matter tracts exhibit different developmental pattern. Graph theoretical approach has been widely used to quantitatively characterize the dynamics of the brain networks (Bullmore and Sporns, 2009; Gong et al., 2009; He et al., 2007; He and Evans, 2010). The aim is to

build a structural brain connectome for developing brains between 31wg and 40wg with the graph theoretical approach that will give us insight into the connectivity changes during early brain development. The information of network nodes is obtained from consistent parcellation of the segmented brain cortex from DTI images and the edge information is obtained from the traced white matter tracts also from DTI images. The hypothesis is that significant changes of brain configurations occur during perinatal brain development. Measuring and comparing various network metrics at the early preterm can improve our understanding about early human brain development.

Chapter 2

Dual Tensor Tract Analysis (DTTA): Towards Application to Routine Clinical Diffusion MRI

2.1. Introduction

To accommodate the complex "wiring" in the human brain with volume of around 1.2 liters, significant amount of white matter (WM) fibers need to cross with each other. Diffusion magnetic resonance imaging (dMRI) in routine clinical research is usually acquired within limited time of less than 5 minutes and with relatively low b value such as 1000s/mm^2. The voxel size of these datasets is usually from 2x2x2mm^3 to 3x3x3mm^3 and hence large proportion of WM voxels has crossing fibers. It is believed that almost half of brain voxels contain crossing fibers (Tournier, 2011). Fractional anisotropy (FA) (Basser et al., 1994b) derived from the single tensor model and ranging from 0 to 1, has been widely used to quantify the WM microstructural changes associated with many neurological or psychiatric disorders. However, WM microstructural integrity at the crossing-fiber regions (CFR) has been significantly underestimated (Jbabdi et al., 2010; Tuch et al., 2005; Wheeler-Kingshott and Cercignani, 2009) with single tensor (ST) FA.

In the past few years, a number of techniques have been developed through innovation of imaging and modeling to address the crossing-fiber problem. The notable imaging techniques include Q-ball imaging (Tuch, 2004), diffusion spectrum imaging (Wedeen et al., 2005) and multi-b diffusion imaging (Alexander et al., 2010). The representative modeling techniques beyond single tensor include multi-tensor (Hosey et al., 2005; Peled et al., 2006; Sotiropoulos et al., 2008), diffusion kurtosis (Jensen et al., 2005) and high order tensor (Liu et al., 2004; Minati et al., 2007; Minati et al., 2008). Many of these models require high b value and high angular resolution diffusion imaging (HARDI) for data acquisition. Moreover, a significant proportion of technologies have

been developed specifically to improve tractography (Alexander, 2005; Anderson, 2005; Behrens et al., 2007; Hosey et al., 2005; Lazar and Alexander, 2005; Tournier et al., 2004; Tuch, 2004; Wedeen et al., 2005) with no tract specific metric measurement. Relatively fewer studies have focused on improving metrics from dMRI. To name a few, they include generalized fractional anisotropy (GFA) (Fritzsche et al., 2010; Tuch, 2004; Zhan et al., 2010), generalized anisotropy (GA) (Ozarslan et al., 2005), mode of anisotropy (Douaud et al., 2011; Ennis and Kindlmann, 2006) and fractions (Hosey et al., 2008; Jbabdi et al., 2010). However, so far there is no widely accepted alternative scalar measure that can replace ST FA and which is not sensitive to crossing-fibers.

Moreover, it was shown (Pasternak et al., 2009) that free water or the isotropic contribution can severely underestimate the FA estimated in the dMRI voxels. Hence it becomes imperative to estimate the isotropic contribution in the dMRI voxels and report FA that is not affected by free water contamination. However, all the techniques focused on providing an alternative scalar measurement to FA at CFR do not correct for free water or the isotropic contribution in the CFR. .

Recently technologies of tract analyses including tract statistics (Colby et al., 2012; Goodlett et al., 2009; Yushkevich et al., 2008; Zhu et al., 2011), tract morphometry (O'Donnell et al., 2009; Zhang et al., 2010) and tract metric analysis as in our previous studies (Delgado-Ayala et al., 2012; Huang et al., 2012a; Huang et al., 2011; Huang et al., 2012b) have become important due to great clinical significance of the tracts. However, most of the techniques beyond ST FA in the literature (Alexander, 2005; Anderson, 2005; Behrens et al., 2007; Ennis and Kindlmann, 2006; Fritzsche et al., 2010; Ozarslan et al., 2005; Tuch et al., 2005; Zhan et al., 2010) were developed for the voxelwise analysis. Although few of them were designed for tract analysis, there was no delineation of multi-anisotropy values for the crossed fiber tracts in a single voxel. In

addition, most of these studies either improving tractography (Alexander, 2005; Anderson, 2005; Behrens et al., 2007; Hosey et al., 2005; Tournier et al., 2004; Tuch, 2004; Wedeen et al., 2005) or proposing new metrics (Douaud et al., 2011; Ennis and Kindlmann, 2006; Fritzsche et al., 2010; Hosey et al., 2008; Jbabdi et al., 2010; Ozarslan et al., 2005; Tuch, 2004; Zhan et al., 2010) were performed at the cost of high b value, high angular resolution and long scan time that are not suitable for clinical research. Due to extensive applications of FA in neurological and psychiatric studies such as phenotype characterization, drug testing and therapy monitoring; biased conclusions from the underestimated ST FA in tract analysis can have significantly negative impacts on these studies. Hence it is critical to develop methods which can correct the underestimated FA in these clinical studies and are designed for tract analysis.

In this study, a clinically applicable, partial volume and free water contamination corrected dual tensor model for tract analysis of dMRI is proposed. The proposed novel **D**ual **T**ensor-based **T**ract **A**nalysis (DTTA) is capable of estimating unbiased dual anisotropy in a single voxel at crossing-fiber regions (CFR) and is adapted for tract analysis. DTTA is tested with the data from dMRI in clinical research obtained from 3T Philips and 3T GE scanners with 30 and 25 diffusion encoding gradient directions. Dual tensor Gaussian mixture model was used in DTTA. With input of dMRI, DTTA fully characterizes the two tensors at CFR which carry more information than just multiple primary eigenvectors for tractography and detaches the crossed fibers for tract analysis. A digital phantom was designed and human dMRI with multiple b values were acquired to evaluate the accuracy of estimated anisotropy at CFR after DTTA correction. FA measurements from dual tensors at a single voxel were estimated and implemented in DTTA for tract analysis. In addition, the estimation of dual tensor anisotropy has been optimized under the framework of clinical dMRI with low b value and acquired within 5

minutes. The results from digital phantom study showed high accuracy of the corrected DTTA anisotropy. The results from normal human dMRI study indicated effective correction of underestimated anisotropy at CFR.

2.2. Materials and Methods

2.2.1. Overview of DTTA

The DTTA technique includes two major components namely Gaussian mixture dual-tensor model with Levenberg-Marquardt (LM) fitting and tract analysis. Figure 2.1 schematically illustrates this method. The WM microstructure is significantly underestimated at the CFR with the single tensor FA (Figure 2.1a). After identification of the voxels of CFR in Figure 2.1a, dual-tensor fitting was conducted as shown in Figure 2.1b. The crossed tracts were then detached in Figure 2.1c with one of the two DTTA anisotropy values assigned to each tract based on the alignment of the primary eigenvector of the tensors in the crossing-fiber voxel to the primary eigenvectors of the tensor in the surrounding voxels. In Figure 2.1c, the DTTA anisotropy profiles of the two crossed tracts were obtained and they were usually more uniform than the ST FA profile of the same tract.

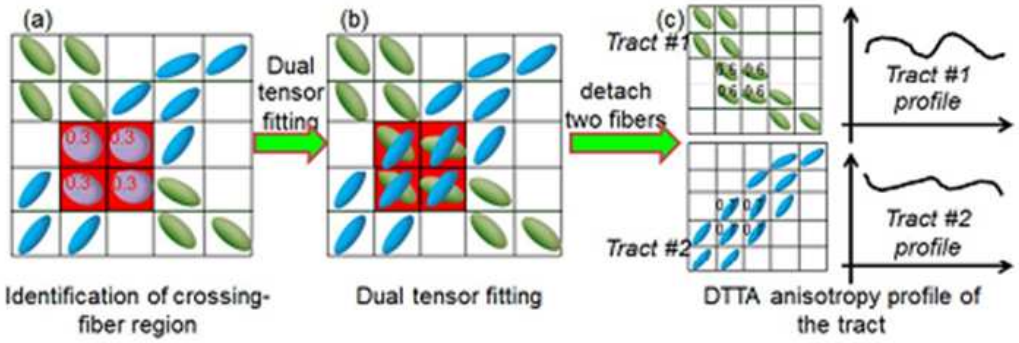

Figure 2.1: Diagram of tract analysis. Low FA value (0.3) at the red voxels from single tensors in (a) can be corrected by multi-FA values from multi-tensor in (b), each of which is associated with a unique blue or green tract. For tract analysis, the crossed fibers (red voxels in (a) and (b)) in a single data volume can be detached into multiple tracts (blue and green tract in (c)) in multiple volumes, each of which contains only one tract (c). Tract profile can be obtained (c). Different colors of ellipsoids indicate diffusion tensors of two unique tracts. The corrected multi-FA values (0.6 and 0.7) at the end voxels in (a) and (b) belong to two different tracts.

2.2.2. Signal Modeling and Test with the Digital Phantom

2.2.2.1. Gaussian Mixture Signal Model and Fitting of the Model

A simplified Gaussian mixture signal model (Alexander et al., 2010; Hosey et al., 2005; Hosey et al., 2008) was used for the CFR voxels as follows,

$$S = S_0(f_{iso}e^{-bD_{iso}} + f_1 e^{-b\overline{G_i}^T \overline{\overline{D_1}}\,\overline{G_i}} + (1 - f_1 - f_{iso})e^{-b\overline{G_i}^T \overline{\overline{D_2}}\,\overline{G_i}}) \quad [1]$$

where f_1 and f_{iso} are the volume fractions of the first fiber bundle and isotropic compartment, b is the applied b value, S_0 is the signal with no diffusion weighting, D_{iso} is the diffusion coefficient of the isotropic component in the voxel, $\overline{G_i}$ is the *ith* gradient vector with *i* as the direction of the acquisition, $\overline{\overline{D_1}}$ and $\overline{\overline{D_2}}$ are the two tensors representing the first and second fiber bundles. As can be seen, this is a Gaussian signal mixture model where the signal measured in the voxel is a combination of two fiber bundles and an isotropic component. The exchange of the protons within the voxel

between the two fibers is assumed to be in the slow exchange regime that might be expected for spatially distinct tissues. $\overline{\overline{D_1}}$ and $\overline{\overline{D_2}}$ are formulated from their eigenvalues E_1=diag[λ_{11}, λ_{21}, λ_{31}], E_2=diag[λ_{12}, λ_{22}, λ_{32}] and rotations $\boldsymbol{R_1}$, $\boldsymbol{R_2}$ by $\overline{\overline{D_i}} = \overline{R_i^T} E_i \overline{R_i}$.

Rotation around x, y and z axes is given by $\overline{R_i} = \overline{R}_{x(\alpha_1)} \overline{R}_{y(\alpha_2)} \overline{R}_{z(\alpha_3 \pm \alpha_4)}$, i=1,2 for $\overline{\overline{D_1}}$ and $\overline{\overline{D_2}}$ respectively, where α_k, k=1,2,3, represent the orientation of the plane in which the principal eigenvectors of the two tensors reside and $2\alpha_4$ is the angle between the two primary eigenvectors of $\overline{\overline{D_1}}$ and $\overline{\overline{D_2}}$. We hypothesized that f_{iso} is a linear function of mean apparent diffusion coefficient (mADC) with the details described below and f_{iso} in the voxel was estimated *apriori* from mADC. The diffusivity of the isotropic component, $D_{iso,}$ in the voxel was assumed constant at $3x10^{-3}$ mm^2/s (Pasternak et al., 2009). By assuming the same axial diffusivity for the two tensors and same radial diffusivity for each individual tensor (Caan et al., 2010), the 12 independent variables in equation [1] were reduced to 8 independent variables, namely λ_{1i} *(i=1,2),* λ_{21} *(equal to* λ_{31}*),* λ_{22} *(equal to* λ_{32}*)*, α_1, α_2, α_3, α_4, f_1. In-house software incorporating LM estimation algorithm was used for fitting these 8 independent variables. In order to test the goodness-of-fit and measure the similarity between the fitted dual tensors and the measured diffusion profile, we set a fitting error metric $\left(\sum_{i=0}^{N_{dir}} \left(\left| S_i - S_i^f \right| / S_i \right) \right) / N_{dir}$, where N_{dir} was the total number of gradient directions, S_i was the measured signal of ith gradient direction of dMRI, and S_i^f was computed from the fitted dual tensor model. LM fitting was iterated until fitting error metric less than 0.05 was achieved for high quality of global fitting convergence. If this metric is greater than 0.05 after 100 times of iterations of LM estimation, the voxel is considered as a non-CFR voxel. If the error from DTTA is less than that from ST model, then a further quantitative step was performed to check for over-fitting of the model. This was

done using the Akaike Information Criteria (AIC) (Akaike, 1992) described in detail below. If the voxel fail the AIC test, then that voxel was marked as non-CFR voxel. Of note, the non-CFR voxel marked due to high fitting error or over fitting of the model can have more than 2 fiber crossings. Since the assumed DTTA signal model explicitly models only the voxels that have 2 fiber crossings, all such voxels with more than 2 fiber crossings will retain the FA estimated from ST model.

2.2.2.2. Identification of the CFR:

The planar index Cp, given by $Cp = 2(\lambda_2-\lambda_3)/(\lambda_1+\lambda_2+\lambda_3)$, calculated from the eigenvalues of the single tensor was used to identify CFR voxels. All the voxels where $Cp>0.2$ were marked as CFR voxels (Peled et al., 2006; Sotiropoulos et al., 2008).

2.2.2.3. Evaluating the Model Fit

The result of the nonlinear fitting was quantitatively evaluated to check for over-fitting of the tensors with two techniques. This was firstly done with the help of previously mentioned goodness-of-fit technique and secondly, using the AIC. Briefly, AIC compares the sum of squares obtained using the DTTA fitting to the sum of squares obtained using the ST fit and this is further compared against the loss of degrees of freedom due to the more complicated DTTA model. AIC is computed using the equation [2] where N is the number of data points which is equal to the number of diffusion encoding gradients, K is the number of parameters fit by the regression plus one (7 in case of ST model and 9 in case of DTTA model) and SS is the sum of the square of the vertical distances of the points from the curve.

$$AIC = N.\ln(\frac{SS}{N}) + 2K \qquad [2]$$

In order to compare the two models, equation [3] is used that compares the change in AIC value.

$$\Delta AIC = N.\ln(\frac{SS_{DTTA}}{SS_{ST}}) + 2.(K_{DTTA} - K_{ST}) \quad [3]$$

If ΔAIC is negative, then DTTA model was chosen for the CFR voxel otherwise ST model was retained for the CFR voxel.

2.2.2.4. Estimation of f_{iso} in the CFR

f_{iso} was estimated as a linear function of mADC obtained from routine clinical dMRI with only low b value. The following linear equation was used to characterize the relationship of f_{iso} and *mADC*: f_{iso} =c1**mADC*+c2, where c1 and c2 are two fixed scalar coefficients. Two-shell (b=1000s/mm^2 and b=2500s/mm^2) dMRI data (acquisition procedure described in details below) of 5 normal subjects were used for calculating c1 and c2. Specifically, for each WM voxel, f_{iso} was estimated from nonlinear LM fitting of Gaussian mixture model using the two-shell dMRI data. .mADC was measured with low b (1000s/mm^2) dMRI data. Then the linear fitting was conducted for voxels in whole brain WM and c1 and c2 were estimated which were assumed to be constants for all WM voxels across the subjects. f_{iso} was estimated in all the non-CFR voxels by the technique described in (Pasternak et al., 2009).

2.2.2.5. Calculation of FA1, FA2 and Weighted DTTA Anisotropy at the CFR and ST FA at the Single-Fiber Region

After multi-tensor fitting, FAi (i=1, 2) (Pierpaoli and Basser, 1996) of each tensor was calculated using the equation

$$FAi = \sqrt{(\lambda_{1i} - \lambda_{2i})^2 + (\lambda_{1i} - \lambda_{3i})^2 + (\lambda_{2i} - \lambda_{3i})^2} \,/\, \sqrt{2(\lambda_{1i}{}^2 + \lambda_{2i}{}^2 + \lambda_{3i}{}^2)} \quad [4]$$

Weighted DTTA anisotropy was calculated by the following equation, $(f_1*FA1+(1-f_{iso}-f_1)*FA2)/(1-f_{iso})$. It represents the weighted anisotropy of the fitted two tensors in a single voxel. The average weighted DTTA from different subjects was obtained by using nonlinear registration function (FNIRT) from FSL (www.fmrib.ox.ac.uk/fsl). Equation [4]

was also used for ST FA calculation at the single-fiber region and λ_1, λ_2 *and* λ_3 were eigenvalues of the single tensor obtained from linear least square fitting.

2.2.2.6. Test with the Digital Phantom

To test the feasibility of obtaining accurate dual FA values from dual tensor fitting with diffusion signals acquired in a clinical research framework, i.e. relatively low b value (1000s/mm^2) and reasonable signal-to-noise ratio (SNR), a digital phantom was generated with equation [1]. The four variables used for the phantom design and their detailed values were as follows: $2\alpha_4$=10, 20,• • •90, f_1=0.1, 0.2,• • •0.9, FA1=0.2,• • •0.9; FA2=0.2, • • •0.9, where FA1 and FA2 were the fractional anisotropy of the two tensors. To match *in vivo* human data, Jones 30 gradient scheme (44) with 30 diffusion encoding gradient directions was used to generate 30 dMRI volumes and one non-diffusion weighted, b0 image. b-value was 1000 sec/mm^2. To understand the influence of noise on the proposed model, Rician noise was added to the simulated signal generated from equation [1] by adding Gaussian noise with different standard deviation to both real and imaginary part of the simulated signal in k-space (45). The resultant SNR varied from 10 to 70.

2.2.3. dMRI of In-vivo Human Brain

2.2.3.1. Normal Subjects

17 healthy young adults (age: 24.4±3.3), free of current and past medical or neurological disorders, were recruited at Advanced Imaging Research Center of the University of Texas Southwestern Medical Center. All human subjects gave informed written consents approved by the Institutional Review Board.

2.2.3.2. Data Acquisition

A 3T Philips Achieva MR system was used to acquire dMRI data. A single-shot echo-planar imaging (EPI) sequence with SENSE parallel imaging scheme (SENSitivity Encoding, reduction factor =2.5) was used. dMRI of all human subjects were acquired with the following parameters, b value = 1000 s/mm^2, imaging matrix=112×112 zero filled to 256×256, field of view=224×224mm (nominal resolution of 2mm), slice thickness =2mm without gap, slice number=65, axial acquisition parallel to the anterior-posterior commissure line (AC-PC). For comparison, dMRI of a higher b value were also acquired at b=2500 s/mm^2 from 7 out of the 17 healthy controls with same delta values, δ=17.4ms and Δ=39.9ms, as those used for b=1000 s/mm^2. Different diffusion gradient strengths, G=36mT/m and G=57mT/m were used for b=1000 and 2500 s/mm^2 respectively. To ensure enough SNR, two repetitions were used for dMRI with b-value of 2500 s/mm^2. TR=9.5s and TE=80ms were used for all dMRI with different b values. Jones 30 gradient scheme (Jones et al., 1999a) with 30 diffusion encoding gradient directions was used to generate 30 dMRI volumes and one non-diffusion weighted, b0 image. A 3T GE Signa MR system was also used to acquire dMRI data of 10 healthy subjects to compare the results across the scanners. A single-shot echo-planar imaging (EPI) sequence with GRAPPA parallel imaging scheme (GRAPPA acceleration factor = 3) was used. dMRI were acquired with the following parameters: b value = 1000 s/mm^2, imaging matrix=96×96 zero filled to 256×256, field of view=240×240mm (nominal resolution of 2.5mm), slice thickness =2.5mm without gap, slice number=60, axial acquisition parallel to the anterior-posterior commissure line (AC-PC). 25 diffusion encoding gradient directions was used to generate 25 dMRI volumes and one non-diffusion weighted, b0 image. Other imaging parameters on 3T GE was TR = 16.5s, TE = 84.4ms, diffusion

gradient strengths of G=36mT/m and same delta values, δ=17.4ms and Δ=39.9ms as 3T Philips Achieva MR system.

2.2.4. Tract Analysis

2.2.4.1. Tractography

Probabilistic tractography (Behrens et al., 2007) was conducted on left inferior fronto occipital fasciculus (IFO), inferior longitudinal fasciculus (ILF), cortico-spinal tract (CST), uncinate fasciculus (UNC) and superior longitudinal fasciculus (SLF) which are known to have CFR along their paths. The ROI for tracing these tracts were drawn by following the literature (Wakana et al., 2007). These ROI were then fed into *probtrackx* module of FSL (http://fsl.fmrib.ox.ac.uk/fsl/fslwiki/FDT). Only those voxels that had a value greater than 1% of the waytotal were retained and binarized. The binary masks from the traced left CST, IFO, UNC, ILF and SLF were used for comparisons of the tract specific DTTA anisotropy (FA1 or FA2) and ST FA.

2.2.4.2. Tract-Specific Anisotropy

Selection of FA1 or FA2 in the voxels at the CFR was determined by the orientations of the primary eigenvectors of the two tensors. Specifically, the FAi (i=1, 2) of the individual tensor whose primary eigenvector aligned best to those of the surrounding voxels was selected. The alignment of the eigenvectors was quantified by the dot product of the two eigenvectors. The best alignment of an eigenvector resulted in the maximum summation of the dot products of this eigenvector and surrounding eigenvectors. The underlying hypothesis is that the fiber orientations in a tract are continuous and well aligned. This procedure resulted in one tract-specific FA for the specific tract in each crossing-fiber voxel.

2.2.4.3. Tract Analysis

Each voxel in left UNC, IFO, ILF and SLF was categorized as single-fiber voxel or crossing-fiber voxel by the approach described above. DTTA anisotropy at the CFR which is specific to a certain tract and ST FA at the single-fiber voxel was calculated. The procedure was repeated for 17 low-b dMRI data of healthy young volunteers. For each tract, the tract voxels of all subjects were evenly sampled, resulting in a group of single-fiber FA values, crossing-fiber FA values before DTTA correction and crossing-fiber FA values after DTTA correction.

2.2.4.4. Along-the-Tract Analysis

The traced left CST was used as a binary mask for the following calculation. Mean and standard deviation of the following metrics at certain axial planes along the inferior-superior axis of left CST were calculated. Before DTTA correction, ST FA, generalized FA (GFA) (Fritzsche et al., 2010; Tuch, 2004; Zhan et al., 2010) and generalized anisotropy (GA) (Ozarslan et al., 2005) were calculated along the CST from low b ($b=1000s/mm^2$) dMRI data of 17 healthy subjects acquired from Philips MR system. Same procedure was repeated for dMRI data of 10 healthy subjects acquired from GE MR System. DTTA was then applied to the same dMRI data to obtain the DTTA-corrected tract profile. Furthermore, to test the benefit of multi-shell dMRI with regards to the anisotropy correction, we applied DTTA to obtain the corrected anisotropy along the left CST from the multi-shell ($b=1000$ and $2500s/mm^2$) dMRI of 7 out of 17 healthy subjects. The profiles of all these metrics along the left CST were plotted. In addition, mean and standard deviation of these metrics at all left CST voxels were calculated to compare the consistency of these metric values inside the same tract.

2.3. Results

2.3.1. Digital Phantom Test and f_{iso} Estimation

Figure 2.2a shows that bias for estimating two anisotropy values is less than 5% for almost all cases with SNR greater than 35 (pointed by green arrow) and separation angle greater than 30 degrees. Under the similar condition, the fitting errors of volume fractions f_1 are less than 5% for almost all cases in Figure 2.2b. The known ground truth in Figure 2.2a and Figure 2.2b is represented by the dashed line. The fitting algorithm was tested to be robust with error less than 5% for almost all cases in the range of FAi (i=1 or 2) from 0.2 to 0.9 and volume fractions from 0.2 to 0.9 in the simulated voxel. For simplification, the results of several selected combinations of two tensors are shown in Figure 2.2.

The regression plots of f_{iso} estimated from two shell dMRI data and mADC of voxels of whole brain WM of 5 subjects are shown in Figure 2.3. The linear correlation is statistically significant ($p<0.0001$) for all three plots. For f_{iso} estimation with routine clinical dMRI, the ones from whole brain WM were used.

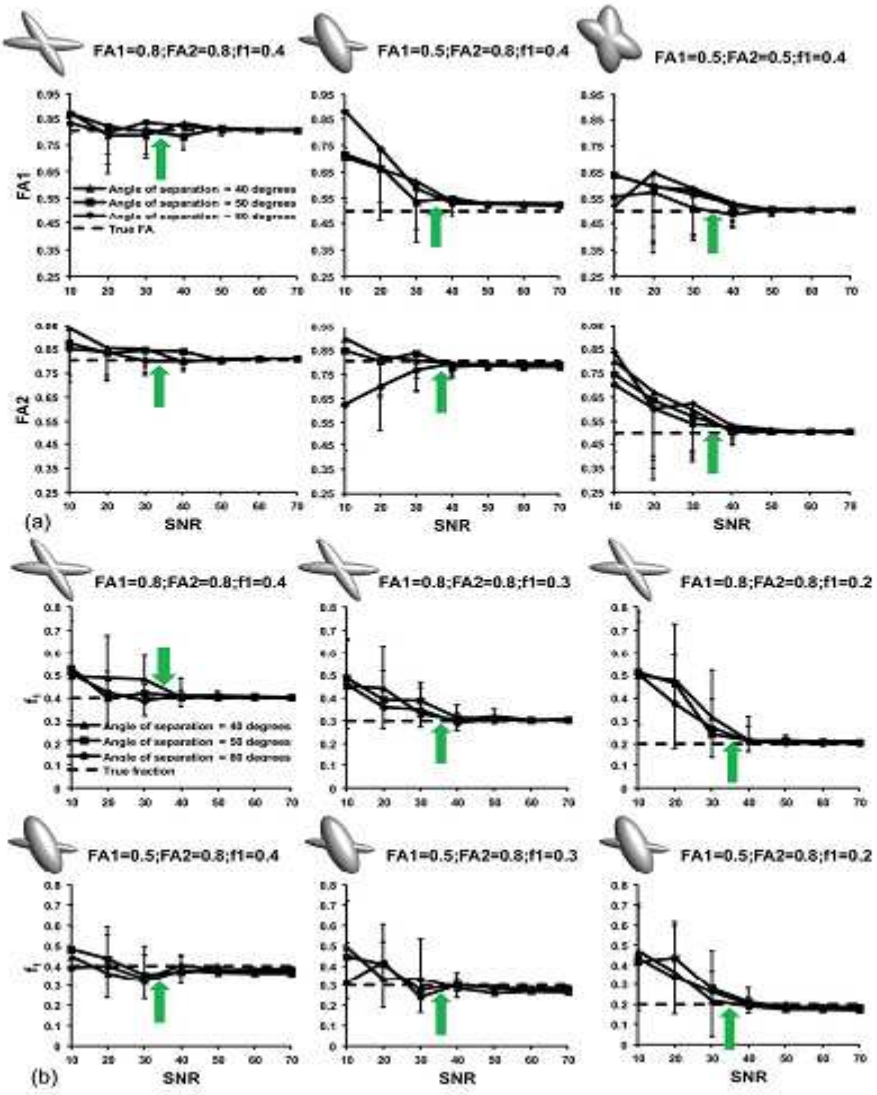

Figure 2.2: (a) Estimation of FA1 and FA2 of two crossing fiber components at different SNR and separation angles (40, 50 and 80 degrees). Left, middle and right panels represent different combinations of ground truth FA1 and FA2. (b) Estimation of f1 at different SNR and separation angles (40, 50 and 80 degrees) with two typical combinations of FA1 and FA2 in the upper and lower panels. Dashed lines are true FA values (a) and true f1 (b). Green arrows indicate the SNR above which the fitting becomes accurate and stable.

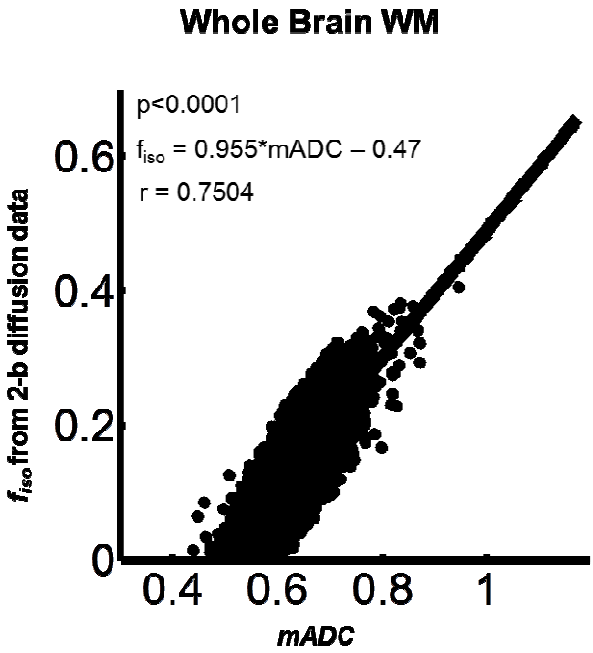

Figure 2.3: Linear regression between f_{iso} estimated from 2-b diffusion data and mADC is shown for whole brain white matter (WM) voxels. The dots represent evenly sampled points from whole brain WM voxels from 5 subjects and the black line represents the linearly fitted line

.

2.3.2 Comparison of the Primary Eigenvector and Diffusion Profile at CFR Obtained Using ST Model, DTTA Model and Ball and Stick Model from FSL

Figure 2.4 shows the FA map from a coronal slice of a typical healthy subject with CFR region shown by the white rectangular box. The primary eigenvector at CFR obtained from ST model and the two primary eigenvector obtained from ball and stick model (BSM) implemented in the FDT module of FSL and DTTA model are shown in the upper panel. The diffusion profile in the CFR obtained from ST model, BSM model and DTTA model overlaid on the FA map is shown in the lower panel. As shown in the upper panel, the primary eigenvector obtained from ST model fails to find the primary eigenvector of the crossed fibers. However, both BSM and DTTA model can estimate the

primary eigenvector of the crossing fibers in the CFR with almost similar orientations. Moreover DTTA model can estimate the diffusion profile of the crossing fibers as shown in the two rightmost lower panels which cannot be estimated either by ST model or BSM model. Hence it is clear from Figure 2.4 that DTTA model can estimate both the primary eigenvectors and the diffusion profile at CFR.

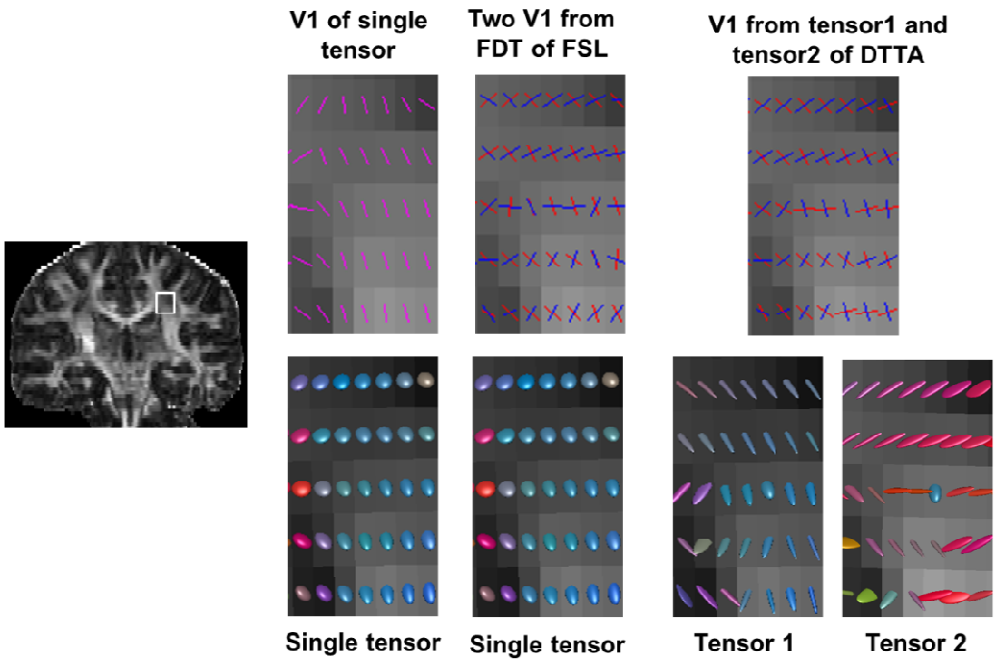

Figure 2.4: Coronal slice of a healthy subject is shown in the leftmost panel with the CFR highlighted by the white rectangular box. Eigenvectors obtained from ST model, FDT model of FSL and DTTA model are shown in the top panel and the diffusion profiles of the fiber tracts in the CFR obtained from ST model, FDT model and DTTA model are shown in the bottom panel.

2.3.3. Weighted DTTA Anisotropy Compared to Single Tensor FA

The upper panels in Figure 2.5 show the averaged single tensor FA maps acquired from 17 subjects with dMRI of b value 1000 s/mm^2 , and the lower panels show the averaged weighted DTTA anisotropy after applying DTTA technique to the voxels of the CFR with the same dMRI datasets. As indicated by the red arrows in upper panels of

Figure 2.5, the ST FA values were significantly lower at the CFR compared to surrounding regions, potentially conveying biased information on white matter microstructural integrity. The weighted DTTA anisotropy at a crossing-fiber voxel is not specific to a tract, but reflects the corrected microstructural integrity of that voxel. It is clear from Figure 2.5 that underestimated anisotropy values were restored with weighted DTTA anisotropy values at the CFR and they appear more homogeneous to the anisotropy values of surrounding single fiber regions.

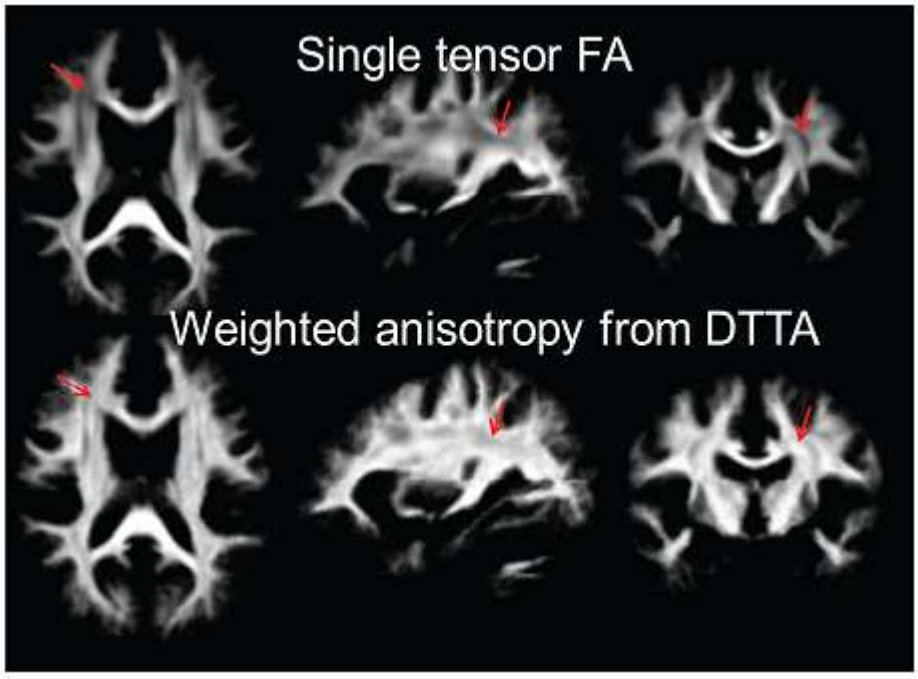

Figure 2.5: Single tensor FA (upper panels) and weighted anisotropy from DTTA (lower panels) averaged from low b DWI from 10 subjects. The red arrows point to some typical regions with apparently lower single tensor FA due to fiber crossing. Compared to single tensor FA, weighted anisotropy from DTTA provides unbiased measure of WM integrity at the CFR in the entire brain.

2.3.4. Tract Analysis of DTTA

2.3.4.1. Tract Based Analysis

The two columns below each tract in the lower panel of Figure 2.6 show the FA values at the evenly sampled voxels for 17 subjects before (pink “+”) and after (red circle) applying the DTTA technique to crossing-fiber voxels. The unbiased single-fiber FA values (blue dots) from the same tracts were put in both columns as references. As can be seen in the lower panel of Figure 2.6, single tensor FA values at the CFR (pink “+”) cluster are severely underestimated and fall below the single tensor FA values in the single-fiber voxels (blue dots). In contrast, anisotropy values after DTTA correction at the CFR (red circle) overlap with FA values at the single-fiber voxels (blue dots). It indicates that the application of DTTA well restores the FA at the CFR, resulting in a group of consistent FA values at both CFR voxels and single-fiber voxels in the same tract.

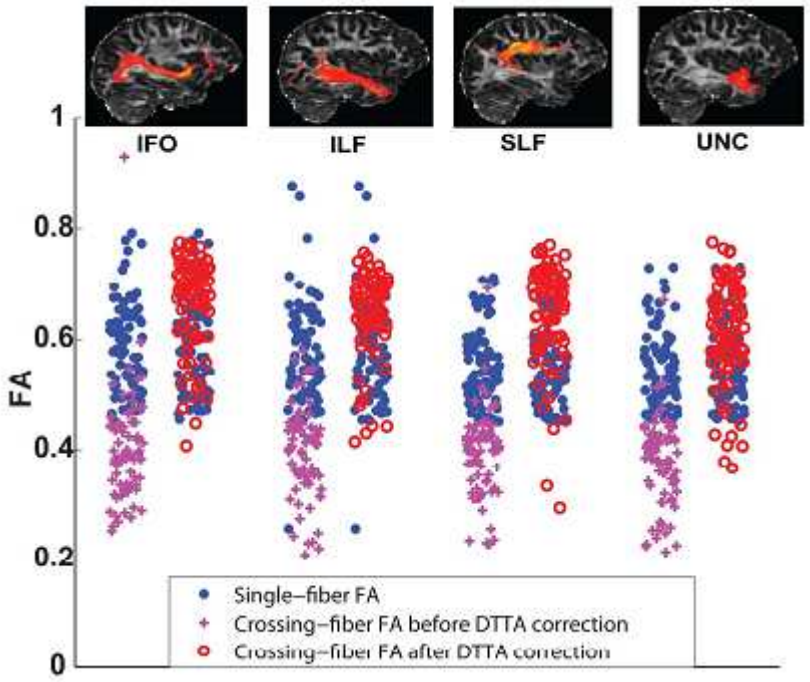

Figure 2.6: Upper panels show traced IFO, ILF, SLF and UNC overlaid on a representative sagittal ST FA image, respectively. Below each tract, crossing-fiber anisotropy values before (pink "+") and after (red circles) DTTA corrections for sampled voxels at the CFR are shown in left and right columns, respectively. The identical blue dots representing unbiased single-fiber FA values from the same tracts were put in both columns as references.

2.3.4.2. Along-the-tract Analysis

Comparisons among DTTA anisotropies, ST FA, GFA and GA along the CST from data of 17 subjects acquired from Philips scanner are shown in Figure 2.7. The traced CST is shown in red color at the top of Figure 2.7. At corona radiate part of CST, fiber crossings of CST and corpus callosum take place. The ST FA values at that location are smaller, shown as a dip in the CST profile (blue line) and pointed by the orange arrow in Figure 2.7a and Figure 2.7b. DTTA anisotropies (red line in Figure 2.7a and red bar in Figure 2.7c), GFA (gray line in Figure 2.7a and gray bar in Figure 2.7c) and GA (black line in Figure 2.7a and black bar in Figure 2.7c) show more homogeneous CST profile,

compared to ST FA (blue line in Figure 2.7a and blue bar in Figure 2.7c). Among all metrics, DTTA performs best in terms of tract profile homogeneity with smallest standard deviation to mean ratio (Figure 2.7c) based on all anisotropy values along the CST. Also shown in Figure 2.7c, the mean of GA along the CST is quite similar to that of DTTA along the CST, while the standard deviation of GFA along the CST is similar to that of DTTA anisotropy along the CST.

DTTA anisotropy profile (orange color) and ST FA profile (light blue color) obtained along the CST from 10 healthy subjects scanned on GE scanner is also shown in Figure 2.7a. Orange bar and light blue bar in Figure 2.7c shows the mean and standard deviation along CST for DTTA anisotropy and ST FA from the subjects scanned on GE scanner. As seen in Figure 2.7a, both ST FA profile and the DTTA anisotropy profile obtained from Philips scanner with 30 diffusion encoding gradient directions is similar to the DTTA anisotropy profile obtained from GE scanner with 25 diffusion encoding gradient directions. The means and standard deviations of ST FA and anisotropy obtained from DTTA along the CST across the scanners are also similar as shown in Figure 2.7c.

In addition, the DTTA anisotropy profile and ST FA profile with single shell (b=1000s/mm^2) and multi-shell (b=1000 and 2500 s/mm^2) dMRI are shown in Figure 2.7b. Their means and standard deviations are shown in Figure 2.7d. The DTTA anisotropy profiles along the CST with single shell and multi-shell dMRI appear similar in Figure 2.7b while the ST FA profile along the CST is significantly lower with multi-shell dMRI compared to that of single shell dMRI (Figure 2.7b and Figure 2.7d).

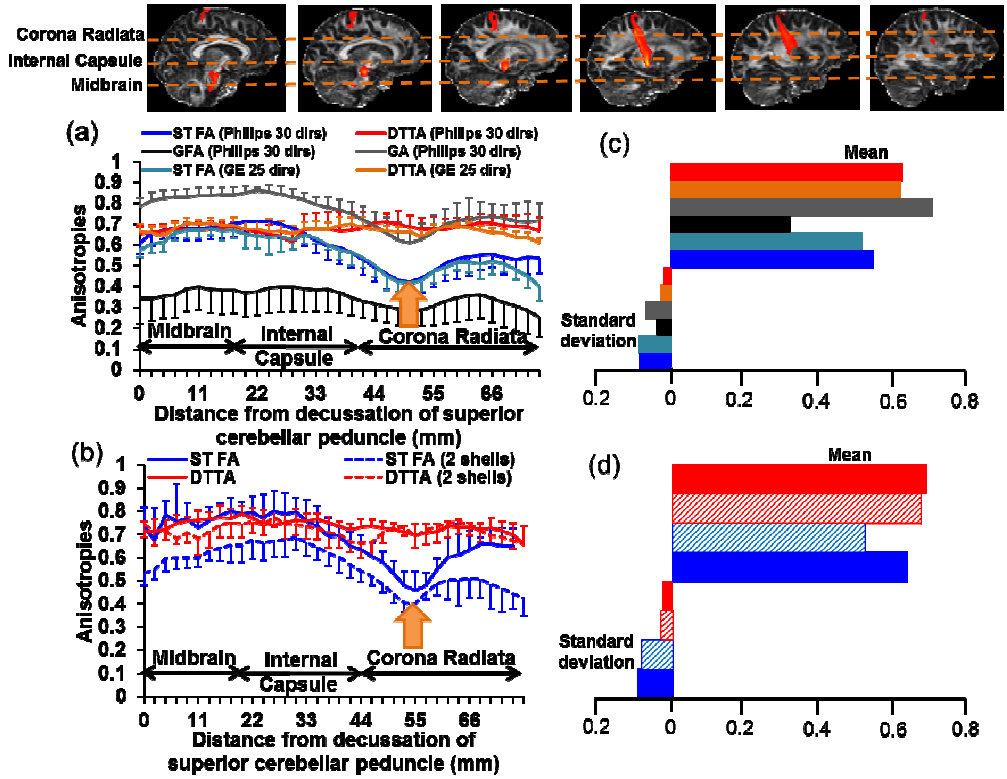

Figure 2.7: Metric profiles from DTTA, ST FA, GFA and GA along the CST. (a): Metric profiles from DTTA and ST FA from single shell dMRI from both the scanners and multi-shell dMRI (b): Mean and standard deviation of the anisotropy metrics along the CST in (c) and (d) correspond to panels (a) and (b), respectively. CST separated into segments of midbrain, internal capsule and corona radiate and overlaid on sagittal FA images is shown at the top panels for anatomical guidance.

2.4. Discussion

In this study, we presented a DTTA technique which can effectively correct the underestimated FA values at the CFR that is not contaminated by free water contribution and conduct unbiased metric measurements for tract analysis with dMRI acquired in clinical research. DTTA has low requirement on dMRI data acquisition, specifically relatively low b value and small number of diffusion orientations, and demands relatively short computation time. The motivation of this study is to help improve measurement accuracy for radiologists, psychiatrists, neurologists and other clinicians who have

become major users of dMRI in their routine clinical research. For them, there is a strong need to improve anisotropy measurements for tract analysis without altering their dMRI sequences. Our study intends to show feasibility of increasing accuracy of measuring anisotropy by adopting Gaussian mixture model and fusing this model into tract analysis. Gaussian mixture model is not one of the most recent dMRI models, but is the one that has low requirement of b value and numbers of diffusion orientations. It is noteworthy that there are other state-of-the-art dMRI models to differentiate intracellular and extracellular dMRI signals such as the composite hindered and restricted water diffusion (CHARMED) model (Assaf and Basser, 2005; Assaf et al., 2004) and neurite orientation dispersion and density imaging of the human brain (NODDI) (Zhang et al., 2012) which are beyond the scope of this study. Different from previous evaluation investigation (Ramirez-Manzanares et al., 2011) conducted with low b value; the goal of this study is not to evaluate performance of more sophisticated method such as Q-ball imaging (Tuch, 2004) in a clinical dMRI setting. The goal of the study is to test the improvement of accuracy of anisotropy measurement with DTTA. The digital phantom study and tests with clinical dMRI jointly suggest that the DTTA technique is robust for estimating unbiased anisotropy values at the CFR and can potentially increase sensitivity and accuracy in detecting WM microstructural abnormality when applied to clinical research. The digital phantom study indicated relatively high accuracy of multi-tensor fitting in a wide range of SNR and combinations of individual tensor FA values, fractions of each tensor and angles between the two tensors (Figure 2.2). The consistency of the anisotropy at the CFR after DTTA correction to the FA value at the single-fiber regions shown in Figure 2.6 and Figure 2.7 and more homogeneous weighted FA map shown in Figure 2.5 demonstrate the effectiveness of DTTA.

DTTA is unique in that it estimates two anisotropy values corresponding to crossed dual-fibers at the voxels of the CFR. Multi-FA values within a single voxel are difficult for voxelwise analysis. However, multi-FA values enable the tract analysis, as illustrated in Figure 2.1. It is important to note that the binary volumes of the crossing tracts will overlap with each other at the voxels of the CFR, if they are compressed into one volume. Two tracts need to be detached at the voxels of the CFR. With tract analysis, each of the multi-FA values at the voxels of the CFR all over the entire brain is associated with a specific detached tract (Figure 2.1). Fiber orientations of the surrounding voxels will be used to determine which tract is associated with one of the two DTTA anisotropy values. To the best of our knowledge, our method is one of the first developed methods to estimate dual-FA values at the voxel of the CFR for tract analysis. DTTA is capable of yielding less biased microstructural information and integrated into the tract statistics (Colby et al., 2012; Goodlett et al., 2009; Yushkevich et al., 2008; Zhu et al., 2011), tract morphometry (O'Donnell et al., 2009; Zhang et al., 2010) and tract metric analysis (Delgado-Ayala et al., 2012; Huang et al., 2012a; Huang et al., 2011; Huang et al., 2012b) developed recently. It should be noted that the novel weighted FA map shown in Figure 2.5 helps to conduct the whole brain voxelwise comparison of unbiased WM microstructural integrity as two anisotropy values can be integrated into one for each CFR voxel.

The most prominent feature of DTTA probably is that it can be practically applied to analyze the dMRI dataset acquired in routine clinical research. DTTA is easy to implement and postprocessing of DTTA is computationally efficient. The whole DTTA package will be made available in a public website. Most clinical dMRI takes less than 5 minutes. And typical parameters are: b value = 1000s/mm^2, angular gradient resolution = 25 to 60. The number of gradient directions to fully characterize the crossing fibers can

be estimated from SH, N=1/2*(l_{max}+1)(l_{max}+2), where l_{max} is the maximum SH order. For crossing of two fibers or two tensors, the l_{max} is 4 which results in N=15. Practically more than 15 gradient directions are needed to improve the conditioning of the two tensor fitting. It was shown in Figure 2.7c that the estimation of FA along the tract is similar across the scanners and yielded similar profile (Figure 2.7a) along the CST for acquisition with 30 or 25 diffusion encoding gradient directions. If f_{iso} is a variable in LM fitting, multi-shell dMRI is required (Caan et al., 2010). By calculating f_{iso} *a priori* before LM fitting, we have simplified the three-compartment Gaussian mixture model in equation [1] into the two-compartment model without sacrificing validity of the three-compartment model used in DTTA. Furthermore, a recent study (Hahn et al., 2013) has shown that two tensors can be reliably fit with two-compartment model and single shell dMRI. Calculating f_{iso} *a priori* has been achieved by using relationship between f_{iso} and mADC to estimate f_{iso} from mADC with routine clinic dMRI acquired with a single b value. To construct this relationship between f_{iso} and mADC, f_{iso} was estimated by nonlinear fitting from two-shell dMRI data. The relationship between f_{iso} and mADC is statistically significant for voxels in whole brain WM (Figure 2.3). In this way, f_{iso} can still reflect the varying diffusion properties of the local tissues.

As local minimum could occur in multi-variable LM regression, extra step was conducted to avoid the local minimum. With no gold standard, it is difficult to validate the estimated anisotropy at the CFR after DTTA correction. The validation was conducted with the assumption of homogeneous microstructural properties within the tract. For example, homogeneity of the T2 values, but not single tensor FA values, within the tract has been observed previously (Wakana et al., 2007).

2.5. Limitations of this Study and Future Directions

There are several limitations of DTTA technique. Firstly it should be noted that at the resolution at which the data is acquired, estimated FA is only a macroscopic view of the microscopic diffusion occurring at the cellular level which the current dMRI techniques cannot resolve. With complexity of the human brain WM, the Gaussian mixture model used in DTTA was improved compared to the single tensor model, yet it is still a rather rough and simplified characterization of the underlying WM fiber architecture. Several of the DTTA limitations are hence associated with this relatively simplified Gaussian mixture model (Equation 1) used in DTTA. First, DTTA was not designed to resolve crossing of three or more fiber bundles, although previous studies (Alexander, 2005; Behrens et al., 2007) suggest that crossings of two fiber bundles happen most among all fiber crossings in brain voxels. The phantom study showed that DTTA failed to accurately estimate anisotropies of the two crossed fiber bundles when the separation angle between them is less than 30 degrees. In addition, the fiber bundles that are diverging, kissing, bending or fanning could not be resolved with DTTA either. In order to reduce number of independent variables for better LM regression, assumptions such as equal largest eigenvalues for the two tensors may not best fit the underlying WM fiber architecture. The assumptions on the equal largest eigenvalues has been used before (Caan et al., 2010; Sotiropoulos et al., 2008) and prevented the DTTA technique from being used for estimating other important metrics such as axial or radial diffusvities at the CFR (Wheeler-Kingshott and Cercignani, 2009). In addition, assuming fixed coefficients in the constructed relationship of f_{iso} and *mADC*, i.e. f_{iso} =c1**mADC*+c2, could lead to at most an approximated estimate of f_{iso}. Nevertheless, it is a more appropriate estimation of f_{iso} that reflects local tissue diffusion properties compared to the fixed value used previously (Hosey et al., 2005). Figure 2.3 shows that f_{iso} of most WM voxels clusters between 0.1

and 0.3. With the advent of advanced imaging technique, dMRI with high angular resolution and high b can be acquired with shorter scan time and eventually applied to the clinical research in the future. Accordingly, DTTA will evolve by incorporating multi-shell dMRI acquisition and more sophisticated signal mixture model by removing the limitations such as equal largest eigenvalues.

2.6. Conclusion

In conclusion, a DTTA technique tailored for the dMRI data acquired in routine clinical research and adapted to tract analysis has been presented and tested to be effective for improving accuracy of the anisotropy in tract analysis. Digital phantom analysis indicated high accuracy of estimating the multiple anisotropy values at the CFR. The underestimated FA at the CFR of the four major associate WM tracts was effectively corrected and consistent to the single-fiber FA of the same tracts. DTTA renders equally well or more homogeneous anisotropy profile along the tract of CST, compared to GFA or GA.

Chapter 3

Differences of Inter-Tract Correlations between Neonates and Children around Puberty: A study based on Microstructural Measurements with DTI

3.1 Introduction

The human brain is complicated yet well organized. The major cerebral white matter (WM) tracts connecting different brain regions are involved in different brain functions. These major cerebral WM tracts are often categorized into different tract groups based on their distinct functions. There are roughly four tract groups, namely limbic, projection, callosal and association tract groups (Huang et al., 2012a; Huang et al., 2012b; Wakana et al., 2004) for cerebral WM tracts. The WM tracts within a tract group perform similar functions. For example, limbic tracts underlie the connectivity in the limbic system and association tracts connect between cerebral cortical areas. The pair of tracts in both cerebral hemispheres belongs to the same tract group and is considered as homologous tracts. At birth, most of major WM tracts are well formed (Huang et al., 2006; Oishi et al., 2011), except the arcuate fasciculus which is a part of the superior longitudinal fasciculus (SLF) and related to language function.

The water molecules all over the human brain tend to diffuse more freely along the WM fiber bundle, instead of perpendicular to it. This diffusion property can be measured noninvasively with diffusion MRI (dMRI), a modality of MRI. The widely used diffusion tensor imaging (DTI) (Basser et al., 1994a, b) characterizes the water diffusion properties in the brain voxels with a tensor model. Fractional anisotropy (FA) (Beaulieu, 2002; Pierpaoli and Basser, 1996) and mean diffusivity (MD), derived from DTI, have been widely used to quantify the microstructural properties of the WM voxels. Other than FA or MD, the other two DTI-derived metrics, radial diffusivity (RD) and axial diffusivity (AxD), convey unique information related to myelination and axonal integrity, respectively

(Song et al., 2002). The four DTI-derived metrics, FA, RD, AxD and MD, characterize different aspects of diffusion tensor and are highly sensitive to WM microstructural changes.

Compared to voxel-based morphometry (VBM), recent tract analyses (Colby et al., 2012; Goodlett et al., 2009; O'Donnell et al., 2009; Yushkevich et al., 2008; Zhang et al., 2010) including ours (Delgado-Ayala et al., 2012; Huang et al., 2012a; Huang et al., 2011; Huang et al., 2012b) have become important due to great functional and clinical significance of the tracts. These WM tracts can be noninvasively traced with tractography based on diffusion MRI (dMRI) (Basser et al., 2000; Behrens et al., 2007; Catani et al., 2002; Conturo et al., 1999; Jones et al., 1999b; Lazar et al., 2003; Mori et al., 1999; Parker et al., 2002; Stieltjes et al., 2001) and the heterogeneous WM tracts can be noninvasively segmented with the traced fibers. With these segmented WM tracts as binary masks for the maps of DTI-derived metrics, the microstructural properties of the WM tracts can be quantified.

Dramatic microstructural changes take place during normal human brain development from birth to puberty, which are two landmark time points in early brain development. Birth marks the beginning time point of postnatal brain development. Puberty marks the end of the child development and beginning of adolescence. The four DTI derived metrics, FA, RD, AxD and MD, have been incorporated in numerous studies investigating WM microstructural changes for infants, children and adolescents during development. The human brain development process is usually characterized with significant increases in FA (Barnea-Goraly et al., 2005; Dubois et al., 2008; Eluvathingal et al., 2007; Gao et al., 2009a; Giorgio et al., 2010; Lebel et al., 2008; Schmithorst and Yuan, 2010; Snook et al., 2005; Tamnes et al., 2010; Westlye et al., 2010) and significant decreases in MD, AxD and RD (Dubois et al., 2008; Eluvathingal et al., 2007; Gao et al.,

2009a; Giorgio et al., 2010; Lebel et al., 2008; Schmithorst and Yuan, 2010; Snook et al., 2005; Tamnes et al., 2010; Westlye et al., 2010). On the other hand, it was shown with DTI-derived metrics of a cohort of adults that specific WM tracts involved in similar functions vary in a similar pattern with each other across different individuals (Li et al., 2012; Wahl et al., 2010), while hemispheric asymmetries of DTI-derived metrics in homologous pairs of WM tracts (Bonekamp et al., 2007; Wilde et al., 2009) have been reported. However, from perspective of brain development, whether or not the significant inter-tract correlations exist at birth and around puberty is still unclear. Furthermore, it remains elusive if these inter-tract correlations will be strengthened and how the correlation patterns change from birth to puberty.

During the development from birth to puberty, the human brain is likely to change from a more randomized state to a more balanced and organized state. In this study, we hypothesized that inter-tract correlations become stronger and the correlation patterns are reshuffled from birth to puberty. Specifically, the reshuffling process will cause more homologous tracts to form tight relationship. DTI data were acquired from 26 normal neonates and 28 normal children around puberty. The following 10 major WM tracts covering limbic, association, commissural and projection tract groups were selected for tract-level measurements of DTI metrics of each subject: left and right corticospinal tract (CST_L and CST_R), left and right inferior fronto-occipital fasciculus (IFO_L and IFO_R), left and right cingulate part of cingulum tract (CGC_L and CGC_R), left and right hippocampal part of cingulum tract (CGH_L and CGH_R), forceps major (FMajor) and forceps minor (FMinor). The tract level comparisons of all four DTI-derived metrics were conducted between the two age groups. Spearman's pairwise inter-tract correlations were performed. We tested if significant correlations of homologous WM tracts exist in neonates and children around puberty. After obtaining four 10 by 10 inter-tract correlation

matrices corresponding to four DTI-derived metrics, FA, RD, AxD and MD, for each age group, we tested these correlation matrices against the identity matrix or a matrix with equal non-diagonal entries. We then assessed if the inter-tract correlations become statistically stronger from birth to puberty. In addition, hierarchical clustering was performed with the pairwise correlations based on FA, RD, AxD and MD measurements for each age group to reveal the pattern of clustering in either age group and reveal the pattern shift from birth to puberty.

3.2. Materials and Methods

3.2.1. Subjects and Data Acquisition

26 normal neonates (14 males; age: 37 to 43 gestational weeks with mean and standard deviation 40.1±2.0 gestational weeks) and 28 normal children around puberty (15 males; age: 9.5 to 15 years with mean and standard deviation 12.0±2.3 years), free of current and past neurological or psychiatric disorders, were recruited at Children's Medical Center (CMC) at Dallas and Advanced Imaging Research Center (AIRC) of the University of Texas Southwestern Medical Center (UTSW), respectively. The parents of all the subjects gave written informed consents approved by Institutional Review Board of UTSW.

Two 3T Philips Achieva MR systems at CMC and AIRC were used to acquire dMRI of neonate and child group, respectively. dMRI data were acquired using a single shot echo planar imaging (EPI) with SENSE parallel imaging scheme (SENsitivity Encoding, reduction factor = 2.3). dMRI parameters for neonates were: FOV = 200/200/100 mm, in-plane imaging matrix = 100 x 100, axial slice thickness = 2mm. dMRI parameters for children around puberty were: FOV = 224/224/143 mm, in-plane imaging matrix = 112 x 112, axial slice thickness = 2.2mm. The common parameters for dMRI

acquisition of both neonate and child group were: b-value = 1000 s/mm^2, TE = 97ms, TR = 7.6s, 30 independent diffusion-weighted directions (Jones et al., 1999) and 2 repetitions to increase signal-to-noise ratio (SNR).

3.2.2. DTI Preprocessing

dMRI acquired from all the subjects was processed offline using DTIStudio mristudio.org; (Jiang et al., 2006). dMRI images for each subject were corrected for motion and eddy current by registering all the diffusion weighted images to the b0 image using a 12-parameter (affine) linear image registration with automated image registration (AIR) algorithm (Woods et al., 1998). After the registration, six independent elements of the 3×3 diffusion tensor (Basser et al., 1994a, b) were determined by multivariate least-square fitting of diffusion weighted images. The tensor was diagonalized to obtain three eigenvalues (λ_{1-3}) and eigenvectors (ν_{1-3}). FA, MD, AxD and RD, derived from DTI, were obtained for all the subjects with the following equations of eigenvalues:

$$FA = \frac{\sqrt{(\lambda_1 - \lambda_2)^2 + (\lambda_1 - \lambda_3)^2 + (\lambda_2 - \lambda_3)^2}}{\sqrt{2}\sqrt{\lambda_1^2 + \lambda_2^2 + \lambda_3^2}}$$

$$MD = (\lambda_1 + \lambda_2 + \lambda_3)/3$$

$$AxD = \lambda_1$$

$$RD = (\lambda_2 + \lambda_3)/2 \qquad [3.1]$$

3.2.3. Tract-level Measurements of DTI Metrics

The following 10 major white matter tracts were selected for tract-level measurements of DTI metrics, left and right corticospinal tract (CST_L and CST_R), left

and right inferior fronto-occipital fasciculus (IFO_L and IFO_R), left and right cingulate part of cingulum tract (CGC_L and CGC_R), left and right hippocampal part of cingulum tract (CGH_L and CGH_R), forceps major (FMajor) and forceps minor (FMinor). These tracts could be reproducibly traced with DTI of all neonates and children and cover all four major tract groups, namely projection, limbic, commissural and association tract group. Other major white matter tracts such as SLF could not be traced reproducibly with our cohort of neonate DTI dataset. Following the literature (Wakana et al., 2007), the tractography protocol described in details below was used to trace all these tracts. DTIstudio (mristudio.org) was used to conduct the tractography. The binary masks of the individually traced tracts were used to compute the tract-level FA, RD, AxD and MD. The test-retest reliability was quantified by coefficient of variation (CV) and κ values of variability shown in Table 3.1, after tracing the tracts below 3 times with the data from 3 subjects randomly selected from each group. All CV values are less than 2% (Table 3.1a) and κ values are greater than 95% (Table 3.1b) for both neonate an child group, indicating almost perfect test-retest reliability and almost perfect agreement of measurements among different tests in both neonate and child group.

Table 3.1: (a) Mean coefficients of variation (% CV) of FA, RD, AxD and MD measurements for neonates and children around puberty. 3 subjects in each group were randomly selected to compute CV. Each tract was traced 3 times for data from each subject. (b) Mean Kappa (κ) for neonates and children around puberty. 3 subjects in each group were randomly selected to compute κ. Each tract was traced 3 times for data from each subject.

(a)

	FA		**RD**		**AxD**		**MD**	
	Neonates	***Children around puberty***	***Neonates***	***Children around puberty***	***Neonates***	***Children around puberty***	***Neonates***	***Children around puberty***
CST_L (%)	0.2	0.2	0.1	0.1	0.06	0.2	0.05	0.05
CST_R (%)	0.2	0.1	0.1	0.2	0.1	0.1	0.1	0.1
CGH_L (%)	0	0.1	0	0.03	0	0.06	0	0.03
CGH_R (%)	0.02	0.1	0.001	0.02	0.02	0.08	0.008	0.05
CGC_L (%)	0	0.07	0	0.05	0	0.05	0	0.03
CGC_R (%)	0	0.06	0	0.1	0	0.06	0	0.08
IFO_L (%)	0.01	0.03	0.002	0.03	0.001	0.03	0.001	0.01
IFO_R (%)	0	0.07	0	0.06	0	0.04	0	0.04
FMinor (%)	0.2	0.05	0.2	0.02	0.2	0.04	0.2	0.01
FMajor (%)	0.3	0.03	0.03	0.01	0.1	0.02	0.05	0.01
Average (%)	0.09	0.08	0.04	0.06	0.05	0.07	0.04	0.04

Table 3.1 -- *Continued*

(b)

	Mean Kappa (κ)	
	Neonates	***Children around puberty***
CST_L	0.986	0.962
CST_R	0.97	0.979
CGH_L	0.99	0.987
CGH_R	0.989	0.987
CGC_L	0.99	0.984
CGC_R	0.989	0.979
IFO_L	0.995	0.986
IFO_R	0.996	0.982
FMinor	0.956	0.997
FMajor	0.975	0.998
Average	0.984	0.984

CST-L and CST-R: For the first ROI, the entire cerebral peduncle of the desired hemisphere was delineated at the level of the decussation of the superior cerebellar peduncle using an axial slice. “OR” operation was used to select all the CST fibers in this hemisphere that reach the primary motor cortex. The second ROI was then drawn at the most ventral axial slice that identifies the cleavage of the central sulcus. “AND” operation is performed at this axial slice to select all the CST fibers in this hemisphere. The fibers running through to the opposite hemisphere were removed using the “NOT” operation.

CGC-L and CGC-R: For the first ROI, a coronal plane was selected at the middle of the splenium of the corpus callosum (CC) using the mid-sagittal plane and the region containing the entire cingulum in the desired hemisphere is selected. All the fibers in this coronal plane passing through the cingulum were selected using the “OR” operation. The second ROI was drawn by selecting a coronal plane in the middle of the genu of the CC and all the CGC fibers were selected using the “AND” operation.

CGH-L and CGH-R: For the first ROI, a coronal plane in the middle of the splenium of the CC was selected using the mid-sagittal plane and the cingulum below the CC of the desired hemisphere was delineated. All the fibers in this coronal plane passing through the cingulum were selected using the “OR” operation. The second ROI was drawn at a coronal slice anterior to the pons using the mid-sagittal plane and the fibers passing through the cingulum in this hemisphere were selected using the “AND” operation.

IFO-L and IFO-R: For the first ROI, a coronal slice at the middle point between the posterior edge of the cingulum and the posterior edge of the parieto-occipital sulcus was selected and the entire occipital lobe of the desired hemisphere was delineated. All the fibers in this hemisphere were selected using the “OR” operation. The second ROI was drawn at the anterior edge of the CC using a coronal slice and all the fibers in this

hemisphere were selected using the “AND” operation. The fibers running through to the thalamus were removed by using the “NOT” operation.

FMajor: For the first ROI, a coronal plane including only the left occipital lobe was selected at the most posterior edge of the parieto-occipital sulcus. The “OR” operation in this coronal plane delineated all the fibers of FMajor. The second ROI was drawn in the same coronal plane on the right hemisphere using the “AND” operation such that all the fibers in the right occipital lobe was selected.

FMinor: For the first ROI, a coronal plane at the middle point between the anterior tip of the frontal lobe and the anterior edge of the genu of the CC was selected using the mid-sagittal plane. The “OR” operation was used to select all the fibers in the entire left hemisphere. The second ROI was drawn in the same coronal plane on the right hemisphere and all the fibers in the right hemisphere were selected using the “AND” operation.

3.2.4. Inter-tract Correlation Analysis

Shapiro-Wilk normality test was performed with DTI-derived metrics of all the 10 white matter tracts of 26 neonate brains and 28 child brains. Distributions of DTI-derived metrics for most of the tracts in the neonate group did not show significant difference ($p>0.05$) from normality. However, distributions of DTI-derived metrics of most of the tracts in the child group differed significantly ($p<0.05$) from normality. Hence, following the method in the literature (Wahl et al., 2010), non-parametric Spearman’s rank correlation coefficient ρ was used to measure all correlations. Subsequently, a correlation matrix was constructed for each of the 4 DTI-derived metrics using pairwise correlation values between any two tracts. Symmetric correlation matrices were obtained with a value of unity along the diagonal of the correlation matrix. The diagonal element

represents perfect correlation of the DTI-derived parameter of the tract with itself and the off-diagonal element represents the correlation of the DTI derived parameter of one tract with that of another tract. There were 10*(10-1)/2 = 45 nontrivial independent correlation values in each correlation matrix.

3.2.5. Statistical Analysis

Two independent tests of correlation matrices were performed to evaluate if the correlation matrices were significantly different from identity and homogeneous matrix (Rencher, 2002; Wahl et al., 2010). The null hypothesis to test for identity was the correlation matrix is an identity matrix, $\Pi_0 = \begin{pmatrix} 1 & 0 & 0 \\ \vdots & \ddots & \vdots \\ 0 & \cdots & 1 \end{pmatrix}$. The size of the correlation matrix was 10 x 10 as we were testing for pairwise correlations of 10 independent tracts. To test the correlation matrices for homogeneity, the null hypothesis was that the correlation matrix was homogeneous and that the non-diagonal elements of the matrix were equal, i.e: $\mu_0 = \begin{pmatrix} 1 & \rho & \rho \\ \vdots & \ddots & \vdots \\ \rho & \cdots & 1 \end{pmatrix}$. This null hypothesized homogeneous correlation matrix was derived by following the procedure outlined in the literature (Rencher, 2002; Wahl et al., 2010). Bonferroni correction was conducted for both test of correlation matrix against identify matrix and test of correlation matrix against matrix with equal non-diagonal elements. Once the DTI-derived correlation matrices were found to be significantly different from identity and homogeneity within each group, correlation matrices of each DTI-derived metric were compared between the two age groups. Spearman's rank correlation coefficients were converted to z values by using Fisher's r-to-z-transform (Fisher, 1915). Note that *r* in Fisher's r-to-z-transform is the spearman's rank correlation

coefficient ρ in this study. Z-statistics was then performed to identify the pair of tracts that showed significant change in correlation strength from birth to puberty.

3.2.6. Hierarchical Clustering Analysis

Hierarchical clustering methods were used to characterize the patterns of inter-tract correlation in each matrix among the groups. We used 1-ρ, where ρ is the Spearman's rank correlation coefficient, as a measure of distance or dissimilarity between the white matter tracts for the purpose of clustering. Hierarchical clustering was performed using hclust function in R version 2.15.2. Depending on the correlation coefficient, different white matter tracts were successively grouped into larger groups and the results were visualized as a dendrogram. White matter tracts that had stronger correlation among themselves were fused together and were linked together. To characterize the uncertainty of the linkage among white matter tracts and reduce the standard error in the percentage of confidence level for each cluster, a multi-scale bootstrap with 1000 repetitions of the analysis was performed using pvclust function in R (Suzuki and Shimodaira, 2006). The multi-scale bootstrap analysis yields an approximately unbiased p-value of each linkage in hierarchical clustering and has been applied in various other studies (Shimodaira, 2002, 2004; Wahl et al., 2010). The threshold for determining statistical significance for the grouping of tracts was set at an unbiased p-value of 0.05 or 95% confidence interval.

3.3. Results

3.3.1. Changes of White Matter Microstructure from Neonates to Children around Puberty

Figure 3.1 shows the three-dimensional (3D) visualization of the traced 10 major white matter tracts for a typical neonate and a typical child around puberty. These 10

major tracts, namely CST_L, CST_R, IFO_L, IFO_R, CGC_L, CGC_R, CGH_L, CGH_R, FMajor and FMinor, cover projection, limbic, association and commissural tract groups involved in distinct brain functions. The microstructural changes from neonates to children at puberty and measured with FA, MD, AxD and RD are shown in Figure 3.2. For all 10 major white matter tracts, FA values are higher in the child group than those of the neonate group while MD, AxD and RD values of the child group are less. FA of CST_L and CST_R of both age groups are highest among all tracts, followed by FMajor and FMinor. RD of CST_L and CST_R of both age groups are lowest among all tracts, indicating better myelination of CST compared to all other tracts. MD and AxD of FMajor and FMinor are highest among all tracts for child group. The values of these DTI-derived metrics of all tracts for the two age groups are shown in Table 3.2.

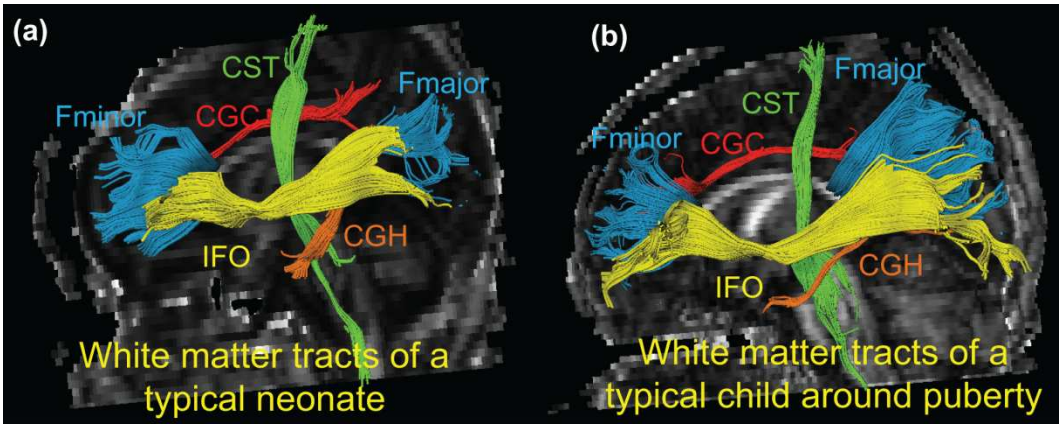

Figure 3.1: 3-D visualization of the traced WM tracts overlaid on mid-sagittal slice of the FA image of a typical neonate (a) and a typical child around puberty (b). Different colors represent different tracts traced for both subjects. CGC_L/R, CGH_L/R, CST_L/R, FMajor/FMinor and IFO_L/R are painted by red, orange, green, blue and yellow color, respectively.

Table 3.2: Mean tract-level FA, RD, AxD and MD measurements and their standard deviations for neonates and children around puberty.

	FA		**RD ($10^{-3}mm^2/s$)**		**AxD ($10^{-3}mm^2/s$)**		**MD ($10^{-3}mm^2/s$)**	
	Neonates	***Children around puberty***	***Neonates***	***Children around puberty***	***Neonates***	***Children around puberty***	***Neonates***	***Children around puberty***
CST left	0.33±0.022	0.514±0.026	0.935±0.069	0.515±0.08	1.577±0.081	1.235±0.121	1.149±0.07	0.755±0.092
CST right	0.327±0.024	0.505±0.018	0.935±0.076	0.518±0.057	1.573±0.101	1.238±0.102	1.148±0.082	0.758±0.07
CGH left	0.234±0.02	0.37±0.032	1.087±0.079	0.631±0.077	1.562±0.099	1.142±0.117	1.245±0.084	0.802±0.088
CGH right	0.241±0.018	0.37±0.026	1.063±0.082	0.619±0.073	1.549±0.102	1.119±0.108	1.225±0.087	0.786±0.083
CGC left	0.254±0.022	0.423±0.021	1.098±0.072	0.57±0.047	1.622±0.099	1.139±0.077	1.273±0.078	0.759±0.055
CGC right	0.237±0.022	0.404±0.025	1.112±0.074	0.574±0.06	1.6±0.099	1.103±0.098	1.274±0.079	0.75±0.071
IFO left	0.258±0.022	0.454±0.025	1.141±0.082	0.567±0.05	1.686±0.092	1.209±0.069	1.322±0.084	0.781±0.054
IFO right	0.264±0.02	0.436±0.02	1.145±0.093	0.582±0.05	1.709±0.112	1.197±0.08	1.333±0.098	0.787±0.058
FMinor	0.292±0.023	0.481±0.02	1.15±0.088	0.546±0.032	1.823±0.119	1.257±0.066	1.374±0.095	0.783±0.04
FMajor	0.31±0.019	0.483±0.024	1.121±0.105	0.548±0.055	1.825±0.162	1.297±0.098	1.355±0.122	0.798±0.066

3.3.2. Enhanced Inter-tract Correlation from Neonates to Children around Puberty

Figure 3.3 shows the scatterplot of the FA (Figure 3.3a), RD (Figure 3.3b), AxD (Figure 3.3c) and MD (Figure 3.3d) values for 2 pairs of homologous tracts and 2 pairs of non-homologous tracts, CGC_L vs CGC_R, CST_L vs CST_R, FMajor vs FMinor and CST-R vs CGC-R. The 2 homologous tracts and FMajor/FMinor represent tract pairs of the three tract groups. Significant correlations ($p<0.05$) can be observed for these 4 pairs of tracts in both age groups.

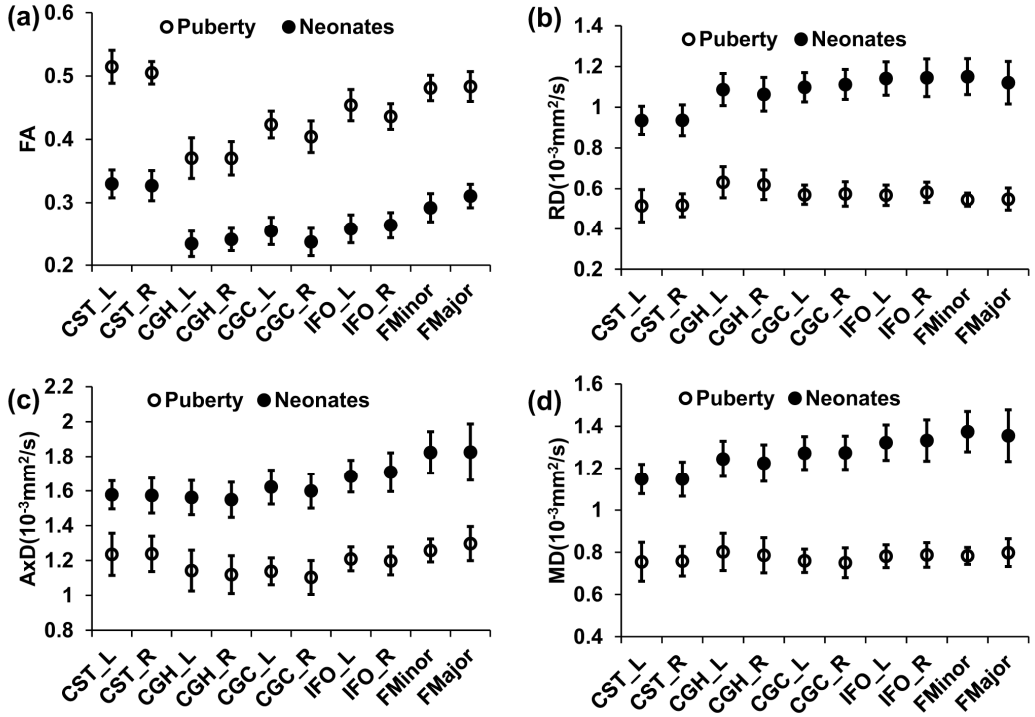

Figure 3.2: Mean and standard deviation of tract-level FA (a), RD (b), AxD (c) and MD (d) measurements for 26 neonates and 28 children around puberty for all the 10 WM tracts. Error bars indicate standard deviations across all the subjects at the same age group.

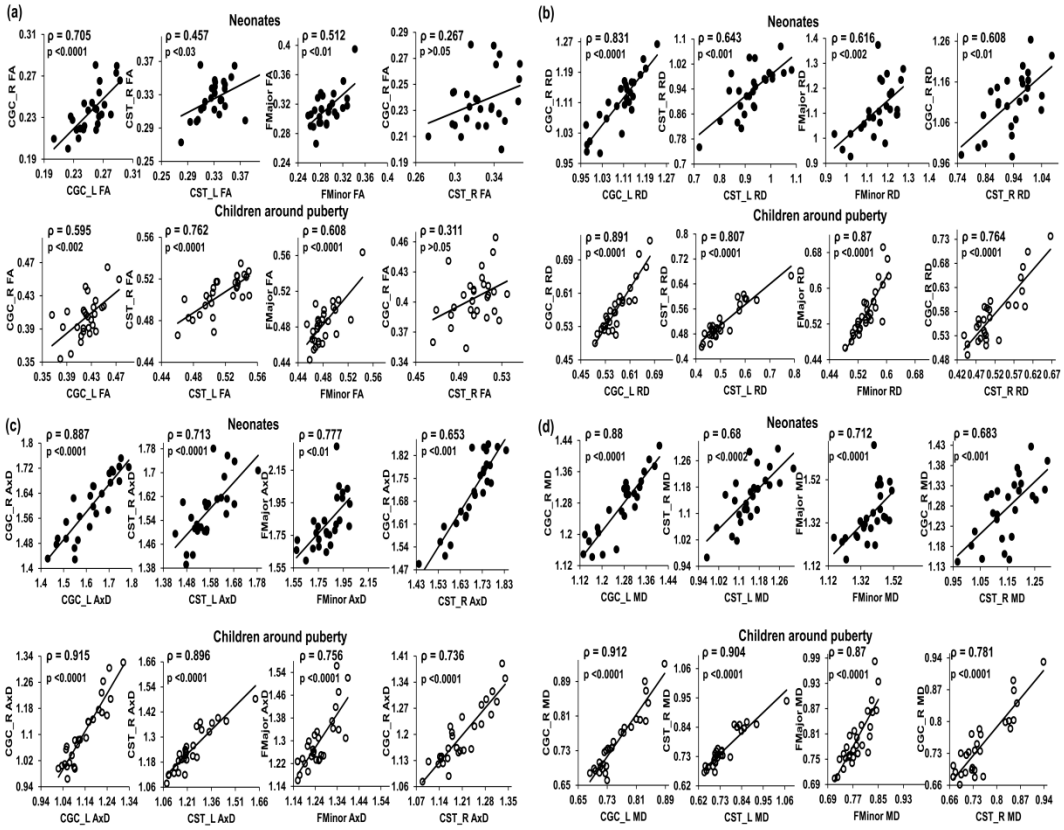

Figure 3.3: Scatterplots of FA (a), RD (b), AxD (c) and MD (d) values from 2 homologous and 2 non-homologous tracts. The 2 homologous pairs and FMajor/FMinor represent tract pairs of three tract groups for both age groups. Top panel shows the inter-tract scatter plots for the neonates and bottom panel shows those for the children around puberty. Each dot in all the plots represents the data from an individual subject in that group. ρ is the Spearman's rank correlation coefficient of the tract pair while p-value shows the statistical confidence of the inter-tract correlation strength.

Significant differences ($p < 0.05$, Bonferroni-corrected) were observed for tests of all inter-tract correlation matrices of both groups against identity matrix or matrix with equal non-diagonal entries. The inter-tract correlation matrices of neonate and child group and the differences of these correlation matrices for FA, RD, AxD and MD are shown in Figures. 3.4a, 3.4b, 3.4c and 3.4d, respectively. General stronger inter-tract correlations can be observed in the child group compared to those in the neonate group for all DTI-derived metrics, represented by the warmer colors in correlation matrices of

child group. The statistics with z-scores (right panel of Figure3. 4) show that 64.4% (29/45), 84.4% (38/45), 73.3% (33/45) and 73.3% (33/45) of independent entries in the correlation matrix of child group are significantly higher than the corresponding entries of neonate group for FA, RD, AxD and MD, respectively. The correlation matrix from RD shows highest percentage changes (84.4%) among correlation matrices from all DTI-derived metrics, indicating more widespread enhanced inter-tract correlations with RD measurements. Note that the denominator 45 above indicates the number of all independent entries in the correlation matrix. The absolute values of correlation coefficients for AxD and MD, represented by the warmer colors in Figure 3.4c and Figure 3.4d, are higher in both neonate and child group than those for FA (Figure 3.4a) or RD (Figure 3.4b). Much smaller percentages of independent entries of the correlation matrices are associated with the situation where correlation coefficients are significantly higher in the neonates than the children. Specifically, these percentages are 8.9% (4/45, namely CGC_R vs FMinor, CGC_R vs FMajor, CGH_L vs IFO_L and IFO_L vs IFO_R), 6.7% (3/45, namely CGC_R vs FMinor, CGC_R vs FMajor and IFO_L vs FMajor), 4.4% (2/45, namely CGC_R vs FMinor and CGC_R vs FMajor) and 4.4% (2/45, namely CGC_R vs IFO_R and CGC_R vs FMajor) for FA, RD, AxD and MD, respectively. The inter-tract correlation coefficient values based on FA, RD, AxD and MD measurements for both age groups are shown in Table 3.3a, Table 3.3b, Table 3.3c and Table 3.3d respectively.

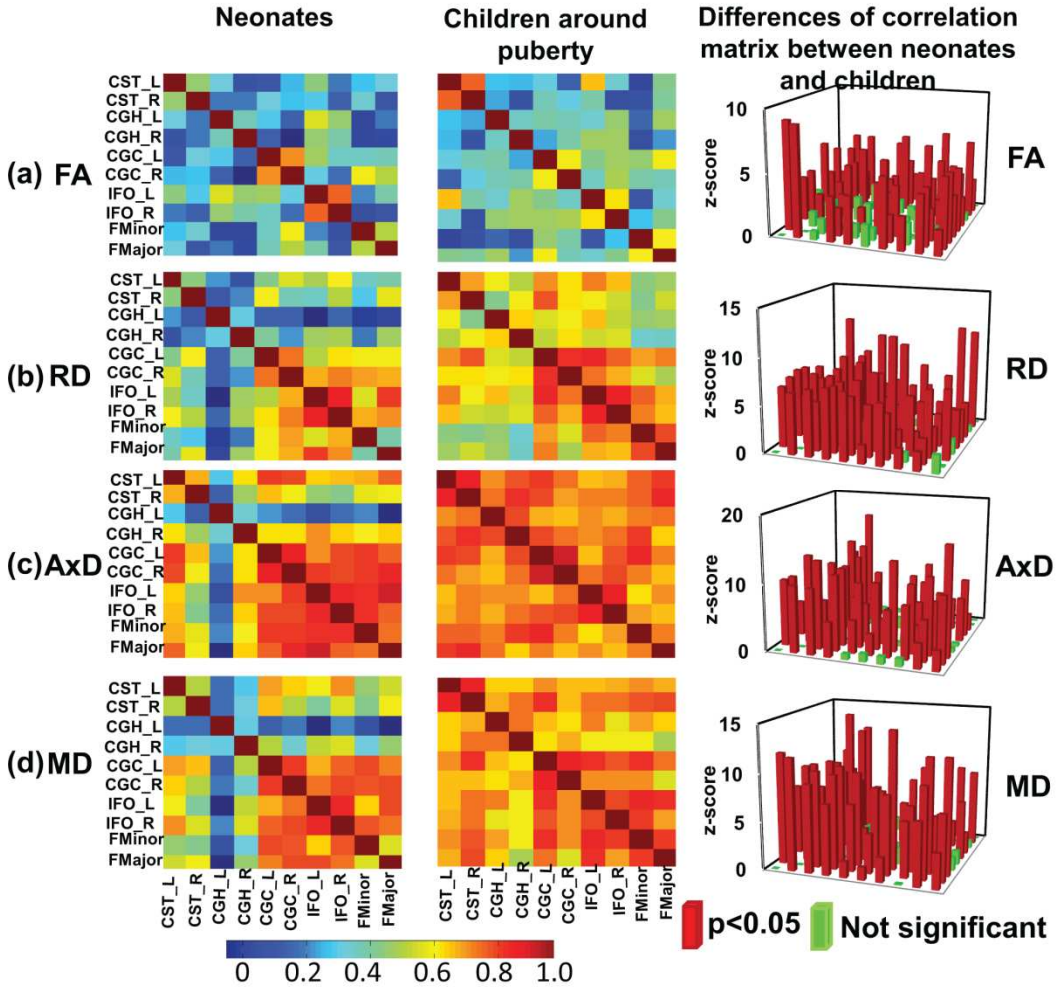

Figure 3.4: Heat maps of the inter-tract correlation matrices obtained from tract-level FA (a), RD (b), AxD (c) and MD (d) measurements of both age groups. The left and middle panels show the inter-tract correlation matrices for neonates and children around puberty, respectively. The right panel shows the z-scores of the changes in correlation strength between the two age groups. In the z-score plots, the entries with significant ($p<0.05$) changes in inter-tract correlation strengths are shown in red color while entries with non-significant ($p>0.05$) change in inter-tract correlation strengths are shown in green color. Color bar encoding the correlation strengths in the left and middle columns is also shown.

Table 3.3: (a) Spearman's inter-tract correlation coefficient (ρ) matrix based on FA measurements (b) Spearman's inter-tract correlation coefficient (ρ) matrix based on RD measurements (c) Spearman's inter-tract correlation coefficient (ρ) matrix based on AxD measurements. (d) Spearman's inter-tract correlation coefficient (ρ) matrix based on MD measurements.

(a)

Neonates										
	CST_L	**CST_R**	**CGH_L**	**CGH_R**	**CGC_L**	**CGC_R**	**IFO_L**	**IFO_R**	**FMinor**	**FMajor**
CST_L	1									
CST_R	0.457	1								
CGH_L	0.318	0.181	1							
CGH_R	0.05	0.186	0.372	1						
CGC_L	0.088	0.314	0.294	0.136	1					
CGC_R	0.252	0.267	0.144	-0.074	0.705	1				
IFO_L	0.44	0.29	0.556	0.454	0.47	0.3	1			
IFO_R	0.19	0.143	0.463	0.388	0.358	0.167	0.752	1		
FMinor	0.278	0.331	0	0	0.352	0.587	0.196	0.036	1	
FMajor	0.324	0.093	0.182	0.026	0.378	0.498	0.383	0.086	0.512	1
Children around puberty										
	CST_L	**CST_R**	**CGH_L**	**CGH_R**	**CGC_L**	**CGC_R**	**IFO_L**	**IFO_R**	**FMinor**	**FMajor**
CST_L	1									
CST_R	0.762	1								
CGH_L	0.267	0.244	1							
CGH_R	0.256	0.045	0.347	1						
CGC_L	0.301	0.363	0.390	0.241	1					
CGC_R	0.143	0.311	0.369	0.385	0.595	1				
IFO_L	0.655	0.395	0.344	0.467	0.419	0.351	1			
IFO_R	0.331	0.033	0.457	0.465	0.469	0.494	0.631	1		
FMinor	0.006	0.055	0.152	0.041	0.46	0.39	0.086	0.274	1	
FMajor	0.414	0.397	0.466	0.221	0.595	0.365	0.335	0.427	0.608	1

Table 3.3 -- *Continued*

(b)

Neonates										
	CST_L	**CST_R**	**CGH_L**	**CGH_R**	**CGC_L**	**CGC_R**	**IFO_L**	**IFO_R**	**FMinor**	**FMajor**
CST_L	1									
CST_R	0.643	1								
CGH_L	0.508	0.432	1							
CGH_R	0.406	0.495	0.558	1						
CGC_L	0.631	0.748	0.454	0.628	1					
CGC_R	0.724	0.608	0.452	0.508	0.831	1				
IFO_L	0.682	0.595	0.323	0.668	0.690	0.796	1			
IFO_R	0.748	0.693	0.469	0.680	0.764	0.824	0.909	1		
FMinor	0.595	0.551	0.357	0.486	0.738	0.802	0.716	0.79	1	
FMajor	0.619	0.726	0.368	0.666	0.744	0.795	0.878	0.818	0.616	1
Children around puberty										
	CST_L	**CST_R**	**CGH_L**	**CGH_R**	**CGC_L**	**CGC_R**	**IFO_L**	**IFO_R**	**FMinor**	**FMajor**
CST_L	1									
CST_R	0.807	1								
CGH_L	0.743	0.639	1							
CGH_R	0.692	0.737	0.771	1						
CGC_L	0.815	0.861	0.72	0.694	1					
CGC_R	0.76	0.764	0.745	0.762	0.891	1				
IFO_L	0.828	0.738	0.78	0.712	0.894	0.837	1			
IFO_R	0.784	0.707	0.697	0.723	0.846	0.799	0.906	1		
FMinor	0.65	0.639	0.654	0.584	0.806	0.719	0.851	0.826	1	
FMajor	0.669	0.712	0.668	0.588	0.823	0.678	0.795	0.787	0.87	1

Table 3.3 -- *Continued*

(c)

Neonates										
	CST_L	**CST_R**	**CGH_L**	**CGH_R**	**CGC_L**	**CGC_R**	**IFO_L**	**IFO_R**	**FMinor**	**FMajor**
CST_L	1									
CST_R	0.713	1								
CGH_L	0.38	0.259	1							
CGH_R	0.68	0.541	0.43	1						
CGC_L	0.835	0.711	0.33	0.673	1					
CGC_R	0.825	0.653	0.287	0.681	0.887	1				
IFO_L	0.691	0.535	0.166	0.752	0.748	0.832	1			
IFO_R	0.708	0.503	0.282	0.691	0.813	0.813	0.860	1		
FMinor	0.712	0.639	0.32	0.656	0.828	0.828	0.848	0.854	1	
FMajor	0.786	0.646	0.077	0.686	0.798	0.868	0.915	0.792	0.777	1
Children around puberty										
	CST_L	**CST_R**	**CGH_L**	**CGH_R**	**CGC_L**	**CGC_R**	**IFO_L**	**IFO_R**	**FMinor**	**FMajor**
CST_L	1									
CST_R	0.896	1								
CGH_L	0.748	0.779	1							
CGH_R	0.802	0.85	0.814	1						
CGC_L	0.836	0.817	0.72	0.813	1					
CGC_R	0.782	0.736	0.706	0.772	0.915	1				
IFO_L	0.709	0.757	0.745	0.750	0.703	0.778	1			
IFO_R	0.725	0.764	0.712	0.77	0.808	0.815	0.898	1		
FMinor	0.791	0.798	0.765	0.83	0.857	0.764	0.675	0.733	1	
FMajor	0.833	0.869	0.782	0.688	0.769	0.706	0.749	0.704	0.756	1

Table 3.3 -- *Continued*

(d)

Neonates										
	CST_L	**CST_R**	**CGH_L**	**CGH_R**	**CGC_L**	**CGC_R**	**IFO_L**	**IFO_R**	**FMinor**	**FMajor**
CST_L	1									
CST_R	0.68	1								
CGH_L	0.454	0.459	1							
CGH_R	0.533	0.56	0.549	1						
CGC_L	0.794	0.779	0.439	0.675	1					
CGC_R	0.76	0.683	0.469	0.569	0.88	1				
IFO_L	0.727	0.612	0.301	0.692	0.787	0.826	1			
IFO_R	0.807	0.705	0.485	0.712	0.846	0.869	0.897	1		
FMinor	0.648	0.628	0.378	0.56	0.861	0.849	0.765	0.848	1	
FMajor	0.701	0.735	0.306	0.642	0.819	0.864	0.867	0.83	0.712	1
Children around puberty										
	CST_L	**CST_R**	**CGH_L**	**CGH_R**	**CGC_L**	**CGC_R**	**IFO_L**	**IFO_R**	**FMinor**	**FMajor**
CST_L	1									
CST_R	0.904	1								
CGH_L	0.768	0.791	1							
CGH_R	0.764	0.832	0.836	1						
CGC_L	0.814	0.889	0.775	0.758	1					
CGC_R	0.776	0.781	0.756	0.79	0.912	1				
IFO_L	0.777	0.827	0.819	0.727	0.881	0.805	1			
IFO_R	0.788	0.83	0.725	0.736	0.853	0.81	0.868	1		
FMinor	0.812	0.856	0.799	0.732	0.886	0.808	0.897	0.878	1	
FMajor	0.783	0.866	0.77	0.672	0.832	0.71	0.886	0.796	0.87	1

3.3.3. Reshuffled Inter-tract Correlation Patterns from Neonates to Children around Puberty

The inter-tract correlations based on each of DTI-derived metrics are reshuffled from neonates to children at puberty. These reshuffled inter-tract correlation patterns can be appreciated from dendrograms based on FA, RD, AxD and MD measurements in Figure 3.5a, 3.5b, 3.5c and 3.5d, respectively. In general, the pairing of homologous tracts is more prominent for child group compared to that of the neonate group based on measurements of all DTI-derived metrics. The reshuffling leading to a more organized pairing among WM tracts is most prominent with the dendrograms based on tract-level RD measurements (Figure 3.5b). For inter-tract correlation based on FA measurement (Figure 3.5a), the tract pairs of CST_L/R becomes clear in the dendrogram of child group, while this pair is not as apparent in neonate group. The IFO_L/R pair is prominent for dendrograms of both neonate and child group based on FA measurements (Figure 3.5a). For dendrograms based on RD measurements (Figure 3.5b), it is clear that all homologous tracts and FMajor/FMinor get paired for child group while the correlation patterns are more random for neonate group. For dendrograms based on AxD (Figure 3.5c) or MD (Figure 3.5d) measurements, stronger and more clusters of the homologous tracts can be observed. The clustering pattern obtained from MD (Figure 3.5d) is similar to that obtained from RD (Figure 3.5b). However, the homologous tracts of child group are not well paired in MD-based dendrogram (Figure 3.5d), compared to those in RD-based dendrogram (Figure 3.5b).

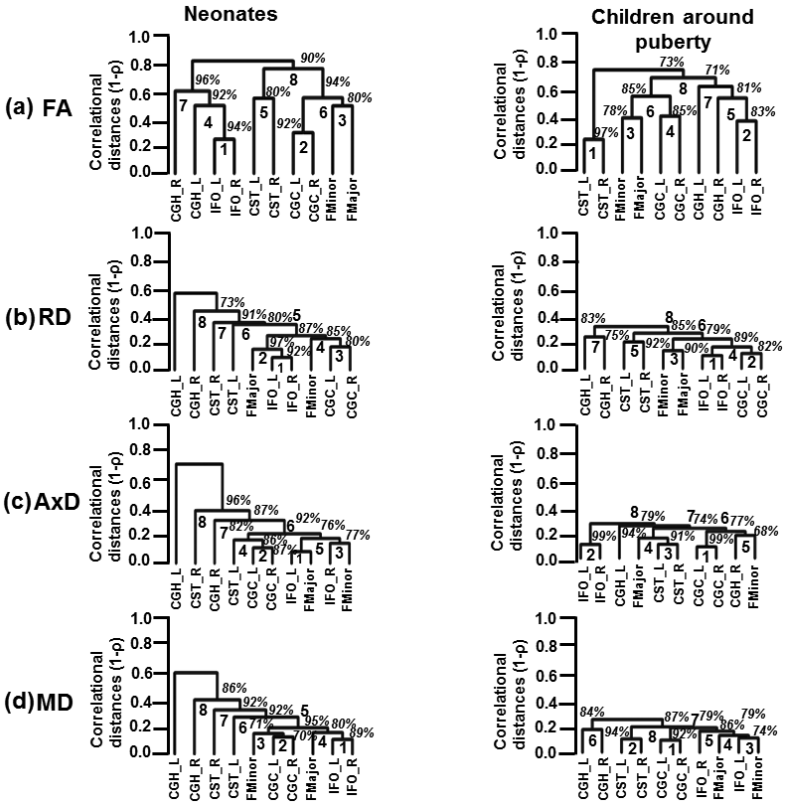

Figure 3.5: Dendrograms depicting the hierarchical clustering pattern obtained from tract-level FA (a), RD (b), AxD (c) and MD (d) measurements for both age groups. The left and right panels show the clustering pattern for neonates and children around puberty, respectively. The ranks of the clustering are shown in bold. The confidence intervals for the clustering (the percentage values) are shown in italics.

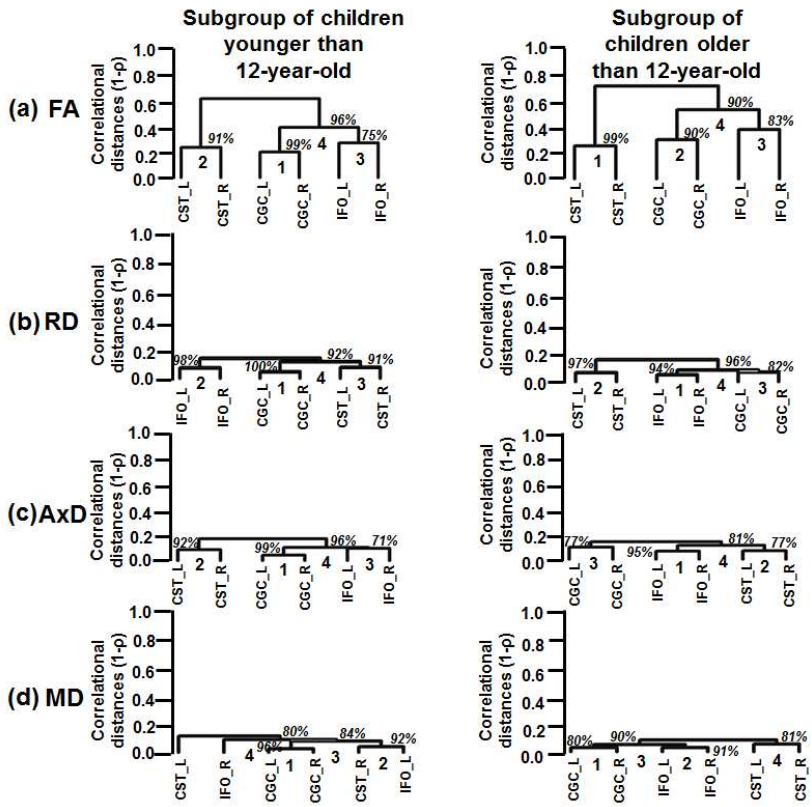

Figure 3.6: Dendrograms depicting the hierarchical clustering pattern obtained from tract-level FA (a), RD (b), AxD (c) and MD (d) measurements for two subgroups of children around puberty. Dendrograms on the left column are for the subgroup of children younger than 12-year-old (9.5 to 12 year); those on the right column are for the subgroup of children older than 12-year-old (12 to 15 year).

3.4. Discussion

In this study, dynamics of inter-tract correlations from birth to onset of adolescence was investigated with DTI-based tract-level microstructural measurements from 10 major WM tracts, CST_L, CST_R, IFO_L, IFO_R, CGC_L, CGC_R, CGH_L, CGH_R, FMajor and FMinor. Higher WM tract integrity, reflected by higher FA, lower MD, AxD and RD, were found for the corresponding tracts from neonates to children around puberty. It is clear that even at birth; nearly all major WM tracts demonstrate similar morphology as those in children around puberty. Significant correlations of homologous

tracts are shown for both neonate and child groups. The comparisons of the inter-tract correlation matrices between the neonate and child group indicated that stronger inter-tract correlations are established during development. Using data-driven hierarchical clustering algorithm with no *a priori* information, we were able to reveal that the linkage patterns of the major tracts differ between the two age groups. Specifically, homologous tracts involved in similar brain functions tend to cluster together for children around puberty especially with tract-level RD measurements. Such clustering patterns of homologous tracts become more prominent from birth to puberty. These changes of inter-tract correlations between neonates and children around puberty suggest inhomogeneous but organized axonal development which causes the reshuffled inter-tract correlation pattern while keeping homologous tracts tightly correlated. To the best of our knowledge, this is the first study investigating dynamics of inter-tract correlations with DTI-based microstructural measurements during early human brain development.

3.4.1. Heterogeneous WM Growth

The WM development is heterogeneous among different tract groups, but more homogeneous among homologous tracts. The heterogeneity among different tract groups includes heterogeneous tract-level measurements of DTI-derived metrics at each time point and heterogeneous changes of these DTI-based tract-level measurements from birth to puberty. The general FA increase and general MD, AxD and RD decrease for all WM tracts in early brain development shown in Figure 2 are consistent with the previous findings (Barnea-Goraly et al., 2005; Dubois et al., 2008; Eluvathingal et al., 2007; Gao et al., 2009b; Giorgio et al., 2010; Lebel et al., 2008; Schmithorst and Yuan, 2010; Snook et al., 2005; Tamnes et al., 2010; Westlye et al., 2010). The heterogeneity among different tract groups is most prominent with FA measurements for children around puberty

(Figure 3.2). From Figure 3.2a, it is clear that FA of CST-L/R (project tract group) is highest in children around puberty, followed by FMajor/FMinor (commissural tract group), IFO-L/R (association tract group) and CGC/H_L/R (limbic tract group). This order of tract group FA measurements is preserved back at birth, but the differences of FA among the tract groups are smaller (Figure 3.2a) for neonatal brains. The heterogeneous changes of tract-level DTI metrics in Figure 3.2 may cause the reshuffling of inter-tract correlation patterns. Quite similar FA values (Figure 3.2a) as well as MD, AxD and RD values (Figure 3.2b-3.2d) of the homologous tracts can be found for both age groups.

3.4.2 Strengthened and Reshuffled Inter-tract Correlation during Development

At birth, significant correlations can be observed based on microstructural measurements of homologous tracts, as shown in upper panels of Figs. 3.3a-3.3d. From Figure 3.4, the general inter-tract correlations from birth to puberty are clearly stronger for all four DTI-derived microstructural measurements. With FA measurement as an example, each entry of correlation matrix in Figure 3.4a can be expanded to the correlation scatterplots such as those shown in panels of Figure 3.3a. Our results also indicated that significantly increased inter-tract correlations are more widespread with correlation coefficients based on RD measurements. For both age groups, correlation coefficients are highest based on AxD measurements (Figure 3.4c) and lowest based on FA measurements (FA). This pattern is especially clear for children around puberty. The overall higher inter-tract correlation coefficients based on AxD measurements suggest that axonal integrity is coherent among the WM tracts within an individual child's brain but varies among different children. To help understand this finding, we could assume a situation when each of the children around puberty has identical AxD for all 10 major WM tracts and the AxD values vary among these children. Under such situation, all inter-tract

correlation coefficients based on AxD would be the perfect value 1. The relatively low inter-tract correlation coefficients based on FA measurements may be caused by heterogeneity of FA values among the WM tracts within each individual subject's brain. Larger variability of FA values among WM tracts can also be observed in Figure 3.2a.

From Figure 3.5a, the FA-based dendrograms show that several homologous tracts are clustered together even for neonates. The left and right IFO are clustered with rank 1 for dendrograms based on tract-level FA of neonatal brains. IFO is thought to play a role in integrating the information from auditory and visual cortices to the prefrontal cortex (Martino et al., 2010). Resting-state fMRI studies have shown consistent pattern of activation in auditory and visual networks in neonates (Doria et al., 2010; Fransson et al., 2007). It is noteworthy that in the resting-state fMRI studies, the connectivity was also identified through correlation of brain-oxygen-level-dependent (BOLD) signal fluctuations in the homologous brain regions. The strong correlations of BOLD signal time courses in visual and auditory networks between left and right hemisphere in neonatal brains may be related to tight cluster of IFO-L and IFO-R involved in these brain functions. Both neonatal and child dendrograms based on FA measurements (Figure 3.5a) have two more separate clusters of projection tracts (CST) and limbic tracts (CGC). All these clusters can also be found in adult brains (Wahl et al., 2010). Figure 3.5b demonstrates one of the most compelling findings with dendrograms based on RD measurements. Although two pairs of homologous WM tracts are clustered together with rank 1 (IFO_L/R) and rank 3 (CGC_L/R), the other two pairs of homologous tracts and FMajor/FMinor are spread all over the dendrogram for neonatal brains (Figure3.5b). It is striking that all 4 pairs of homologous tracts and FMajor/FMinor are tightly clustered together for children around puberty (Figure 3.5b). RD is closely related to myelination of WM tracts (Song et al., 2002). We should be careful to associate the RD values with

myelination due to crossing-fiber and pathological situations (Wheeler-Kingshott and Cercignani, 2009). Nevertheless, during normal brain development with no implication of pathology and with the assumption that tract-level RD measurement for major WM tracts is much less affected by crossing fiber compared to voxelwise RD measurement, tract-level RD is still considered as an important index reflecting the degree of myelination (Eluvathingal et al., 2007; Gao et al., 2009a; Snook et al., 2005; Tamnes et al., 2010; Westlye et al., 2010). The results in Figure 3.5b suggest that organized myelination from birth to puberty plays an important role to reshuffle the inter-tract correlations and result in clustered homologous tracts and clustered functionally similar tracts. The dendrogram patterns based on AxD and MD measurements are different than those based on FA or RD measurements. Unlike RD-based dendrogram (Figure 3.5b), neither of the dendrograms based on AxD or MD measurements for children around puberty shows well organized clusters of all 4 pairs of homologous tracts and FMajor/FMinor (Figure 3.5c and 3.5d). Previous studies (Gao et al., 2009a; Neil et al., 2002; Snook et al., 2005) have found that the measurements of RD decrease dramatically with relatively little changes in AxD of the major white matter tracts during brain development. Our results demonstrated in Figure 3.2 also indicate smaller and more homogeneous changes of AxD from birth to puberty compared to those of RD. These AxD change features may explain why relatively disorganized AxD-based dendrograms remain for children around puberty. From equation (3.1), MD is the linear combination of AxD and RD. The relatively disorganized dendrograms based on MD measurement for child group could also be originated from smaller and more homogeneous changes of AxD measurements during development. Nevertheless, with the brain development, there are still trends for homologous and functionally similar tracts to cluster together in dendrograms based on AxD and MD in Figure 3.5c and Figure 3.5d.

3.4.3. Possible Mechanisms of the Inter-tract Correlation Changes from Birth to Onset of Adolescence

This study on dynamics of inter-tract correlations from birth to onset of adolescence provides unique insight on the well-organized cerebral WM development. The development of human cerebral WM tracts is characterized with enhanced myelination and axonal integrity. From the results in this study, inhomogeneous RD decreases among the tracts take place during development. More (84.4% of all independent correlation coefficients) inter-tract correlations become stronger with RD measurements, compared to those with any other DTI metric measurements. In addition, the dendrograms based on RD (Figure 3.5b) demonstrate that all 4 pairs of homologous tracts and FMajor/FMinor are tightly clustered at puberty while only 2 pairs of homologous tracts are clustered at birth. The cerebral WM at birth is likely to be in a relatively random and disorganized status. Due to close relationship of RD with the myelination of WM tract, these results suggest that inhomogeneous enhancement of myelination rather than strengthening of axonal integrity plays a key role in reshaping the WM configuration during development. Both genes and experiences could also play a role to adjust WM microstructures so that the homologous WM tracts reach to a coherent status to meet the needs of certain brain functions by the time of onset of adolescence. Although it is not known by what mechanism inhomogeneous myelination is modulated during WM maturation, our results suggest that the myelination process is precisely controlled so that all 4 pairs of homologous tracts and FMajor/FMinor are clustered together around puberty (Figure 3.5b).

3.5. Limitations of this Study and Future Directions

There are several issues which may affect the results in this study. Five pairs of major WM tracts were chosen for this study due to the fact that only these five pairs of major WM tracts could be reproducibly traced with neonate DTI. The numbers of participated subjects, 26 for neonates and 28 for children, just exceeds 25 which is needed for correlation analysis of five pairs of WM tracts. Higher sample numbers could increase the confidence level in analysis of hierarchical clustering. Corrections for multiple comparisons were only performed on testing the correlation matrices against identity matrix and matrix with equal non-diagonal elements. No correction was performed on the hierarchical clustering results due to lack of any known methods to perform such a correction on dendrograms. The accuracy of measuring tract-level DTI-derived metrics plays a key role in inter-tract correlations. This accuracy is affected by three major factors. They are the crossing-fiber factor, SNR of the data and partial volume effects. Both the tractography and the DTI-derived measurements are biased at crossing-fiber regions (Wheeler-Kingshott and Cercignani, 2009). With single tensor model and tractography method of fiber assignment by continuous tracking (FACT) (Mori et al., 1999), it is apparent that the tracing method adopted in this study cannot resolve the crossing-fiber issue, resulting in imperfect binary mask of the traced tracts for tract-level measurements of DTI metrics. Nevertheless, the tracing protocol (Wakana et al., 2007) based on FACT tractography captures the core of the major WM tracts and is still widely used in the field. We conducted two repetitions of diffusion MRI and the SNR is sufficient for data acquisition with 3T magnet. With diffusion imaging resolution $2x2x2mm^3$ for neonates and $2x2x2.2mm^3$ for children around puberty, the partial volume effects are inevitable. However, it seems the effects of imperfect WM fiber tracing offsets the partial volume effects for obtaining accurate tract-level DTI metrics, in that the tracing

algorithm adopted in this study cannot trace the small branches of the fibers where the problem of partial volume effects is most prominent. Ranks of the DTI measurements, instead of measured metrics themselves, were used for correlation pattern analysis. Despite possibly different levels of biases of the DTI metric measurements caused by partial volume effects due to different head sizes between neonates and children, the similar shifts of measurements in the same age group could have minimum effects on the rank of metric measurements and therefore minimum effects on the Spearman's rank correlation patterns. Although same types of scanners were used in this study, systematic differences of the scanners may affect the DTI analysis results. To make sure that the effects of systematic differences caused by two different scanners are minimal, a healthy young subject ("*in vivo* human phantom") was scanned in both scanners used in this study and with the same DTI sequence. The quantitative comparisons were also conducted. Quantitative DTI measurement differences caused by scanner difference were tested to be within the range of variability of scanning the same subject twice with one scanner (Saxena et al., 2012). With the same type of scanners used in this study and rigorous quality control of both scanners, the effects of scanner differences on the presented results in this study are thus negligible. The group of children around puberty included both pre-puberty and post-puberty subjects. The age difference between the two groups, newborns and children around puberty, is much larger than the age difference within the group of around puberty. Therefore, we hypothesized that the intra-group WM developmental heterogeneity for the children group exists, but is not big enough to affect the inter-group results presented in this study. This has been tested and proved by Figure 3.6. In Figure 3.6, we separated the children around puberty into two subgroups, pre-puberty (9.5 to 12 year) and post-puberty (12 to 15 year). With reduced sample number for each subgroup, we could conduct the correlation analysis for 6 tracts (3 pairs of

homologous tracts). It is shown in Figure 3.6 that homologous tracts are still clustered together in both subgroups, like the cluster patterns shown in the right column of Figure 3.5. Moreover, the linkage patterns are very similar between the two subgroups, with slight dendrogram rank change.

The tracts obtained using the FACT technique used in this study is biased due to its inability to track through the crossing fiber regions as mentioned above. Hence the tracts obtained in this study do not faithfully represent the exact tract connections between different regions of the brain and could possibly influence the hierarchical tractography classification obtained. Since the fiber tracking approach depends heavily on the myelination and the organization of the white matter fibers which are yet not fully developed in neonatal subjects in this study, there is a possibility that the hierarchical tractography classification is biased. However it was shown that the hierarchical classification obtained using the tract-tracing approach (Wahl et al., 2010) and independent component analysis (ICA) approach (Li et al., 2012) was similar for an older group of healthy subjects and hence this study should be repeated by ICA technique with more subjects in each group to replicate the findings that might remove the discrepancies obtained in the known tract connections between different brain regions and the hierarchical tractography classification due to the tract-tracing approach.

In the future, several improvements can be made to address the issues affecting accuracy of measuring tract-level DTI metrics. The tracking methods (Behrens et al., 2007; Tournier et al., 2004) which are capable of resolving the crossing-fiber issue can be adopted. Although there is no general consensus on which parameters can replace these four DTI-derived metrics and better characterize the WM microstructure, there have been a few metrics such as general fractional anisotropy (GFA) (Fritzsche et al., 2010; Tuch, 2004; Zhan et al., 2010), generalized anisotropy (GA) (Ozarslan et al., 2005),

mode of anisotropy (Douaud et al., 2011; Ennis and Kindlmann, 2006) and fractions (Hosey et al., 2008; Jbabdi et al., 2010) which are less sensitive to crossing-fiber problem. In addition, tract-based spatial statistics (TBSS) from FSL (http://www.fmrib.ox.ac.uk/fsl) (Smith et al., 2006) can be used to alleviate the partial volume effects, as shown in the study of FA correlations in adults (Li et al., 2012).

3.6. Conclusion

In conclusion, inter-tract correlation changes during development from birth to onset of adolescence were investigated with tract-level FA, RD, AxD and MD measurements. Stronger and enhanced microstructural inter-tract correlations were found during development. The linkage patterns of the major tracts also differ with the dendrograms of two age groups due to brain development. These changes of microstructural correlations from birth to puberty suggest inhomogeneous but organized myelination processes which cause the reshuffled inter-tract correlation pattern and make homologous tracts tightly clustered. Especially RD-based dendrograms reveal that all 4 pairs of homologous tracts and FMajor/FMinor investigated in this study are tightly clustered for children around puberty while only 2 out of these 5 pairs of tracts are clustered at birth, indicating important role of myelination to reshape the WM configuration. It opens a new window to study white matter tract development and can be potentially used to investigate atypical brain development due to neurological or psychiatric disorders.

Chapter 4

Exploring the Perinatal Brain Network with Diffusion MRI and Graph Theory

4.1. Introduction

The human brain is a highly structured organ but its origin is just a simple tube (Huang and Vasung, 2013; Nolte, 1999). How does this simple tube advances to become the most complex yet highly structured organ of the body is still elusive? Considering the significance of delineating the structural changes to understand the very complicated process of human fetal brain development, it is not striking that neuroanatomists have been studying this process since last two centuries. The very earliest report about the structure of the human brain came in 1816 from embryological dissection of postnatal human brains (Tiedemann, 1816) which was followed by several other noted neuroanatomists (Chi et al., 1977; Poliakov, 1949). Histology, by far, has been the most widely used and a dominant modality to study the early neural structure of developing human brain (Rakic, 1988; Sidman and Rakic, 1982; Volpe, 2001). Comprehensive atlases based on histological slides became available a few years ago (Bayer and Altman, 2005; O'Rahilly and Muller, 2006).

Although unmatched information about the human fetal brain could be obtained from histological sections; it requires highly trained people to conduct these studies, it is time consuming and could be subjective (Axer, 2011). As mentioned in the previous chapters, DTI has the capability to non-invasively image the neural structures of developing human brain. The water molecules diffusing inside the brain has a tendency to diffuse in a direction parallel to the axons rather than perpendicular to it (Beaulieu, 2002; Le Bihan, 2011; Mori, 2007). The microstructural and morphological changes of white matter axons connecting different cortical areas of the developmental brains has been studied in great details by estimating DTI derived metrics such as FA, AxD and RD

of white matter fiber bundles(Dubois et al., 2008; Eluvathingal et al., 2007; Gao et al., 2009a; Giorgio et al., 2010; Huang and Vasung, 2013; Huang et al., 2009; Huang et al., 2006; Huppi, 2011; Huppi and Dubois, 2006; Huppi et al., 1998; Kostovic and Jovanov-Milosevic, 2006; Lebel et al., 2008; Mukherjee et al., 2002; Snook et al., 2005). Using the direction of the fastest diffusion of the water molecules, one can assess the structural connectivity consisting of heterogeneous white matter fiber bundles connecting different brain regions (Dennis et al., 2011; Hagmann et al., 2010). This structural connectivity underlies the formation and evolution of the human brain network during development. The structural connectivity could be thought of as a network or “wiring” of the human brains which is responsible for normal cognitive and executive functions. Deviation from normal network development has been found to be associated with developmental cognitive brain disorders such as mental retardation, autism, schizophrenia, bipolar disorder and language impairment (Bullmore and Sporns, 2009; Power et al., 2010).

The application of graph theory to study human brain network has advanced our understanding of the structural and functional brain networks (Bullmore and Sporns, 2009; He et al., 2007; He and Evans, 2010; van den Heuvel et al., 2009; van den Heuvel and Sporns, 2011). The development of functional brain networks has been studied using functional MRI (f-MRI) (Dosenbach et al., 2010; Fair et al., 2008; Fair et al., 2007; Power et al., 2010; Supekar et al., 2009) and recently, dMRI has been used to study structural brain connectivity (Dennis et al., 2011; Gong et al., 2009; Hagmann et al., 2010). Characterizing normal perinatal brain network development will not only expand our understanding of formation of functionally significant brain circuits, but also shed light on our understanding of the abnormal network development associated with child health. The axonal connectivity during early brain development undergoes dramatic structural changes causing significant variations of brain network properties (Huang et al., 2009;

Huang et al., 2006; Judas, 2011; Kostovic and Jovanov-Milosevic, 2006; Takahashi et al., 2012; Vasung et al., 2010; Vasung et al., 2011). The advantage of dMRI to probe structural brain connectivity using DTI based tractography, makes it an ideal choice to study perinatal structural brain development. However, with the difficulty of acquiring high quality DTI data of perinatal brains, brain network development has not been characterized in the literature. Studying perinatal brain network development in the continuous age range of 31wg to 40wg will improve our understanding whether there is a monotonic change of the network configuration or it follows some pattern of brain development.

In this study, we explored the development of human brain structural networks with high resolution DTI data of 15 in vivo neonatal brains from 31wg to 40wg. The brain was parcellated into 58 cortical regions or nodes using JHU neonatal template (Oishi et al., 2011) and structural connectivity between these nodes were quantified with deterministic fiber tracking (Mori et al., 1999). Topological changes during perinatal brain development were characterized with graph theoretical analysis (Bullmore and Sporns, 2009). Various graph theoretical network metrics such as network strength, global and local efficiency, modularity and small-worldness were quantified and compared for the developing brains.

4.2. Materials and Methods

4.2.1. Primer on Graph Theory

Graph theory is a branch of mathematics developed in the 18th century and is credited to Euler's original publication in which he used a graphical representation to show that it was impossible to traverse each city of Koningsberg's seven bridges exactly once and return to the starting point (Euler, 1736). A graph in the context of graph theory

is defined as a set of nodes or vertices that are linked together by connections or edges. The connections of the graph can be weighted or unweighted and can be directed or undirected. Graph theoretical methods have since been applied to many real-world systems to provide an abstract representation of the system's elements and their interactions (Watts and Strogatz, 1998). Many of the efficient real-world systems have been shown to share common network properties although the systems themselves were inherently diverse such as the neural network of the *Caenorhabditis elegans* worm, the power grid of the western United States and the social network of the Screen Actors Guild (Watts and Strogatz, 1998). These networks were described as having small-world network phenomenon. Recently, such small-world architectures have also been shown in several empirical studies of human structural and functional brain networks (Bullmore and Sporns, 2009; Hagmann et al., 2010; He et al., 2007; He and Evans, 2010). Several other topological properties derived from graph theoretical approaches such as global, local and cost efficiency, strength, and modularity have also been measured in relation to human brain networks (Bullmore and Sporns, 2009; Hagmann et al., 2010; He et al., 2007; He and Evans, 2010). Structural and functional brain networks can be explored using graph theory with the following 4 steps, shown graphically in Figure 4.1 (Bullmore and Sporns, 2009):

I. Defining the nodes: Nodes can be defined as the electrodes used for electroencephalography (EEG) or magnetoencephalography (MEG) or any combination of voxels from fMRI data for studying functional brain networks or as anatomically defined cortical regions from histological, MRI or dMRI data for studying structural brain networks.

II. Defining the edges: Edges can be defined as the cross-correlation between the regions of interest in fMRI data or inter-regional correlations

between the electrodes used in MEG or EEG studies for functional network analysis or number of fibers between two regions of a dMRI data for structural connectivity analysis.

III. Building the connectivity matrix: An adjacency, connectivity or an association matrix is generated by compiling all the pairwise association between nodes.

IV. Deriving the network properties: The connectivity matrix of step III is then evaluated to derive various topological network measures by comparing the matrix to equivalent parameters of a population of random networks.

Various network properties are described later in the section of network properties.

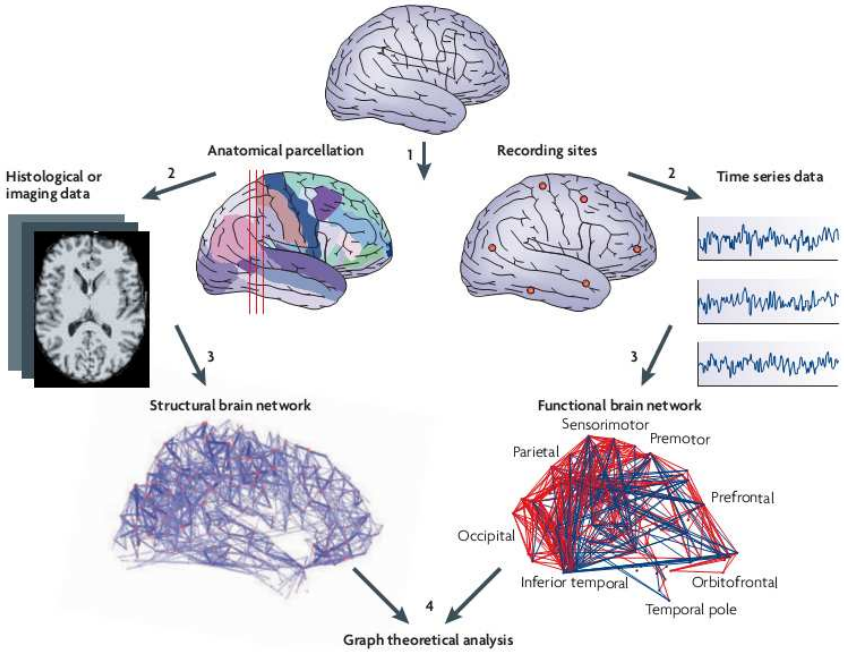

Figure 4.1: Graphical illustration of the technique to perform graph theoretical analysis. Nodes of the analysis are shown by various colors on the anatomical parcellation of the brain or the red circles on the functional recording data; the edges for dMRI are shown by the fiber tracts or the correlation strength between the different nodes on the functional data (Bullmore and Sporns, 2009).

4.2.2 dMRI Acquisition for In-vivo Human Brain

High quality dMRI data was acquired from 15 neonatal brains between 31wg and 40wg at Children's Medical Center (CMC) at Dallas using a Philips 3T MR scanner. All included neonates were part of cohort for studying normal development and were selected after rigorous screening procedures conducted by the neonatologist at CMC. Exclusion criteria include mother's excessive drug or alcohol abuse during pregnancy; grade III-IV intraventricular hemorrhage; periventricular leukomalacia; hypoxic-ischemic encephalopathy; lung disease or brochopulmonary dysplasia; necrotizing enterocolitis that requires intestinal resection or complex feeding/nutritional disorders; defects or anomalies of forebrain, brainstem or cerebellum; brain tissue dys- or hypoplasias; abnormal meninges; alterations in the pial or ventricular surface; or white matter lesions. dMRI data were acquired using a single-shot EPI with SENSE parallel imaging scheme (SENSitivity Encoding, reduction factor =2.5). The imaging parameters were: resolution=1.5x1.5x1.5 mm^3, identical 30 independent diffusion-weighted directions (Jones et al., 1999a) uniformly distributed in space, b-value =1000 s/mm^2, repetition=2. For dMRI, the total acquisition time was 11 minutes. In addition, 15 neonatal subjects in the continuous age range between 30wg and 40wg were scanned at CMC. All mothers gave informed written consents approved by Institutional Review Board of the CMC.

4.2.3. Network Construction for the Developing Brains

The workflow of structural network construction including cortical parcellation (Figure 4.2a), dMRI tractography (Figure 4.2b) and generation of connectivity matrix (Figure 4.2c) of the neonatal brains can be seen in Figure 4.2. A 58x58 symmetric weighted cortical network or graph representing the structural connectivity of whole-brain was constructed for each subject after node and edge definitions described in details

below. Graph theoretical methods were then applied to derive various network properties for each group.

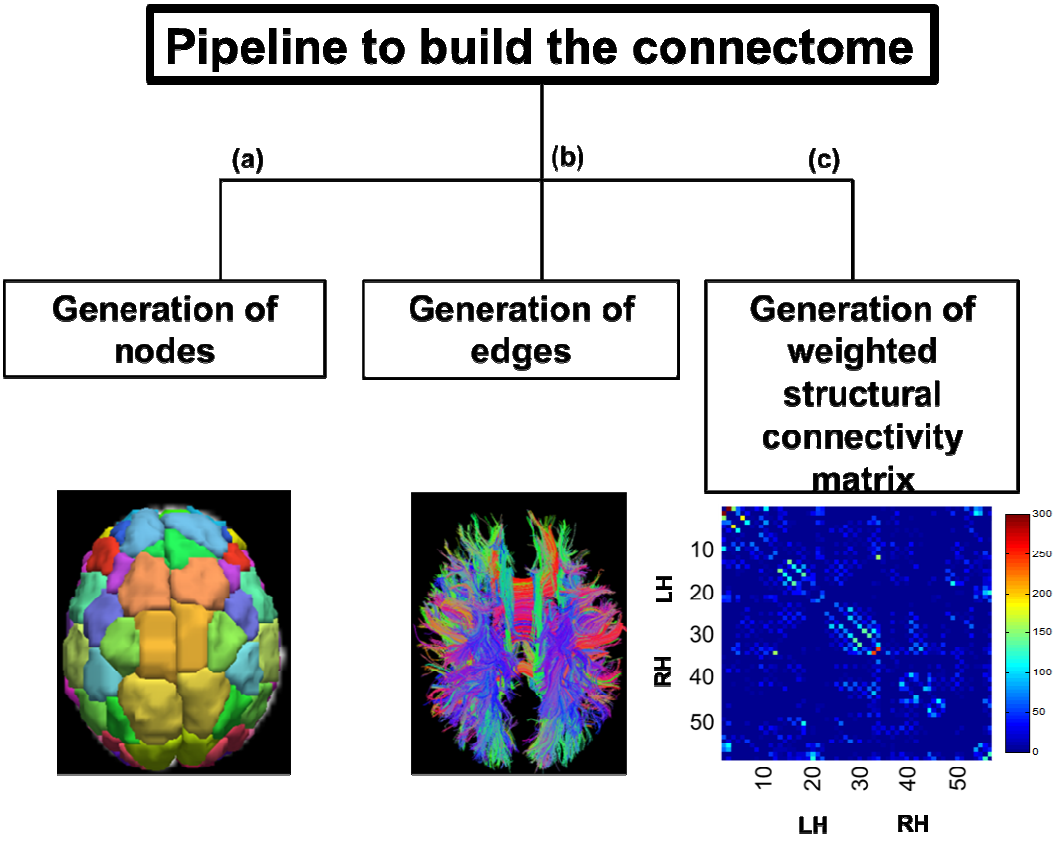

Figure 4.2: Illustration of the pipeline to build the connectome. Nodes were derived from a template free parcellation algorithm and are overlaid as different colors on (a); edges connecting the nodes were obtained from deterministic fiber tracking as shown in (b) and connectivity matrix generated from these edges is shown in (c).

4.2.3.1. Cortical Parcellation for Network Node Definition

The procedure for obtaining the nodes has been previously described (Gong et al., 2009; Huang et al., 2013). Briefly, the cortical parcellation was obtained by transforming the JHU template (Oishi et al., 2011) to native space using a transformation matrix that was obtained by registering the non-diffusion weighted b0 image to b0 image of the JHU template using SPM8 (http://www.fil.ion.ucl.ac.uk/spm). The resulting JHU

template with 58 parcellated regions or nodes was hence in the native space. Of note, discrete labeling values were preserved by the use of nearest-neighbor interpolation method.

4.2.3.2 dMRI Tractography for Network Edge Definition

With each of the 58 parcellated nodes as seeds, deterministic tracking was performed using TrackVis (Wang et al., 2007). A filtering algorithm was applied to retain only those fiber tracts that connect two different nodes and a 58x58 weighted connectivity matrix was established for each subject.

The weight of the 58x58 weighted connectivity matrices was obtained by scaling the number of fibers connecting any two nodes by the average FA of the fibers connecting those two nodes (Liu et al., 2012). Since the resolution was same for each subject in the continuous age range cohort, fiber count represents an unbiased measurement of connectivity between any two nodes. FA indicates the microstructural integrity of the white matter fibers which will strengthen with brain development and hence it was used as a scaling factor to better characterize the early brain network.

4.2.4. Network Analysis with Graph Theory

A brain structural network (graph) G is composed by N nodes and K edges. To characterize topological organization of structural networks, the following graph measures under different thresholds were calculated: network strength, global efficiency, local efficiency, normalized shortest path length, normalized clustering coefficient and small-worldness (Rubinov and Sporns, 2010). All network analysis was performed using the in-house GRETNA software (Huang et al., 2013).

4.2.4.1 Network Strength, Efficiency and Small-worldness

For a weighted brain network or graph, we first computed the network strength (Equation 4.1) as the average of the strengths across all of the nodes in which the strength of a node is the sum of the edge weights (w_{ij}) linking to it. Then, we computed the weighted clustering coefficient (Equation 4.2), which quantifies the extent of local interconnectivity or cliquishness in a network, and the weighted shortest path length (Equation 4.3), which quantifies the ability for information propagation in a network in parallel. A network is said to be small-world if it has similar shortest path lengths but higher clustering coefficients than degree-matched random networks (Watts and Strogatz, 1998). In other words, a small-world network has the normalized clustering coefficient, $\gamma = C_p^{real} / C_p^{rand} > 1$ and the normalized shortest path length, $\lambda = L_p^{real} / L_p^{rand} \approx 1$. These two measurements can also be summarized into a simple quantitative measurement, small-worldness, $\sigma = \gamma / \lambda$ (Equation 4.4). We also computed the global efficiency as the inverse of shortest path length, the local efficiency as a measure of the efficiency of local information transfer between neighboring nodes, and the cost efficiency as the relative network efficiency normalized by its cost (Equations 5-7, respectively).

Network strength: For a network (graph) G with N nodes and K edges, we calculated the strength of G as:

$$S_p(G) = \frac{1}{N} \sum_{i \in G} S(i) \qquad [4.1]$$

where S(i) is the sum of the edge weights w_{ij} linking to node i. The strength of a network is the average of the strengths across all of the nodes in the network.

Small-world properties: Small-world network parameters (clustering coefficient, Cp, and shortest path length, Lp) were originally proposed by Watts and Strogatz (Watts and Strogatz, 1998). In this study, we investigated the small-world properties of the weighted

brain networks. The clustering coefficient of a node i, C(i), which was defined as the likelihood whether the neighborhoods were connected with each other or not, is expressed as follows:

$$C(i) = \frac{2}{k_i(k_i - 1)} \sum_{j,k} (\overline{w}_{ij} \overline{w}_{jk} \overline{w}_{ki})^{1/3} \quad [4.2]$$

where k_i is the degree of node i, and $\overline{w}$ is the weight, which is scaled by the mean of all weights to control each participant's cost at the same level. The clustering coefficient is zero, C(i) = 0, if the nodes are isolated or with just one connection, i.e., $k_i = 0$ or $k_i = 1$. The clustering coefficient, Cp, of a network is the average of the clustering coefficient over all nodes, which indicates the extent of local interconnectivity or cliquishness in a network (Watts and Strogatz, 1998).

The path length between any pair of nodes (e.g., node i and node j) is defined as the sum of the edge lengths along this path. For weighted networks, the length of each edge was assigned by computing the reciprocal of the edge weight, $1/w_{ij}$. The shortest path length, L_{ij}, is defined as the length of the path for node i and node j with the shortest length. The shortest path length of a network is computed as follows:

$$L_p(G) = \frac{1}{N(N-1)} \sum_{i \neq j \in G} L_{ij} \quad [4.3]$$

where N is the number of nodes in the network. The L_p of a network quantifies the ability for information propagation in parallel.

To examine the small-world properties, the clustering coefficient, C_p, and shortest path length, L_p, of the brain networks were compared with those of random networks. In this study, we generated 100 matched random networks, which had the same number of nodes, edges, and degree distribution as the real networks (Maslov and Sneppen, 2002). Of note, we retained the weight of each edge during the randomization procedure such

that the weight distribution of the network was preserved. Furthermore, we computed the normalized shortest path length (lambda), $\lambda = L_p^{real} / L_p^{rand}$, and the normalized clustering coefficient (gamma), $\gamma = C_p^{real} / C_p^{rand}$, where L_p^{rand} and C_p^{rand} are the mean shortest path length and the mean clustering coefficient of 100 matched random networks. Of note, the two parameters correct the differences in the edge number and degree distribution of the networks across individuals. A real network would be considered small-world if $\gamma > 1$ and $\lambda \approx 1$ (Watts and Strogatz, 1998). In other words, a small-world network has not only the higher local interconnectivity but also the approximately equivalent shortest path length compared with the random networks. These two measurements can be summarized into a simple quantitative metric, small-worldness,

$$\sigma = \gamma / \lambda \qquad [4.4]$$

which is typically greater than 1 for small-world networks.

Network efficiency: The global efficiency of G measures the global efficiency of the parallel information transfer in the network (Latora and Marchiori, 2001), which can be computed as:

$$E_{glob}(G) = \frac{1}{N(N-1)} \sum_{i \neq j \in G} \frac{1}{L_{ij}} \qquad [4.5]$$

where L_{ij} is the shortest path length between node i and node j in G.

The local efficiency of G reveals how much the network is fault tolerant, showing how efficient the communication is among the first neighbors of the node i when it is removed. The local efficiency of a graph is defined as:

$$E_{loc}(G) = \frac{1}{N} \sum_{i \in G} E_{glob}(G_i) \qquad [4.6]$$

where Gi denotes the subgraph composed of the nearest neighbors of node i.

The cost efficiency of G is defined as the global efficiency divided by the cost of the network.

$$E_{cost}(G) = E_{glob}(G) / Cost(G) \quad [4.7]$$

The network cost was to measure the expense for building up the connecting elements of a graph. Typically, the cost of a connection is proportional to its distance, which is the inverse of the edge weight in this study, and therefore the overall cost of a graph is derived by taking the sum of distance, i.e. Cost = sum ($1/w_{ij}$). The cost efficiency measures the relative network efficiency normalized by its cost (Huang et al., 2013).

4.3. Results

4.3.1. Cortico-cortical Connections of Perinatal Human Brain Cohorts

Figure 4.3 shows the cortico-cortical connections for a 31wg, 35wg and 40wg brain. Sagittal view (top panel) and axial view (bottom panel) are shown for each subject. As can be seen from Figure 4.3, the orientation of the fibers represented by the color encoded by the fibers shows a significantly heterogeneous trend with brain development. The white matter fibers of 31wg have more green encoded fibers overall visually, and with perinatal brain development the fibers become more heterogeneous shown by a very heterogeneous color pattern in 35wg and 40wg brains.

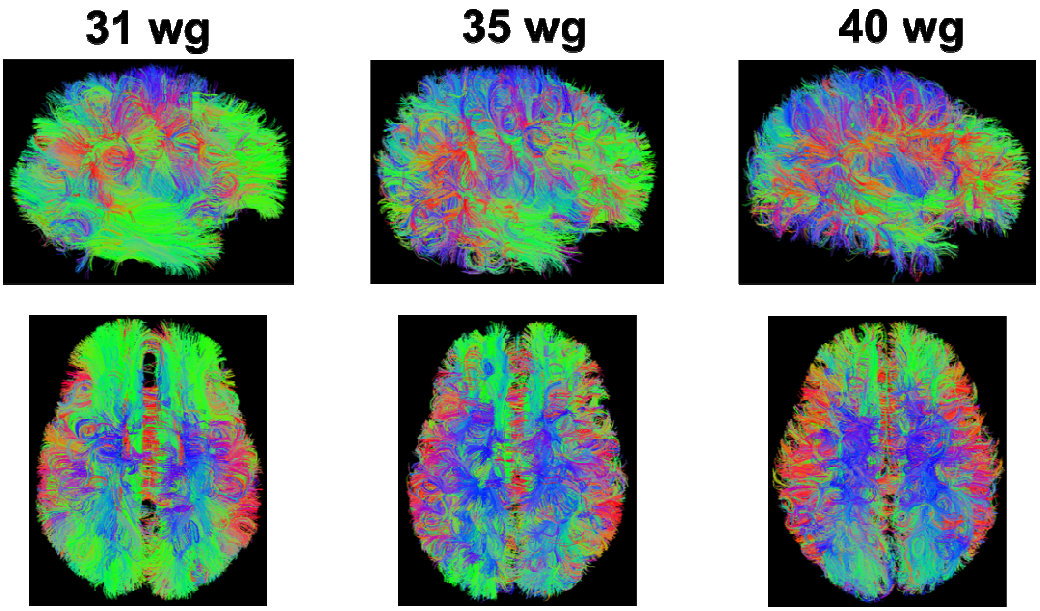

Figure 4.3: Cortico-cortical fiber connections are shown for a representative subject in a 31wg, 35wg and 40wg brain. Top row show the sagittal view and bottom row shows the axial view.

4.3.2. Dynamics of the Connectivity Matrix during Perinatal Brain Development

Figure 4.4 shows the weighted connectivity matrix of a 31wg, 35wg and 40wg brain. It can be appreciated that connectivity strength increases with brain development shown by red color in most of the elements of the 40wg connectivity matrix as compared to 31wg or 35wg brain. It can also be seen from Figure 4.4, that inter-hemispheric connectivity becomes stronger during perinatal brain development which could be appreciated from more red color elements in 40wg brain as compared to the other groups.

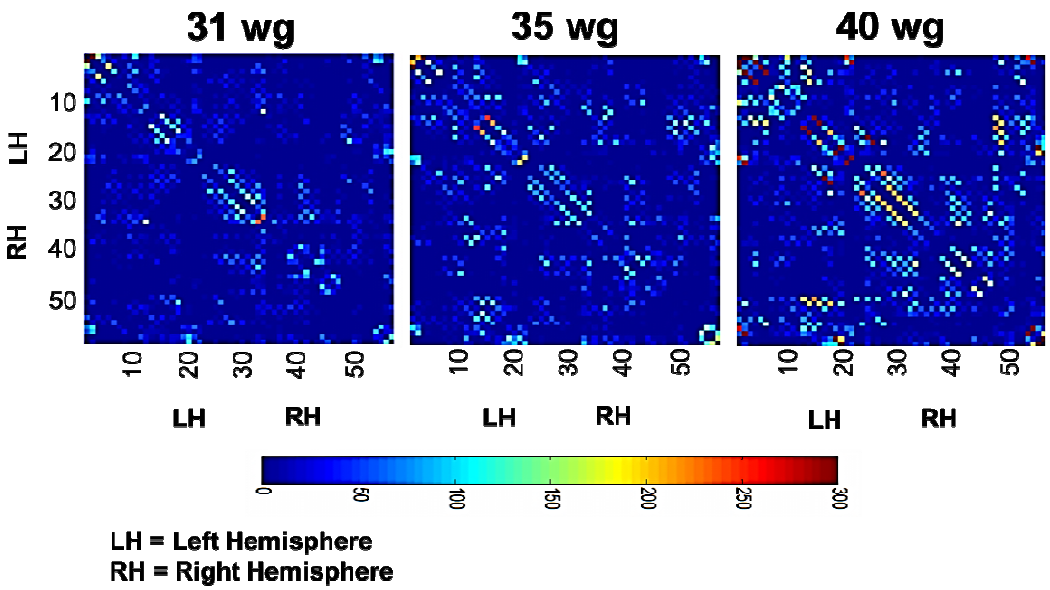

Figure 4.4: Connectivity matrix is shown for 3 timepoints; 31 wg in the leftmost panel, 35wg in the middle panel and 40wg in the rightmost panel

4.3.3. Dynamics of the Network Strength, Efficiency and Small-world Properties during Brain Development

The network strength, efficiency and small-world properties of three age groups are shown in Figure 4.5. The network strength, global efficiency, local efficiency and cost efficiency increase uniformly with age as shown in Figure 4.5. Normalized L_p increase uniformly with age while normalized C_p and small worldness does not show an increasing trend with perinatal brain development. Small-world organization is evident at all ages with a normalized C_p greater than 1 and normalized L_p close to 1.

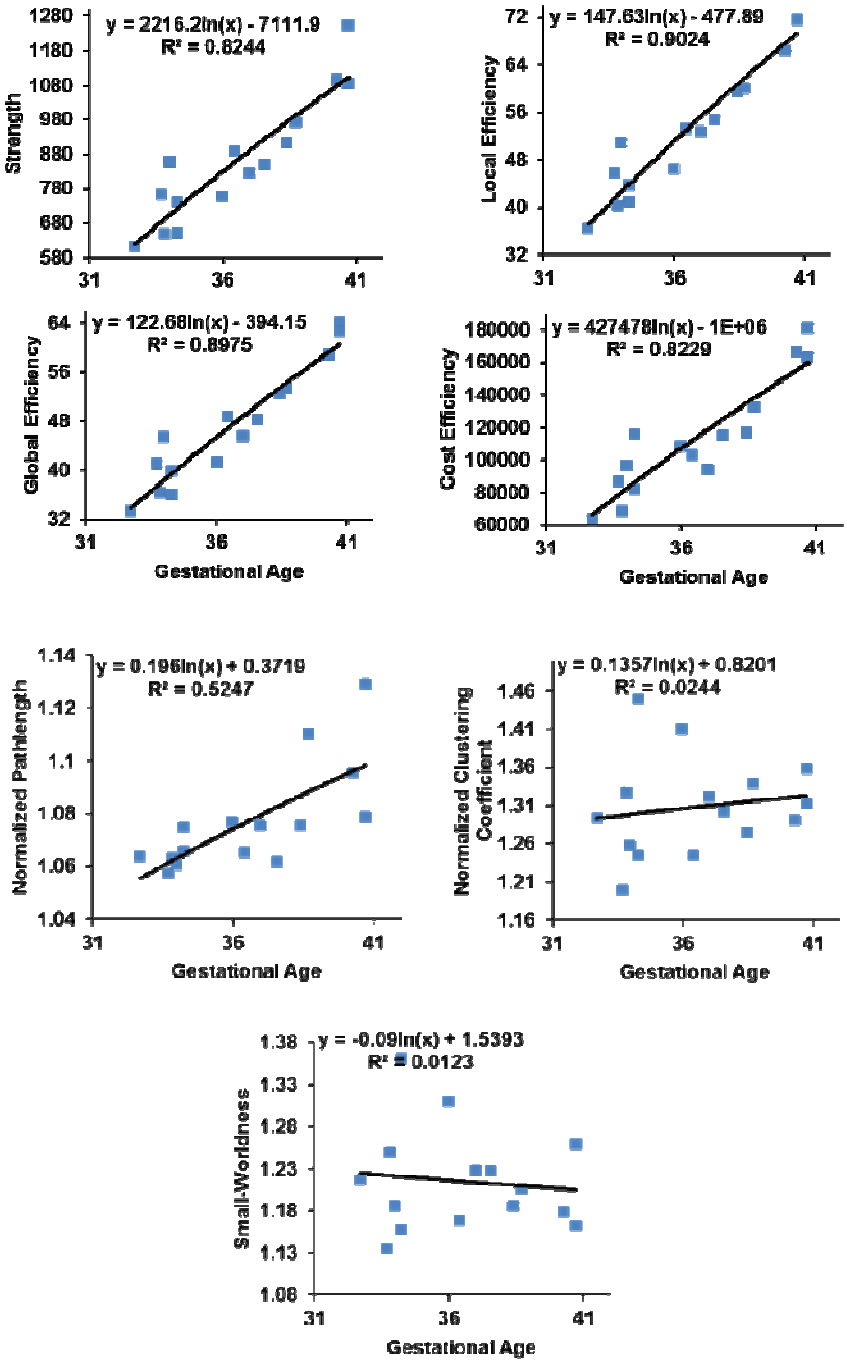

Figure 4.5: Various network properties are shown as scatterplots as a function of gestational age in weeks. Each dot represents the result from an individual subject.

4.4 Discussion

The early human brain development during continuous age range of 31wg to 40wg is characterized with dramatic changes of structural connectivity and network configuration. Moreover, the brain structural configuration was evolved into a stronger and a more efficient organization with human brain development. Our results show a monotonic increase in all the network derived metrics except clustering coefficient and small-worldness. The increase in the efficiency during perinatal brain development also suggests that the stronger network configuration is obtained from a combination of microstructural development of WM fiber tracts combined with synaptic pruning of small WM fibers. To our knowledge, this study is the first comprehensive network investigation during perinatal brain development using graph theoretical approaches.

The network quantification shows a stronger and more efficient connectivity with development. The increase in network strength, global, local and cost efficiency is increasing in a monotonic fashion indicating that brain is getting more efficient during perinatal brain development (Figure 4.5). Increase in the normalized L_p between 31wg and 40wg indicates that during early brain development, communication processes between different regions of the brain become more integrated but the insignificant change in normalized C_p indicates that the communication is not yet well segregated (He and Evans, 2010). However, small-world organization does exist at all the three landmark points when compared to 100 matched random networks indicating that brain neither has a random nor a very regular lattice structure even as early as 31wg (Watts and Strogatz, 1998). Recent studies have shown that small-worldness property exists in brain during very early stages of life as early as two weeks old (Huang et al., 2013; Yap et al., 2011). The dMRI studies have shown that the brain has increased efficiency and strength with brain maturation from 2-to 18 year old (Hagmann et al., 2010) and our study show that

the dynamics of these network metrics are present even during the perinatal brain development. Hence our results suggests that during brain development, network integration increases but segregation is a process that takes place after birth as shown in the previous studies (Hagmann et al., 2010; Yap et al., 2011).

Although there have been no functional connectivity studies done at the chosen three landmark points, previous studies on development of functional connections have suggested that formation of the human brain network is complemented by important structural development (Dosenbach et al., 2010; Fair et al., 2008; Fair et al., 2007; Power et al., 2010; Supekar et al., 2009). These developments include myelination of the long range WM fibers (Giedd et al., 1999; Paus et al., 1999) and pruning of the short range WM fibers (Chugani et al., 1987; Huttenlocher et al., 1982; Takahashi et al., 2012). Brain maturation in terms of functional connectivity can be linked to improved structural connectivity and has been shown that structural connectivity might itself manifest some changes to incorporate later matured functional connectivity (Greicius et al., 2009; Honey et al., 2009; van den Heuvel et al., 2009). Unlike functional connectivity, structural connectivity evaluated from dMRI relies solely on physical axonal connections. Hence the brain regions that communicate via a relay process cannot be studied with structural connectivity analysis using dMRI. It is likely that the strengthening of the growing structural network is the outcome of both the microstructural enhancement (including myelination) of the long range WM fibers and pruning of the short range fibers. The analysis of integrated effects of microstructural enhancement of long range fibers and pruning of short range fibers in the future may provide further insights on the underlying mechanism of growing human brain network.

4.5. Limitations of the Study and Future Work

There are several limitations of this study. Firstly, the tractography technique used in our study uses deterministic tracking (Mori et al., 1999) that has known limitations at the regions where the fibers cross. This study should be replicated with the most advanced probabilistic tractography technique (Behrens et al., 2007) to investigate whether the tracking algorithm has any significant role in describing the results. Secondly, the choice of edge weight and number of nodes has been continuously debated and several studies have proposed different number of nodes and edge weights (Hagmann et al., 2010; Zalesky et al., 2010). Evaluating change in network properties with different number of nodes and edge weights might also give new insights into perinatal human brain development. Furthermore, the effect of long range connections and short range connections needs to be investigated in detail to evaluate the effects of each of these connections on the brain connectivity. Evaluating the effect of gyrification or cortical folding should be investigated and its effect on shaping the overall brain connectivity needs to be evaluated. Furthermore, the results are shown from only 15 subjects and the study needs to be replicated with a larger sample size.

4.6. Conclusions

In conclusion, this study shows that a stronger and efficient network is formed during early human brain development. All of the network derived metrics showed a monotonic increase with brain development. Small-worldness was evident at all ages and was retained during brain development. The network property changes found in this study could be underlined by significant growth of major long association white matter tracts with increased myelination and concurrent pruning of small fibers during perinatal brain development.

Chapter 5

Conclusion and Outlook

As mentioned in the previous chapters, dMRI and DTI is a tremendous non-invasive modality to virtually dissect the human brain. Several quantitative metrics can be derived by fitting the signal to the known single tensor model and the metrics of the fiber tracts of interest can be compared with patient population to either diagnose the problem at a very early stage or longitudinally follow up the patient to evaluate drug efficacy.

However, it was shown in chapter 2 that FA which is by far the most widely used metric derived from DTI in clinical research has severe underestimation at the region of crossing fibers. Since in a patient population it is the entire tract that is of an interest rather than just few voxels, VBM technique is not adequate to make an informed clinical decision. Hence a novel algorithm DTTA was proposed and evaluated. This algorithm was shown to have the potential to be used in the clinics with routinely used dMRI scans and it is capable of resolving FA for two fibers in the voxels where there is fiber crossing. This new corrected FA can then be used to evaluate the entire tract of interest.

Since DTI can is capable of doing in vivo virtual dissection of the brain, it has tremendous potential to study the developmental patterns of the human brain. It was shown in chapter 3 that most of the fiber tracts responsible for specific function in the adult brain undergo significant developmental changes. It was shown that although the patterns of development derived from clustering algorithms is significantly different at birth than during puberty, remarkably the homologous tracts has similar developmental trend.

In chapter 4, efforts were made to study the perinatal brain development with the aid of graph theoretical methods. Although it is known that during perinatal brain development, several molecular and cellular processes shape the early dynamics of the

structural connectivity; brain network configuration during perinatal brain development is still unknown. It was shown using graph theoretical approaches that during perinatal brain development there is a monotonic increase in all the network derived measurements. However even at very early stages of development, human brain exhibits small-world organization.

But there are still challenges that need to be met to fully utilize the information that can be obtained from dMRI data. Complicated models of tractography to track through the crossing white matter fibers inside the brain in-vivo and validating the tractography techniques with known human brain connections has not been done yet and needs to be done. The diffusion process measured is a macroscopic ensemble of all the microscopic diffusion inside the brain regions and hence the measured white matter fiber integrity is still biased. There is a continuous demand of higher resolution data at a faster speed that will give a complete picture of the structural connectivity of the brain. Combining the information from this highly resolved structural connectivity can further help to answer the ever-staggering question of a very efficient functional brain network.

References

Akaike, H., 1992. [Data analysis by statistical models]. No To Hattatsu 24, 127-133.
Alexander, D.C., 2005. Multiple-fiber reconstruction algorithms for diffusion MRI. Ann N Y Acad Sci 1064, 113-133.
Alexander, D.C., Hubbard, P.L., Hall, M.G., Moore, E.A., Ptito, M., Parker, G.J., Dyrby, T.B., 2010. Orientationally invariant indices of axon diameter and density from diffusion MRI. Neuroimage 52, 1374-1389.
Alexander, M.P., 1995. Mild traumatic brain injury: pathophysiology, natural history, and clinical management. Neurology 45, 1253-1260.
Anderson, A.W., 2005. Measurement of fiber orientation distributions using high angular resolution diffusion imaging. Magn Reson Med 54, 1194-1206.
Assaf, Y., Basser, P.J., 2005. Composite hindered and restricted model of diffusion (CHARMED) MR imaging of the human brain. Neuroimage 27, 48-58.
Assaf, Y., Freidlin, R.Z., Rohde, G.K., Basser, P.J., 2004. New modeling and experimental framework to characterize hindered and restricted water diffusion in brain white matter. Magn Reson Med 52, 965-978.
Axer, H., 2011. Invasive Methods for Tracing White Matter Architecture. Oxford University Press, New York.
Baird, A.E., Benfield, A., Schlaug, G., Siewert, B., Lovblad, K.O., Edelman, R.R., Warach, S., 1997. Enlargement of human cerebral ischemic lesion volumes measured by diffusion-weighted magnetic resonance imaging. Ann Neurol 41, 581-589.
Baird, A.E., Warach, S., 1998. Magnetic resonance imaging of acute stroke. J Cereb Blood Flow Metab 18, 583-609.
Bakshi, R., Minagar, A., Jaisani, Z., Wolinsky, J.S., 2005. Imaging of multiple sclerosis: role in neurotherapeutics. NeuroRx 2, 277-303.
Barnea-Goraly, N., Menon, V., Eckert, M., Tamm, L., Bammer, R., Karchemskiy, A., Dant, C.C., Reiss, A.L., 2005. White matter development during childhood and adolescence: a cross-sectional diffusion tensor imaging study. Cereb Cortex 15, 1848-1854.
Basser, P.J., Mattiello, J., LeBihan, D., 1994a. Estimation of the effective self-diffusion tensor from the NMR spin echo. J Magn Reson B 103, 247-254.
Basser, P.J., Mattiello, J., LeBihan, D., 1994b. MR diffusion tensor spectroscopy and imaging. Biophys J 66, 259-267.
Basser, P.J., Pajevic, S., Pierpaoli, C., Duda, J., Aldroubi, A., 2000. In vivo fiber tractography using DT-MRI data. Magn Reson Med 44, 625-632.
Baumann, N., Pham-Dinh, D., 2001. Biology of oligodendrocyte and myelin in the mammalian central nervous system. Physiol Rev 81, 871-927.
Bayer, S.A., Altman, J., 2005. The Human Brain During the Second Trimester. CRC, Boca Raton, FL.
Beaulieu, C., 2002. The basis of anisotropic water diffusion in the nervous system - a technical review. NMR Biomed 15, 435-455.
Beaulieu, C., Allen, P.S., 1994. Water diffusion in the giant axon of the squid: implications for diffusion-weighted MRI of the nervous system. Magn Reson Med 32, 579-583.
Beaulieu, C., Plewes, C., Paulson, L.A., Roy, D., Snook, L., Concha, L., Phillips, L., 2005. Imaging brain connectivity in children with diverse reading ability. Neuroimage 25, 1266-1271.
Behrens, T.E., Berg, H.J., Jbabdi, S., Rushworth, M.F., Woolrich, M.W., 2007. Probabilistic diffusion tractography with multiple fibre orientations: What can we gain? Neuroimage 34, 144-155.

Benes, F.M., Turtle, M., Khan, Y., Farol, P., 1994. Myelination of a key relay zone in the hippocampal formation occurs in the human brain during childhood, adolescence, and adulthood. Arch Gen Psychiatry 51, 477-484.
Bernstein, M.A., King, K.F., Zhou, X.J., 2004. Handbook of MRI Pulse Sequences. Elsevier Academic Press.
Blinkov, S.M., Glezer, I.I., 1968. The Human Brain in Figures and Tables: A Quantitative Handbook. Plenum Press, New York.
Bonekamp, D., Nagae, L.M., Degaonkar, M., Matson, M., Abdalla, W.M., Barker, P.B., Mori, S., Horska, A., 2007. Diffusion tensor imaging in children and adolescents: reproducibility, hemispheric, and age-related differences. Neuroimage 34, 733-742.
Bullmore, E., Sporns, O., 2009. Complex brain networks: graph theoretical analysis of structural and functional systems. Nat Rev Neurosci 10, 186-198.
Caan, M.W., Khedoe, H.G., Poot, D.H., den Dekker, A.J., Olabarriaga, S.D., Grimbergen, K.A., van Vliet, L.J., Vos, F.M., 2010. Estimation of diffusion properties in crossing fiber bundles. IEEE Trans Med Imaging 29, 1504-1515.
Callaghan, P.T., 2011. Physics of Diffusion. Oxford University Press, New York.
Catani, M., 2011. The Functional Anatomy of White Matter: From Postmortem Dissections to In Vivo Virtual Tractography. Oxford University Press, New York.
Catani, M., Howard, R.J., Pajevic, S., Jones, D.K., 2002. Virtual in vivo interactive dissection of white matter fasciculi in the human brain. Neuroimage 17, 77-94.
Chi, J.G., Dooling, E.C., Gilles, F.H., 1977. Gyral development of the human brain. Ann Neurol 1, 86-93.
Choi, S.J., Lim, K.O., Monteiro, I., Reisberg, B., 2005. Diffusion tensor imaging of frontal white matter microstructure in early Alzheimer's disease: a preliminary study. J Geriatr Psychiatry Neurol 18, 12-19.
Chugani, H.T., Phelps, M.E., Mazziotta, J.C., 1987. Positron emission tomography study of human brain functional development. Ann Neurol 22, 487-497.
Ciccarelli, O., Catani, M., Johansen-Berg, H., Clark, C., Thompson, A., 2008. Diffusion-based tractography in neurological disorders: concepts, applications, and future developments. Lancet Neurol 7, 715-727.
Colby, J.B., Soderberg, L., Lebel, C., Dinov, I.D., Thompson, P.M., Sowell, E.R., 2012. Along-tract statistics allow for enhanced tractography analysis. Neuroimage 59, 3227-3242.
Conturo, T.E., Lori, N.F., Cull, T.S., Akbudak, E., Snyder, A.Z., Shimony, J.S., McKinstry, R.C., Burton, H., Raichle, M.E., 1999. Tracking neuronal fiber pathways in the living human brain. Proc Natl Acad Sci U S A 96, 10422-10427.
Cummings, J.L., 2004. Alzheimer's disease. New England Journal of Medicine, 56.
Delgado-Ayala, M., Smith, L., Clegg, N., Huang, H., 2012. White matter biomarker of hereditary spastic paraplegia. Annals of Neurology 72, s196-s197.
Dell'acqua, F., Simmons, A., Williams, S.C., Catani, M., 2013. Can spherical deconvolution provide more information than fiber orientations? Hindrance modulated orientational anisotropy, a true-tract specific index to characterize white matter diffusion. Hum Brain Mapp 34, 2464-2483.
Dennis, E.L., Jahanshad, N., Rudie, J.D., Brown, J.A., Johnson, K., McMahon, K.L., de Zubicaray, G.I., Montgomery, G., Martin, N.G., Wright, M.J., Bookheimer, S.Y., Dapretto, M., Toga, A.W., Thompson, P.M., 2011. Altered structural brain connectivity in healthy carriers of the autism risk gene, CNTNAP2. Brain Connect 1, 447-459.
Doria, V., Beckmann, C.F., Arichi, T., Merchant, N., Groppo, M., Turkheimer, F.E., Counsell, S.J., Murgasova, M., Aljabar, P., Nunes, R.G., Larkman, D.J., Rees, G.,

Edwards, A.D., 2010. Emergence of resting state networks in the preterm human brain. Proc Natl Acad Sci U S A 107, 20015-20020.
Dosenbach, N.U., Nardos, B., Cohen, A.L., Fair, D.A., Power, J.D., Church, J.A., Nelson, S.M., Wig, G.S., Vogel, A.C., Lessov-Schlaggar, C.N., Barnes, K.A., Dubis, J.W., Feczko, E., Coalson, R.S., Pruett, J.R., Jr., Barch, D.M., Petersen, S.E., Schlaggar, B.L., 2010. Prediction of individual brain maturity using fMRI. Science 329, 1358-1361.
Douaud, G., Jbabdi, S., Behrens, T.E., Menke, R.A., Gass, A., Monsch, A.U., Rao, A., Whitcher, B., Kindlmann, G., Matthews, P.M., Smith, S., 2011. DTI measures in crossing-fibre areas: increased diffusion anisotropy reveals early white matter alteration in MCI and mild Alzheimer's disease. Neuroimage 55, 880-890.
Dubois, J., Dehaene-Lambertz, G., Perrin, M., Mangin, J.F., Cointepas, Y., Duchesnay, E., Le Bihan, D., Hertz-Pannier, L., 2008. Asynchrony of the early maturation of white matter bundles in healthy infants: quantitative landmarks revealed noninvasively by diffusion tensor imaging. Hum Brain Mapp 29, 14-27.
Eluvathingal, T.J., Hasan, K.M., Kramer, L., Fletcher, J.M., Ewing-Cobbs, L., 2007. Quantitative diffusion tensor tractography of association and projection fibers in normally developing children and adolescents. Cereb Cortex 17, 2760-2768.
Ennis, D.B., Kindlmann, G., 2006. Orthogonal tensor invariants and the analysis of diffusion tensor magnetic resonance images. Magn Reson Med 55, 136-146.
Euler, L., 1736. Solutio problematis ad geometriam situs pertinentis. Commentarii Academiae Scientiarum Imperialis Petropolitanae, 128-140.
Evans, M.J., Finean, J.B., 1965. The Lipid Composition of Myelin from Brain and Peripheral Nerve. J Neurochemistry 12, 6.
Fair, D.A., Cohen, A.L., Dosenbach, N.U., Church, J.A., Miezin, F.M., Barch, D.M., Raichle, M.E., Petersen, S.E., Schlaggar, B.L., 2008. The maturing architecture of the brain's default network. Proc Natl Acad Sci U S A 105, 4028-4032.
Fair, D.A., Dosenbach, N.U., Church, J.A., Cohen, A.L., Brahmbhatt, S., Miezin, F.M., Barch, D.M., Raichle, M.E., Petersen, S.E., Schlaggar, B.L., 2007. Development of distinct control networks through segregation and integration. Proc Natl Acad Sci U S A 104, 13507-13512.
Fick, A., 1855. Uber diffusion. Philosphical Magazine.
Fields, D., 2008. White Matter. Scientific American 298, 8.
Filippi, M., Cercignani, M., Inglese, M., Horsfield, M.A., Comi, G., 2001. Diffusion tensor magnetic resonance imaging in multiple sclerosis. Neurology 56, 304-311.
Filley, C.M., 2001. The Behavioral Neurology of white matter. Oxford University Press, New York.
Filley, C.M., 2011. Neurobiology of White Matter Disorders. Oxford University Press, New York.
Filley, C.M., Franklin, G.M., Heaton, R.K., Rosenberg, N.L., 1988. White matter dementia. Clinical disorders and implications. Neuropsychiatry Neuropsychol Behav Neurol, 119-125.
Filley, C.M., Kleinschmidt-DeMasters, B.K., 2001. Toxic leukoencephalopathy. N Engl J Med 345, 425-432.
Fisher, R.A., 1915. Frequency distribution of the values of the correlation coefficient in samples of an infinitely large population. Biometrika, 507-521.
Fransson, P., Skiold, B., Horsch, S., Nordell, A., Blennow, M., Lagercrantz, H., Aden, U., 2007. Resting-state networks in the infant brain. Proc Natl Acad Sci U S A 104, 15531-15536.

Fritzsche, K.H., Laun, F.B., Meinzer, H.P., Stieltjes, B., 2010. Opportunities and pitfalls in the quantification of fiber integrity: what can we gain from Q-ball imaging? Neuroimage 51, 242-251.
Gao, W., Lin, W., Chen, Y., Gerig, G., Smith, J.K., Jewells, V., Gilmore, J.H., 2009a. Temporal and spatial development of axonal maturation and myelination of white matter in the developing brain. AJNR Am J Neuroradiol 30, 290-296.
Gao, W., Zhu, H., Giovanello, K.S., Smith, J.K., Shen, D., Gilmore, J.H., Lin, W., 2009b. Evidence on the emergence of the brain's default network from 2-week-old to 2-year-old healthy pediatric subjects. Proc Natl Acad Sci U S A 106, 6790-6795.
Garde, E., Lykke Mortensen, E., Rostrup, E., Paulson, O.B., 2005. Decline in intelligence is associated with progression in white matter hyperintensity volume. J Neurol Neurosurg Psychiatry 76, 1289-1291.
Giedd, J.N., Blumenthal, J., Jeffries, N.O., Castellanos, F.X., Liu, H., Zijdenbos, A., Paus, T., Evans, A.C., Rapoport, J.L., 1999. Brain development during childhood and adolescence: a longitudinal MRI study. Nat Neurosci 2, 861-863.
Giorgio, A., Santelli, L., Tomassini, V., Bosnell, R., Smith, S., De Stefano, N., Johansen-Berg, H., 2010. Age-related changes in grey and white matter structure throughout adulthood. Neuroimage 51, 943-951.
Goebell, E., Paustenbach, S., Vaeterlein, O., Ding, X.Q., Heese, O., Fiehler, J., Kucinski, T., Hagel, C., Westphal, M., Zeumer, H., 2006. Low-grade and anaplastic gliomas: differences in architecture evaluated with diffusion-tensor MR imaging. Radiology 239, 217-222.
Gong, G., Jiang, T., Zhu, C., Zang, Y., Wang, F., Xie, S., Xiao, J., Guo, X., 2005. Asymmetry analysis of cingulum based on scale-invariant parameterization by diffusion tensor imaging. Hum Brain Mapp 24, 92-98.
Gong, G., Rosa-Neto, P., Carbonell, F., Chen, Z.J., He, Y., Evans, A.C., 2009. Age- and gender-related differences in the cortical anatomical network. J Neurosci 29, 15684-15693.
Goodlett, C.B., Fletcher, P.T., Gilmore, J.H., Gerig, G., 2009. Group analysis of DTI fiber tract statistics with application to neurodevelopment. Neuroimage 45, S133-142.
Greicius, M.D., Supekar, K., Menon, V., Dougherty, R.F., 2009. Resting-state functional connectivity reflects structural connectivity in the default mode network. Cereb Cortex 19, 72-78.
Hagmann, P., Sporns, O., Madan, N., Cammoun, L., Pienaar, R., Wedeen, V.J., Meuli, R., Thiran, J.P., Grant, P.E., 2010. White matter maturation reshapes structural connectivity in the late developing human brain. Proc Natl Acad Sci U S A 107, 19067-19072.
Hahn, K., Prigarin, S., Hasan, K.M., 2013. Fitting of two-tensor models without ad hoc assumptions to detect crossing fibers using clinical DWI data. Magn Reson Imaging 31, 585-595.
He, Y., Chen, Z.J., Evans, A.C., 2007. Small-world anatomical networks in the human brain revealed by cortical thickness from MRI. Cereb Cortex 17, 2407-2419.
He, Y., Evans, A., 2010. Graph theoretical modeling of brain connectivity. Curr Opin Neurol 23, 341-350.
Helton, K.J., Phillips, N.S., Khan, R.B., Boop, F.A., Sanford, R.A., Zou, P., Li, C.S., Langston, J.W., Ogg, R.J., 2006. Diffusion tensor imaging of tract involvement in children with pontine tumors. AJNR Am J Neuroradiol 27, 786-793.
Hermoye, L., Saint-Martin, C., Cosnard, G., Lee, S.K., Kim, J., Nassogne, M.C., Menten, R., Clapuyt, P., Donohue, P.K., Hua, K., Wakana, S., Jiang, H., van Zijl, P.C., Mori, S.,

2006. Pediatric diffusion tensor imaging: normal database and observation of the white matter maturation in early childhood. Neuroimage 29, 493-504.
Honey, C.J., Sporns, O., Cammoun, L., Gigandet, X., Thiran, J.P., Meuli, R., Hagmann, P., 2009. Predicting human resting-state functional connectivity from structural connectivity. Proc Natl Acad Sci U S A 106, 2035-2040.
Horsfield, M.A., Jones, D.K., 2002. Applications of diffusion-weighted and diffusion tensor MRI to white matter diseases - a review. NMR Biomed 15, 570-577.
Hosey, T., Williams, G., Ansorge, R., 2005. Inference of multiple fiber orientations in high angular resolution diffusion imaging. Magn Reson Med 54, 1480-1489.
Hosey, T.P., Harding, S.G., Carpenter, T.A., Ansorge, R.E., Williams, G.B., 2008. Application of a probabilistic double-fibre structure model to diffusion-weighted MR images of the human brain. Magn Reson Imaging 26, 236-245.
Huang, H., Fan, X., Weiner, M., Martin-Cook, K., Xiao, G., Davis, J., Devous, M., Rosenberg, R., Diaz-Arrastia, R., 2012a. Distinctive disruption patterns of white matter tracts in Alzheimer's disease with full diffusion tensor characterization. Neurobiol Aging 33, 2029-2045.
Huang, H., Fan, X., Williamson, D.E., Rao, U., 2011. White matter changes in healthy adolescents at familial risk for unipolar depression: a diffusion tensor imaging study. Neuropsychopharmacology 36, 684-691.
Huang, H., Gundapuneedi, T., Rao, U., 2012b. White matter disruptions in adolescents exposed to childhood maltreatment and vulnerability to psychopathology. Neuropsychopharmacology 37, 2693-2701.
Huang, H., Shu, N., Mishra, V., Jeon, T., Chalak, L., Wang, Z.J., Rollins, N., Gong, G., Cheng, H., Peng, Y., Dong, Q., He, Y., 2013. Development of Human Brain Structural Networks Through Infancy and Childhood. Cereb Cortex.
Huang, H., Vasung, L., 2013. Gaining insight of fetal brain development with diffusion MRI and histology. Int J Dev Neurosci.
Huang, H., Xue, R., Zhang, J., Ren, T., Richards, L.J., Yarowsky, P., Miller, M.I., Mori, S., 2009. Anatomical characterization of human fetal brain development with diffusion tensor magnetic resonance imaging. J Neurosci 29, 4263-4273.
Huang, H., Zhang, J., Wakana, S., Zhang, W., Ren, T., Richards, L.J., Yarowsky, P., Donohue, P., Graham, E., van Zijl, P.C., Mori, S., 2006. White and gray matter development in human fetal, newborn and pediatric brains. Neuroimage 33, 27-38.
Huppi, P., 2011. Diffusion Tensor MRI in brain development. Oxford University Press, New York.
Huppi, P.S., Dubois, J., 2006. Diffusion tensor imaging of brain development. Semin Fetal Neonatal Med 11, 489-497.
Huppi, P.S., Maier, S.E., Peled, S., Zientara, G.P., Barnes, P.D., Jolesz, F.A., Volpe, J.J., 1998. Microstructural development of human newborn cerebral white matter assessed in vivo by diffusion tensor magnetic resonance imaging. Pediatr Res 44, 584-590.
Huttenlocher, P.R., de Courten, C., Garey, L.J., Van der Loos, H., 1982. Synaptogenesis in human visual cortex--evidence for synapse elimination during normal development. Neurosci Lett 33, 247-252.
Huxley, A.F., Stampfli, R., 1949. Evidence for saltatory conduction in peripheral myelinated nerve fibers. J Physiol 108, 315-339.
Jbabdi, S., Behrens, T.E., Smith, S.M., 2010. Crossing fibres in tract-based spatial statistics. Neuroimage 49, 249-256.
Jensen, J.H., Helpern, J.A., Ramani, A., Lu, H., Kaczynski, K., 2005. Diffusional kurtosis imaging: the quantification of non-gaussian water diffusion by means of magnetic resonance imaging. Magn Reson Med 53, 1432-1440.

Jeon, T., Mishra, V., Uh, J., Weiner, M., Hatanpaa, K.J., White, C.L., Zhao, Y.D., Lu, H., Diaz-Arrastia, R., Huang, H., 2012. Regional Changes of Cortical Mean Diffusivities with Aging after correction of Partial Volume Effects. Neuroimage, 1705-1716
Jeurissen, B., Leemans, A., Tournier, J.D., Jones, D.K., Sijbers, J., 2012. Investigating the prevalence of complex fiber configurations in white matter tissue with diffusion magnetic resonance imaging. Hum Brain Mapp.
Jiang, H., van Zijl, P.C., Kim, J., Pearlson, G.D., Mori, S., 2006. DtiStudio: resource program for diffusion tensor computation and fiber bundle tracking. Comput Methods Programs Biomed 81, 106-116.
Jones, D.K., Horsfield, M.A., Simmons, A., 1999a. Optimal strategies for measuring diffusion in anisotropic systems by magnetic resonance imaging. Magn Reson Med 42, 515-525.
Jones, D.K., Simmons, A., Williams, S.C., Horsfield, M.A., 1999b. Non-invasive assessment of axonal fiber connectivity in the human brain via diffusion tensor MRI. Magn Reson Med 42, 37-41.
Judas, M., 2011. Perinatal development of the human fetal telencephalon. Springer-Verlag, Berlin Heidleberg.
Klingberg, T., Hedehus, M., Temple, E., Salz, T., Gabrieli, J.D., Moseley, M.E., Poldrack, R.A., 2000. Microstructure of temporo-parietal white matter as a basis for reading ability: evidence from diffusion tensor magnetic resonance imaging. Neuron 25, 493-500.
Kostovic, I., Jovanov-Milosevic, N., 2006. The development of cerebral connections during the first 20-45 weeks' gestation. Semin Fetal Neonatal Med 11, 415-422.
Latora, V., Marchiori, M., 2001. Efficient behavior of small-world networks. Phys Rev Lett 87, 198701.
Lazar, M., Alexander, A.L., 2005. Bootstrap white matter tractography (BOOT-TRAC). Neuroimage 24, 524-532.
Lazar, M., Weinstein, D.M., Tsuruda, J.S., Hasan, K.M., Arfanakis, K., Meyerand, M.E., Badie, B., Rowley, H.A., Haughton, V., Field, A., Alexander, A.L., 2003. White matter tractography using diffusion tensor deflection. Hum Brain Mapp 18, 306-321.
Le Bihan, D., 2011. Magnetic Resonance Diffusion Imaging: Introduction and Concepts. Oxford University Press, New York
Lebel, C., Walker, L., Leemans, A., Phillips, L., Beaulieu, C., 2008. Microstructural maturation of the human brain from childhood to adulthood. Neuroimage 40, 1044-1055.
Li, Y.O., Yang, F.G., Nguyen, C.T., Cooper, S.R., LaHue, S.C., Venugopal, S., Mukherjee, P., 2012. Independent component analysis of DTI reveals multivariate microstructural correlations of white matter in the human brain. Hum Brain Mapp 33, 1431-1451.
Li, Z., Moore, A.B., Tyner, C., Hu, X., 2009. Asymmetric connectivity reduction and its relationship to "HAROLD" in aging brain. Brain Res 1295, 149-158.
Liu, C., Bammer, R., Acar, B., Moseley, M.E., 2004. Characterizing non-Gaussian diffusion by using generalized diffusion tensors. Magn Reson Med 51, 924-937.
Liu, Y., Duan, Y., He, Y., Wang, J., Xia, M., Yu, C., Dong, H., Ye, J., Butzkueven, H., Li, K., Shu, N., 2012. Altered Topological Organization of White Matter Structural Networks in Patients with Neuromyelitis Optica. PLoS One.
Marner, L., Nyengaard, J.R., Tang, Y., Pakkenberg, B., 2003. Marked loss of myelinated nerve fibers in the human brain with age. J Comp Neurol 462, 144-152.
Martino, J., Brogna, C., Robles, S.G., Vergani, F., Duffau, H., 2010. Anatomic dissection of the inferior fronto-occipital fasciculus revisited in the lights of brain stimulation data. Cortex 46, 691-699.

Maslov, S., Sneppen, K., 2002. Specificity and stability in topology of protein networks. Science 296, 910-913.
Minati, L., Aquino, D., Rampoldi, S., Papa, S., Grisoli, M., Bruzzone, M.G., Maccagnano, E., 2007. Biexponential and diffusional kurtosis imaging, and generalised diffusion-tensor imaging (GDTI) with rank-4 tensors: a study in a group of healthy subjects. MAGMA 20, 241-253.
Minati, L., Banasik, T., Brzezinski, J., Mandelli, M.L., Bizzi, A., Bruzzone, M.G., Konopka, M., Jasinski, A., 2008. Elevating tensor rank increases anisotropy in brain areas associated with intra-voxel orientational heterogeneity (IVOH): a generalised DTI (GDTI) study. NMR Biomed 21, 2-14.
Mishra, V., Huang, H., 2010. Effects of noise and resolution on fiber count and fiber volume of DTI tractography. ISMRM, Stockholm, Sweden.
Mori, S., 2007. Introduction to Diffusion Tensor Imaging, 1 ed. Elsevier, Italy.
Mori, S., Crain, B.J., Chacko, V.P., van Zijl, P.C., 1999. Three-dimensional tracking of axonal projections in the brain by magnetic resonance imaging. Ann Neurol 45, 265-269.
Mukherjee, P., Miller, J.H., Shimony, J.S., Philip, J.V., Nehra, D., Snyder, A.Z., Conturo, T.E., Neil, J.J., McKinstry, R.C., 2002. Diffusion-tensor MR imaging of gray and white matter development during normal human brain maturation. AJNR Am J Neuroradiol 23, 1445-1456.
Neil, J., Miller, J., Mukherjee, P., Huppi, P.S., 2002. Diffusion tensor imaging of normal and injured developing human brain - a technical review. NMR Biomed 15, 543-552.
Niogi, S.N., Mukherjee, P., Ghajar, J., Johnson, C.E., Kolster, R., Lee, H., Suh, M., Zimmerman, R.D., Manley, G.T., McCandliss, B.D., 2008. Structural dissociation of attentional control and memory in adults with and without mild traumatic brain injury. Brain 131, 3209-3221.
Nolte, J., 1999. The Human Brain: An Introduction to its functional anatomy, 5 ed. Mosby, St. Loius.
O'Donnell, L.J., Westin, C.F., Golby, A.J., 2009. Tract-based morphometry for white matter group analysis. Neuroimage 45, 832-844.
O'Rahilly, R., Muller, F., 2006. Embryonic Human Brain: An Atlas of Developmental Stages. John Wiley & Sons, Inc, Hoboken, NJ.
Oishi, K., Mori, S., Donohue, P.K., Ernst, T., Anderson, L., Buchthal, S., Faria, A., Jiang, H., Li, X., Miller, M.I., van Zijl, P.C., Chang, L., 2011. Multi-contrast human neonatal brain atlas: application to normal neonate development analysis. Neuroimage 56, 8-20.
Ozarslan, E., Vemuri, B.C., Mareci, T.H., 2005. Generalized scalar measures for diffusion MRI using trace, variance, and entropy. Magn Reson Med 53, 866-876.
Parker, G.J., Wheeler-Kingshott, C.A., Barker, G.J., 2002. Estimating distributed anatomical connectivity using fast marching methods and diffusion tensor imaging. IEEE Trans Med Imaging 21, 505-512.
Pasternak, O., Sochen, N., Gur, Y., Intrator, N., Assaf, Y., 2009. Free water elimination and mapping from diffusion MRI. Magn Reson Med 62, 717-730.
Paus, T., Zijdenbos, A., Worsley, K., Collins, D.L., Blumenthal, J., Giedd, J.N., Rapoport, J.L., Evans, A.C., 1999. Structural maturation of neural pathways in children and adolescents: in vivo study. Science 283, 1908-1911.
Peled, S., Friman, O., Jolesz, F., Westin, C.F., 2006. Geometrically constrained two-tensor model for crossing tracts in DWI. Magn Reson Imaging 24, 1263-1270.
Pierpaoli, C., Basser, P.J., 1996. Toward a quantitative assessment of diffusion anisotropy. Magn Reson Med 36, 893-906.
Poliakov, G.I., 1949. Structural organization of the human cerebral cortex during ontogenetic development. Medgiz, Moscow.

Powell, H.W., Parker, G.J., Alexander, D.C., Symms, M.R., Boulby, P.A., Wheeler-Kingshott, C.A., Barker, G.J., Noppeney, U., Koepp, M.J., Duncan, J.S., 2006. Hemispheric asymmetries in language-related pathways: a combined functional MRI and tractography study. Neuroimage 32, 388-399.
Power, J.D., Fair, D.A., Schlaggar, B.L., Petersen, S.E., 2010. The development of human functional brain networks. Neuron 67, 735-748.
Rafii, M.S., Aisen, P.S., 2009. Recent developments in Alzheimer's disease. Biomed Central.
Rakic, P., 1988. Specification of cerebral cortical areas. Science 241, 170-176.
Ramirez-Manzanares, A., Cook, P.A., Hall, M., Ashtari, M., Gee, J.C., 2011. Resolving axon fiber crossings at clinical b-values: an evaluation study. Med Phys 38, 5239-5253.
Reed, B.R., Eberling, J.L., Mungas, D., Weiner, M., Kramer, J.H., Jagust, W.J., 2004. Effects of white matter lesions and lacunes on cortical function. Arch Neurol 61, 1545-1550.
Rencher, A.C., 2002. Methods of Multivariate Analysis, 2 ed. Wiley Interscience, Hoboken N.J.
Rodrigo, S., Naggara, O., Oppenheim, C., Golestani, N., Poupon, C., Cointepas, Y., Mangin, J.F., Le Bihan, D., Meder, J.F., 2007. Human subinsular asymmetry studied by diffusion tensor imaging and fiber tracking. AJNR Am J Neuroradiol 28, 1526-1531.
Rovaris, M., Bozzali, M., Iannucci, G., Ghezzi, A., Caputo, D., Montanari, E., Bertolotto, A., Bergamaschi, R., Capra, R., Mancardi, G.L., Martinelli, V., Comi, G., Filippi, M., 2002. Assessment of normal-appearing white and gray matter in patients with primary progressive multiple sclerosis: a diffusion-tensor magnetic resonance imaging study. Arch Neurol 59, 1406-1412.
Rubinov, M., Sporns, O., 2010. Complex network measures of brain connectivity: uses and interpretations. Neuroimage 52, 1059-1069.
Salat, D.H., Kaye, J.A., Janowsky, J.S., 1999. Prefrontal gray and white matter volumes in healthy aging and Alzheimer disease. Arch Neurol 56, 338-344.
Salat, D.H., Tuch, D.S., Greve, D.N., van der Kouwe, A.J., Hevelone, N.D., Zaleta, A.K., Rosen, B.R., Fischl, B., Corkin, S., Rosas, H.D., Dale, A.M., 2005. Age-related alterations in white matter microstructure measured by diffusion tensor imaging. Neurobiol Aging 26, 1215-1227.
Saxena, K., Tamm, L., Walley, A., Simmons, A., Rollins, N., Chia, J., Soares, J.C., Emslie, G.J., Fan, X., Huang, H., 2012. A preliminary investigation of corpus callosum and anterior commissure aberrations in aggressive youth with bipolar disorders. J Child Adolesc Psychopharmacol 22, 112-119.
Schmithorst, V.J., Yuan, W., 2010. White matter development during adolescence as shown by diffusion MRI. Brain Cogn 72, 16-25.
Schwamm, L.H., Koroshetz, W.J., Sorensen, A.G., Wang, B., Copen, W.A., Budzik, R., Rordorf, G., Buonanno, F.S., Schaefer, P.W., Gonzalez, R.G., 1998. Time course of lesion development in patients with acute stroke: serial diffusion- and hemodynamic-weighted magnetic resonance imaging. Stroke 29, 2268-2276.
Schwartz, E.D., Cooper, E.T., Fan, Y., Jawad, A.F., Chin, C.L., Nissanov, J., Hackney, D.B., 2005. MRI diffusion coefficients in spinal cord correlate with axon morphometry. Neuroreport 16, 73-76.
Shimodaira, H., 2002. An approximately unbiased test of phylogenetic tree selection. Systems Biology, 492-508.
Shimodaira, H., 2004. Approximately unbiased tests of regions using multistep-multiscale bootstrap resampling. Annals of Statistics, 2616-2641.

Sidman, R.L., Rakic, P., 1982. Development of the human central nervous system. Thomas, C.C., Springfield, IL.
Smith, S.M., Jenkinson, M., Johansen-Berg, H., Rueckert, D., Nichols, T.E., Mackay, C.E., Watkins, K.E., Ciccarelli, O., Cader, M.Z., Matthews, P.M., Behrens, T.E., 2006. Tract-based spatial statistics: voxelwise analysis of multi-subject diffusion data. Neuroimage 31, 1487-1505.
Snook, L., Paulson, L.A., Roy, D., Phillips, L., Beaulieu, C., 2005. Diffusion tensor imaging of neurodevelopment in children and young adults. Neuroimage 26, 1164-1173.
Song, S.K., Sun, S.W., Ramsbottom, M.J., Chang, C., Russell, J., Cross, A.H., 2002. Dysmyelination revealed through MRI as increased radial (but unchanged axial) diffusion of water. Neuroimage 17, 1429-1436.
Sotiropoulos, S.N., Bai, L., Morgan, P.S., Auer, D.P., Constantinescu, C.S., Tench, C.R., 2008. A regularized two-tensor model fit to low angular resolution diffusion images using basis directions. J Magn Reson Imaging 28, 199-209.
Stampfli, P., 2007. Resolving the neuronal architecture of the human brain by diffusion tensor imaging and fiber tractography. PhD dissertation, Swiss Federal Institute of Technology, Zurich, Diss. ETH no 17194.
Stejskal, E.O., Tanner, J.E., 1956. Spin diffusion measurement: Spin echoes in the presence of a time-dependent field gradient. Journal of Chemical Physics, 288-292.
Stieltjes, B., Kaufmann, W.E., van Zijl, P.C., Fredericksen, K., Pearlson, G.D., Solaiyappan, M., Mori, S., 2001. Diffusion tensor imaging and axonal tracking in the human brainstem. Neuroimage 14, 723-735.
Studholme, C., 2011. Mapping fetal brain development in utero using magnetic resonance imaging: the Big Bang of brain mapping. Annu Rev Biomed Eng 13, 345-368.
Supekar, K., Musen, M., Menon, V., 2009. Development of large-scale functional brain networks in children. PLoS Biol 7, e1000157.
Suzuki, R., Shimodaira, H., 2006. Pvclust: an R package for assessing the uncertainty in hierarchical clustering. Bioinformatics 22, 1540-1542.
Swanberg, M.M., Tractenberg, R.E., Mohs, R., Thal, L.J., Cummings, J.L., 2004. Executive dysfunction in Alzheimer disease. Arch Neurol 61, 556-560.
Takahashi, E., Folkerth, R.D., Galaburda, A.M., Grant, P.E., 2012. Emerging cerebral connectivity in the human fetal brain: an MR tractography study. Cereb Cortex 22, 455-464.
Tamnes, C.K., Ostby, Y., Fjell, A.M., Westlye, L.T., Due-Tonnessen, P., Walhovd, K.B., 2010. Brain maturation in adolescence and young adulthood: regional age-related changes in cortical thickness and white matter volume and microstructure. Cereb Cortex 20, 534-548.
Tang, Y., Nyengaard, J.R., Pakkenberg, B., Gundersen, H.J., 1997. Age-induced white matter changes in the human brain: a stereological investigation. Neurobiol Aging 18, 609-615.
Tiedemann, F., 1816. Anatomie und Bildungsgeschichte des Gehirns im Foetus des menschen. Steinische Buchhandlung, Nuremberg.
Tievsky, A.L., Ptak, T., Farkas, J., 1999. Investigation of apparent diffusion coefficient and diffusion tensor anisotrophy in acute and chronic multiple sclerosis lesions. AJNR Am J Neuroradiol 20, 1491-1499.
Tofts, P., 2003. Quantitative MRI of the Brain. Wiley, New York.
Tournier, J.D., 2011. The biophysics of crossing fibers. Oxford University Press, New York.

Tournier, J.D., Calamante, F., Gadian, D.G., Connelly, A., 2004. Direct estimation of the fiber orientation density function from diffusion-weighted MRI data using spherical deconvolution. Neuroimage 23, 1176-1185.
Tuch, D.S., 2004. Q-ball imaging. Magn Reson Med 52, 1358-1372.
Tuch, D.S., Salat, D.H., Wisco, J.J., Zaleta, A.K., Hevelone, N.D., Rosas, H.D., 2005. Choice reaction time performance correlates with diffusion anisotropy in white matter pathways supporting visuospatial attention. Proc Natl Acad Sci U S A 102, 12212-12217.
Tullberg, M., Fletcher, E., DeCarli, C., Mungas, D., Reed, B.R., Harvey, D.J., Weiner, M.W., Chui, H.C., Jagust, W.J., 2004. White matter lesions impair frontal lobe function regardless of their location. Neurology 63, 246-253.
van den Heuvel, M.P., Mandl, R.C., Kahn, R.S., Hulshoff Pol, H.E., 2009. Functionally linked resting-state networks reflect the underlying structural connectivity architecture of the human brain. Hum Brain Mapp 30, 3127-3141.
van den Heuvel, M.P., Sporns, O., 2011. Rich-club organization of the human connectome. J Neurosci 31, 15775-15786.
van Dijk, E.J., Prins, N.D., Vrooman, H.A., Hofman, A., Koudstaal, P.J., Breteler, M.M., 2008. Progression of cerebral small vessel disease in relation to risk factors and cognitive consequences: Rotterdam Scan study. Stroke 39, 2712-2719.
Vasung, L., Huang, H., Jovanov-Milosevic, N., Pletikos, M., Mori, S., Kostovic, I., 2010. Development of axonal pathways in the human fetal fronto-limbic brain: histochemical characterization and diffusion tensor imaging. J Anat 217, 400-417.
Vasung, L., Jovanov-Milosevic, N., Pletikos, M., Mori, S., Judas, M., Kostovic, I., 2011. Prominent periventricular fiber system related to ganglionic eminence and striatum in the human fetal cerebrum. Brain Struct Funct 215, 237-253.
Volpe, J.J., 2001. Neurobiology of periventricular leukomalacia in the premature infant. Pediatr Res 50, 553-562.
Wahl, M., Li, Y.O., Ng, J., Lahue, S.C., Cooper, S.R., Sherr, E.H., Mukherjee, P., 2010. Microstructural correlations of white matter tracts in the human brain. Neuroimage 51, 531-541.
Wakana, S., Caprihan, A., Panzenboeck, M.M., Fallon, J.H., Perry, M., Gollub, R.L., Hua, K., Zhang, J., Jiang, H., Dubey, P., Blitz, A., van Zijl, P., Mori, S., 2007. Reproducibility of quantitative tractography methods applied to cerebral white matter. Neuroimage 36, 630-644.
Wakana, S., Jiang, H., Nagae-Poetscher, L.M., van Zijl, P.C., Mori, S., 2004. Fiber tract-based atlas of human white matter anatomy. Radiology 230, 77-87.
Wang, R., Benner, T., Sorensen, A.G., Wedeen, V.J., 2007. Diffusion Toolkit: A Software Package for Diffusion Imaging Data Processing and Tractography. ISMRM, Berlin, Germany.
Watts, D.J., Strogatz, S.H., 1998. Collective dynamics of 'small-world' networks. Nature 393, 440-442.
Wedeen, V.J., Hagmann, P., Tseng, W.Y., Reese, T.G., Weisskoff, R.M., 2005. Mapping complex tissue architecture with diffusion spectrum magnetic resonance imaging. Magn Reson Med 54, 1377-1386.
Wen, H.M., Mok, V.C., Fan, Y.H., Lam, W.W., Tang, W.K., Wong, A., Huang, R.X., Wong, K.S., 2004. Effect of white matter changes on cognitive impairment in patients with lacunar infarcts. Stroke 35, 1826-1830.
Westlye, L.T., Walhovd, K.B., Dale, A.M., Bjornerud, A., Due-Tonnessen, P., Engvig, A., Grydeland, H., Tamnes, C.K., Ostby, Y., Fjell, A.M., 2010. Life-span changes of the human brain white matter: diffusion tensor imaging (DTI) and volumetry. Cereb Cortex 20, 2055-2068.

Wheeler-Kingshott, C.A., Cercignani, M., 2009. About "axial" and "radial" diffusivities. Magn Reson Med 61, 1255-1260.
Wilde, E.A., McCauley, S.R., Chu, Z., Hunter, J.V., Bigler, E.D., Yallampalli, R., Wang, Z.J., Hanten, G., Li, X., Ramos, M.A., Sabir, S.H., Vasquez, A.C., Menefee, D., Levin, H.S., 2009. Diffusion tensor imaging of hemispheric asymmetries in the developing brain. J Clin Exp Neuropsychol 31, 205-218.
Witwer, B.P., Moftakhar, R., Hasan, K.M., Deshmukh, P., Haughton, V., Field, A., Arfanakis, K., Noyes, J., Moritz, C.H., Meyerand, M.E., Rowley, H.A., Alexander, A.L., Badie, B., 2002. Diffusion-tensor imaging of white matter tracts in patients with cerebral neoplasm. J Neurosurg 97, 568-575.
Woods, R.P., Grafton, S.T., Holmes, C.J., Cherry, S.R., Mazziotta, J.C., 1998. Automated image registration: I. General methods and intrasubject, intramodality validation. J Comput Assist Tomogr 22, 139-152.
Wozniak, J.R., Lim, K.O., 2006. Advances in white matter imaging: a review of in vivo magnetic resonance methodologies and their applicability to the study of development and aging. Neurosci Biobehav Rev 30, 762-774.
Wu, O., Koroshetz, W.J., Ostergaard, L., Buonanno, F.S., Copen, W.A., Gonzalez, R.G., Rordorf, G., Rosen, B.R., Schwamm, L.H., Weisskoff, R.M., Sorensen, A.G., 2001. Predicting tissue outcome in acute human cerebral ischemia using combined diffusion- and perfusion-weighted MR imaging. Stroke 32, 933-942.
Yap, P.T., Fan, Y., Chen, Y., Gilmore, J.H., Lin, W., Shen, D., 2011. Development trends of white matter connectivity in the first years of life. PLoS One 6, e24678.
Yushkevich, P.A., Zhang, H., Simon, T.J., Gee, J.C., 2008. Structure-specific statistical mapping of white matter tracts. Neuroimage 41, 448-461.
Zalesky, A., Fornito, A., Harding, I.H., Cocchi, L., Yucel, M., Pantelis, C., Bullmore, E.T., 2010. Whole-brain anatomical networks: does the choice of nodes matter? Neuroimage 50, 970-983.
Zhan, L., Leow, A.D., Jahanshad, N., Chiang, M.C., Barysheva, M., Lee, A.D., Toga, A.W., McMahon, K.L., de Zubicaray, G.I., Wright, M.J., Thompson, P.M., 2010. How does angular resolution affect diffusion imaging measures? Neuroimage 49, 1357-1371.
Zhang, H., Schneider, T., Wheeler-Kingshott, C.A., Alexander, D.C., 2012. NODDI: practical in vivo neurite orientation dispersion and density imaging of the human brain. Neuroimage 61, 1000-1016.
Zhang, Y., Zhang, J., Oishi, K., Faria, A.V., Jiang, H., Li, X., Akhter, K., Rosa-Neto, P., Pike, G.B., Evans, A., Toga, A.W., Woods, R., Mazziotta, J.C., Miller, M.I., van Zijl, P.C., Mori, S., 2010. Atlas-guided tract reconstruction for automated and comprehensive examination of the white matter anatomy. Neuroimage 52, 1289-1301.
Zhu, H., Kong, L., Li, R., Styner, M., Gerig, G., Lin, W., Gilmore, J.H., 2011. FADTTS: functional analysis of diffusion tensor tract statistics. Neuroimage 56, 1412-1425.

Biographical Information

Virendra Mishra was born in Mumbai, India in March 1983. He received his Bachelor of Engineering (B.E.) degree from Thadomal Shahani College of Engineering (TSEC), Mumbai University, India in June 2005. He worked for a couple of years as a field service engineer and applications support specialist before coming to United States. He began his graduate course at University of Texas at Arlington (UTA) and completed his Masters of Science (M.S.) in Electrical Engineering in May 2009. After getting his M.S. degree, he became a graduate student in Joint Biomedical Graduate Program between UTA, UTSW and UT Dallas and completed his PhD. He completed his PhD in May 2014 from the laboratory of Dr. Hao Huang at Advanced Imaging Research Center (AIRC), UT Southwestern Medical Center (UTSW). His dissertation was titled "Establishing the method of Dual-Tensor for Tract based Analysis (DTTA) and investigating human brain developmental connectome with diffusion MRI".